UNIVERSITÀ DEGLI STUDI DI UDINE

Dipartimento Politecnico di Ingegneria ed Architettura

Corso di Dottorato in Ingegneria Industriale e dell'Informazione

Tesi di Dottorato

NUMERICAL MODELING OF SUPERCONDUCTING CABLES FOR FUSION MAGNETS

Supervisore:
Prof. FABRIZIO BELLINA

Dottorando:
FRANCESCO STACCHI

CICLO XXXII – 2020

Sabes para mi ese dinero no me importa,
Yo tengo mi familia lo mas importante en me vida.

Acknowledgment

First of all I want and I need to thank my supervisor Prof. Fabrizio Bellina. Besides being an excellent professor and researcher, he is a very special person. He introduced me to superconductivity and to programming without fear, but at the same time, he taught me the importance of loyalty and fairness in the work place like in the every day life. He shown me the determination, the patience and the passion that are needed to achieve even the most unrealistic goals.
I thank Prof. Pier Luigi Ribani from University of Bologna for his time and kindness. He gave me a lot of useful suggestions for my studies. I thank also Prof. Marco Breschi for all the fruitful conversations.
Special thanks must be given to Pierluigi Bruzzone for having me at the Paul Scherrer Institute. Spending four months with him and his research team was a really unique experience. He shared knowledge with me, and I need to thank him also for this. Many thanks to all the other members of the research team for their hospitality. In particular I want to thank Boris Stepanov for the numerous discussions about AC losses. I have learned a lot from his experience and wisdom.
I also would like to thank Arend Nijhuis from University of Twente for supplying experimental data necessary for my research activity.

Ringrazio i miei genitori per essere stati sempre presenti e per avermi fatto sentire il loro appoggio. Sempre. Quello che sono ora lo devo alle numerose opportunità che ho avuto grazie a voi.
Ringrazio Andrea, mio fratello, per essere una immensa fonte di ispirazione. Ho sempre ammirato, ed anche un po' invidiato, la tua curiosità senza fine.
Un saluto speciale va agli amici di Roma che ho lasciato dopo essermi trasferito a Udine. Grazie a voi ho capito ancora di più quanto sia bello essere legato ad una persona, ad un luogo, a certi modi di essere.
Ringrazio i compagni di dottorato che ho conosciuto qui ad Udine. Persone speciali dalle quali ho imparato molto, nella vita di tutti i giorni come sul lavoro.

Devo ringraziare anche Vincenzo, Ortensia, Paola, Flavio, Chiara e Salvo per avermi fatto passare quattro mesi che difficilmente dimenticherò, per avermi accolto e fatto sentire a casa.

Abstract

In a superconducting multi-stage conductor, many electromagnetic features depend on the strands geometry that affects the cable behavior at both the local and the global levels, determining the inter-strand contact resistances distribution and the coupling current loops shape. To model these phenomena in detail, an accurate description of the cable strands geometry is necessary to get the strand trajectories and, possibly, the inter-strand contact areas. Since analytical or semi-analytical approaches for the cables geometrical modeling, that were successfully adopted for cables with circular cross-section, are not sufficiently adequate for conductors with square or rectangular cross-section, a new geometrical model based on a simplified structural approach has been developed for the numerical code THELMA.
The new geometrical model for rectangular cable-in-conduit conductors and multi-stage Rutherford-like cables is based on a virtual cabling sequence, followed by a compaction procedure to give the desired shape to the conductor cross-section. To reduce the inter-strands and the conduit-strands geometrical interferences due to both the cabling and the compaction procedures, an iteratively elastic contact model has been implemented, which takes into account an elastic force acting on the strands cross-section. These forces are evaluated on the basis of the local geometrical interferences and the strand transversal contact stiffness. In this thesis, the main characteristics of the new geometrical model are presented in detail.
The geometrical model validation is also shown and discussed, based on the AC losses analysis on DEMO TF rectangular cable samples carried out with the THELMA code. In particular, the coupling currents loss has been computed and compared with the measured one after the tuning of the strands contact resistivity parameters with respect to experimental inter-strand resistance data. Contact resistances are of a paramount importance for the numerical modeling of the equivalent electromagnetic network of the cable used for the computation of the coupling loss. Hence, the agreement between the experimental and the numerical AC losses results represents a key point for the geometrical model validation.

An important aspect to be taken into account for the AC losses estimation in superconducting cables is the presence of eddy current loss in the copper stabilizer which is needed for the conductor stability. In this thesis, a preliminary study to model a new stabilizer proposed for one of the DEMO TF prototype conductors is discussed. In particular, the transversal resistance of the stabilizer has been numerically analyzed and the eddy currents loss due to a time-varying magnetic field has been computed with the THELMA code.

Contents

List of Figures

Chapter 1

Introduction

1.1 Nuclear fusion

Thermonuclear fusion can be an important long-term energy source to complement the others resources like fossil fuels, e.g. coal, gas and oil, nuclear fission and renewable sources. In fact, fusion power has several advantages such as no greenhouse gases emissions, abundance of fuel, inherently safe system and no long-life radioactive waste production. Fusion is a process where light nuclei collide and merge together to form a heavier nucleus releasing energy in according to the Einstein's equation $E = mc^2$ [10]. The most promising fusion reaction involves two hydrogen isotopes, deuterium (D) and tritium (T):

$$\mathrm{D} + \mathrm{T} \rightarrow \mathrm{He} + \mathrm{n} + 17.6\mathrm{MeV}\,. \tag{1.1}$$

Since the total mass of the fusion products is lower than the one of the interacting particles, an energy Q of 17.6 MeV is released according to the mass-energy equivalence principle and it is distributed as kinetic energy between the resulting alpha particle and the neutron, with ratio inverse to their respective masses:

$$\mathrm{E_n} = \mathrm{m_{He}}/(\mathrm{m_{He}} + \mathrm{m_n}) \times \mathrm{Q} = 14.1\ \mathrm{MeV}\,, \tag{1.2}$$

$$\mathrm{E_{He}} = \mathrm{m_n}/(\mathrm{m_{He}} + \mathrm{m_n}) \times \mathrm{Q} = 3.56\ \mathrm{MeV}\,. \tag{1.3}$$

This and other kind of nuclear reactions are possible at very high temperatures, nearly 150 million degrees Celsius (> 10 keV), where electrons are separated from nuclei and matter becomes plasma, i.e a hot and fully ionized gas. To produce and control a stable plasma, a fusion reactor able to withstand these extreme working conditions is needed. One of the most promising solutions is the so-called *Tokamak*, a toroidal machine composed by several components,

which use a strong magnetic field to confine the plasma inside a *vacuum vessel* such that it does not touch the walls. However, the neutrons of 14.1 MeV released by the D-T reactions have no electrical charge, therefore they are not affected by magnetic field so they escape from the plasma and are absorbed by a suitable *blanket*, surrounding the vacuum chamber. In the blanket their energy is deposited as heat and extracted to produce steam used in conventional turbines and alternators.

1.2 Tokamak magnet system

The magnetic field required to control the plasma is produced by a complex coils system which involve the superimposition of three different contributions to the resulting field lines. Usually, a D-shaped toroidal field (TF) winding, an ohmic-heating central solenoid (CS), and a set of poloidal field (PF) coils and correction coils (CC) are needed to obtain toroidal helical shaped field lines which allow the plasma electrically charged particles to spiral inside the chamber without interacting with the walls.

Since the intensity of the magnetic field can be very high, up to more than

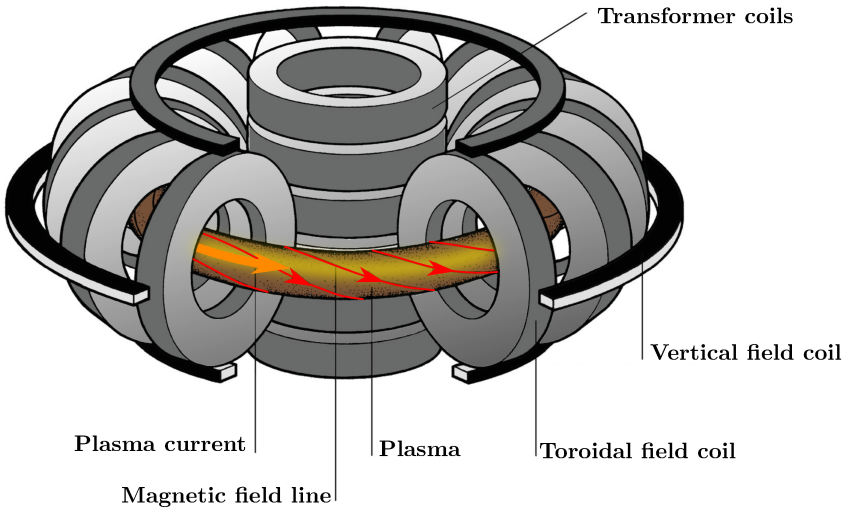

Figure 1.1: Tokamak magnet system.

10 T, superconducting cables are taken into consideration for the realization

of the reactor coils in order to reduce losses in the coils. This is the case of *ITER*, the largest fusion device based on the Tokamak design technology that is under construction in Cadarache,France [11]. ITER will be the first reactor to produce net energy with a design output and input powers of 500 MW and 50 MW respectively. Another goal of the machine is to demonstrate the reliability of all the technologies developed for a fusion power plant and the feasibility of their integrated operation, the achievement of a stable plasma operation and the on-site tritium breeding. The operating specifications of the ITER coils in terms of current and peak magnetic field are specified as follow: TF cables 68 kA/11.8 T, CS cables 40-45 kA/13 T, PF cables 45-55 kA/5.7 T [12]. Given the strong magnetic fields involved, the reason for using superconducting magnets is therefore clear: the zero resistance of superconductors allows operations at very high currents without worrying about the resistive losses typically observed in normal conductors like copper ($R_{Cu}I^2$). The superconducting state is achieved by the conductor below a set of *critical* values of *temperature*, *magnetic field* and *current density* which depend on the material. These three critical quantities are not independent but they form the *critical surface* that separates the normal state, above it, from the superconductivity state, below it as shown in Figure 1.2.

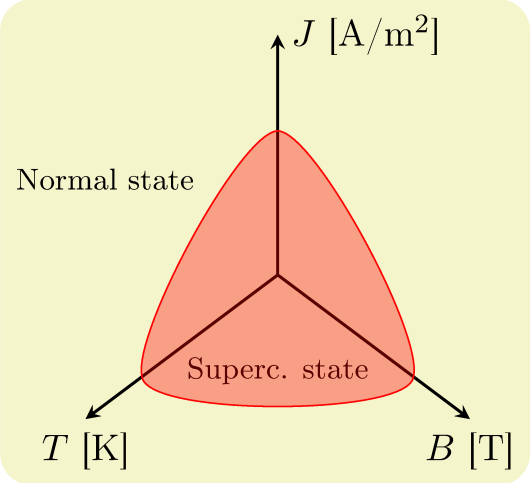

Figure 1.2: Sketch of the critical surface of a superconductor.

Although ITER represents a fundamental step to achieve the goal of large-scale electricity generation from fusion, the next step has been already identified as DEMO, a DEMOnstration Fusion Power Plant able to deliver electricity power to the grid [13]. Since DEMO will be a Tokamak much bigger

than ITER, many technological choices that are going to be tested in ITER will have to be adapted to satisfy the DEMO requirements.

1.3 Cables for fusion magnets

The so-called *Cable-In-Conduit Conductor* (CICC) is the most common solution adopted for the superconducting conductor of a Tokamak coils. Differently from the *Rutherford cables* which are mostly used for particles accelerator magnets [14], CIC conductors, thanks their robust mechanical design and a good cooling capability, are able to carry high levels of current, e.g. up to 68 kA for ITER cables, and to withstand the severe working conditions present in a fusion machine that arise from radiations, huge mechanical stresses, electromagnetic loads and plasma instabilities or disruptions. These type of conductors are composed by several strands twisted together according to a multi-stage cabling scheme, and then inserted in a resistive jacket and compacted. Mostly, the first stage of cabling is made by twisting three strands with a twist pitch t_1 to form the so-called *triplet*, which represents the 1^{st} order bundle of the cable. Then, all the triplets are usually twisted in groups, e.g. three of them, to form a 2^{nd} order bundle usually referred to as 3×3 with a different twist pitch t_2. The 3^{rd} order bundle is evidently formed by twisting together a certain number of 2^{nd} order sub-cables, e.g. four of them, to obtain a 3×3×4 bundle (see Figure 1.3). This procedure is repeated up to the last cabling stage with increasing twist pitches. The last order sub-cables are referred to as *petals*. Intermediate, if necessary, and final compaction are applied to the bundles to control their cross-section shape.

To give sufficient mechanical stiffness to the magnet conductor, the compacted final cable is inserted in a jacket with a circular, square or rectangular cross-section. A final compaction of the jacketed conductor is then performed

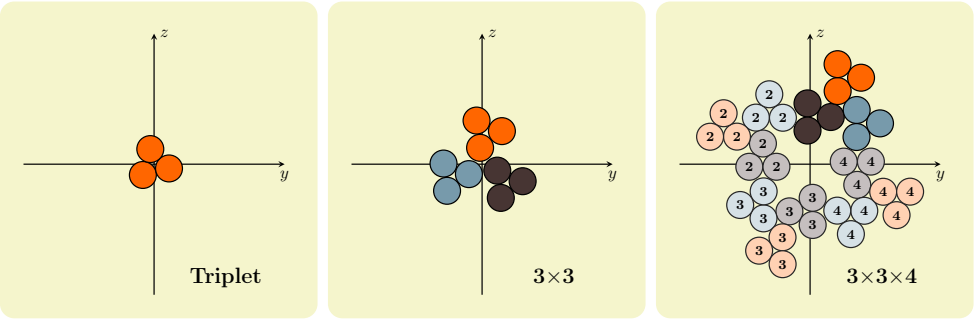

Figure 1.3: Cabling stages of a sub-cable made by 36 twisted strands.

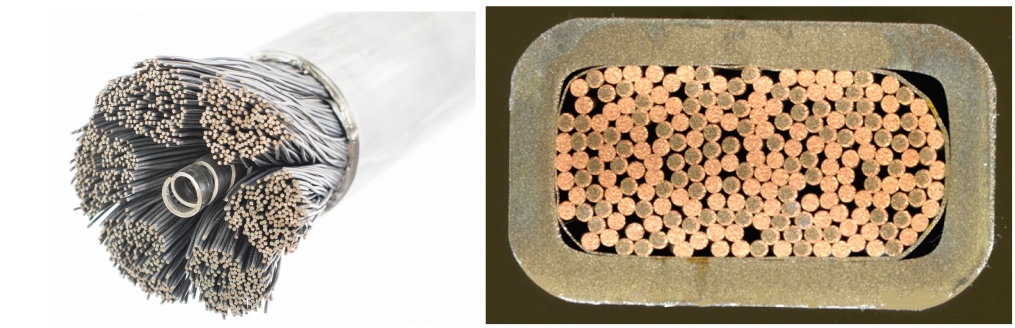

Figure 1.4: Left: ITER TF conductor with a circular jacket; the six petals around the central spiral are clearly visible (Courtesy of Charlie Sanabria, NHMFL-FSU [1]). Right: cross-section of the NAFASSY conductor with a rectangular jacket [2].

to achieve its final dimensions. The relatively high void fraction of the conductors, i.e. 25-40%, and the inner channels realized by steel spirals (see Figure 1.4) allow the forced-flow cooling by means of *super-critical* helium, i.e. helium at a temperature and pressure above its critical point ($T_c = 5.1953$ K, $P_c = 0.2274$ MPa).

1.4 Superconducting strand

In a CIC conductor the superconducting material is embedded as very fine filaments in a low-resistance matrix such as copper, forming the so-called multi filamentary wires or *strands*. The most common materials used to produce the low temperature superconducting filaments are NbTi and Nb_3Sn. NbTi [15] is used for magnetic field up to 8 T and is considered one of the best superconducting soluble alloys thanks to its mechanical properties. It is very ductile and strong at the same time, and these features also permit a cheaper fabrication process compared to other materials like Nb_3Sn. The inter-metallic compound Nb_3Sn [16] allows operation up to 16 T because of its high critical parameters but, at the same time, it is very hard and brittle, making the fabrication process difficult and expensive. Moreover, a small elongations can irreversibly degrade or fracture the material. Both NbTi and Nb_3Sn require liquid helium as coolant in the range of $1.9 - 5$ K.
In the case of the strand, as the current exceeds a certain value, a longitudinal electric field appears. The transition to the resistive state is not sudden. The *strand critical current* I_c [A] is defined as the current flowing in the strand

in correspondence to the *critical electric field* E_c, typically assumed as 10 μV/m. An experimental standard test is usually adopted to determine I_c [17]: voltage taps are suitably applied to a strand specimen to measure the voltage drop due to the injection and the ramp up of the current I [A] at constant temperature. The experimental results show that the field-current characteristic of a superconductor can be expressed in term of the so-called *power law* [18]:

$$E(I) = E_c \left(\frac{I}{I_c}\right)^n , \tag{1.4}$$

where n is the so-called *n-index*. It can be retrieved from the logarithmic slope of the voltage-current characteristic or, in case of Nb_3Sn strands, it can be also empirically characterized as a function of temperature T, magnetic induction B and applied strain ϵ [19][20]:

$$n = 1 + r(T,\varepsilon) \cdot [I_c(B,T,\varepsilon)]^{s(T,\varepsilon)} , \tag{1.5}$$

where r and s are two fitting functions of T and ϵ.
Generally, it is possible to describe the critical current density J_c of a superconductor as a function of field, temperature and, possibly, strain by semi-empirical relations called *scaling law* which are based on parameters found experimentally. For NbTi strands, the most common law is based on the *Bottura fit* [21]:

$$J_c(B,T) = \frac{C_0}{B}\left(\frac{B}{B_{c2}(T)}\right)^{\alpha}\left(1-\frac{B}{B_{c2}(T)}\right)^{\beta}\left[1-\left(\frac{T}{T_{c,0}}\right)^n\right]^{\gamma}, \tag{1.6}$$

where $B_{c2}(T)$ is the upper critical induction at the operating temperature expressed as:

$$B_{c2}(T) = B_{c2,0}\left[1-\left(\frac{T}{T_{c,0}(T)}\right)^n\right], \tag{1.7}$$

with exponent n equal to 1.7. $T_{c,0}$ is the critical temperature at zero field whereas C_0, α, β and γ are the free fitting parameters to be set for the specific strand. For Nb_3Sn strands, the *Durham scaling law* [22] is frequently used and it is defined through these equations:

$$J_c(B,T,\epsilon) = A(\epsilon)[T_c^*(\epsilon)(1-t^2)]^2[B_{c2}^*(T,\epsilon)]^{n-3}b^{p-1}(1-b)^q , \tag{1.8}$$

$$B_{c2}^*(T,\epsilon) = B_{c2}^*(0,\epsilon)(1-t^{\nu}) , \tag{1.9}$$

$$\left(\frac{A(\epsilon)}{A(0)}\right)^{1/u} = \left(\frac{B_{c2}^*(0,\epsilon)}{B_{c2}^*(0,0)}\right)^{1/w} = \frac{T_c^*(\epsilon)}{T_c^*(0)} , \tag{1.10}$$

$$\frac{B^*_{c2}(0,\epsilon)}{B^*_{c2}(0,0)} = 1 + c_2\epsilon^2 + c_3\epsilon^3 + c_4\epsilon^4 \ , \tag{1.11}$$

$$\epsilon = \epsilon_A - \epsilon_M \ , \tag{1.12}$$

where ϵ_A is the applied strain, ϵ is the intrinsic strain, ϵ_M is the applied strain at the peak, T^*_c is the effective critical temperature, B^*_c is the effective upper critical field, $b = B/B^*_{c2}$ is the reduced field and $t = T/T^*_c$ is the reduced temperature. The fitting parameters are 13 but they become 9, without much loss of accuracy, if 4 of them are assumed as: $n = 2.5$, $\nu = 1.5$, $w = 2.2$, $u = 0$. Other relations useful for this material were proposed by *Summers* [23] and *Godeke* [24].
The composite structure of the strands provides *stability* to the conductor during its operation. The use of superconductor in the form of thin filaments is mandatory to avoid the well-known phenomenon called *flux jump* [18]. On the other hand, if superconductors become resistive because of a local increase in temperature due to a localized depositions of energy, the normal metal stabilizing matrix offers higher conductivity compared to the filaments, so the current flows in the stabilizer and the ohmic heating is transferred to the liquid helium which flows inside the conductor and wets the outer surface of the strands. If the heat removal rate is larger than the ohmic heating rate, the temperature decreases and the current returns to the superconductor. Moreover, in a CIC conductor, additional copper strands are usually twisted together with the superconducting ones to enhance the stability of the cable (see Figure 1.4). These strands form the so called *segregated stabilizer*.

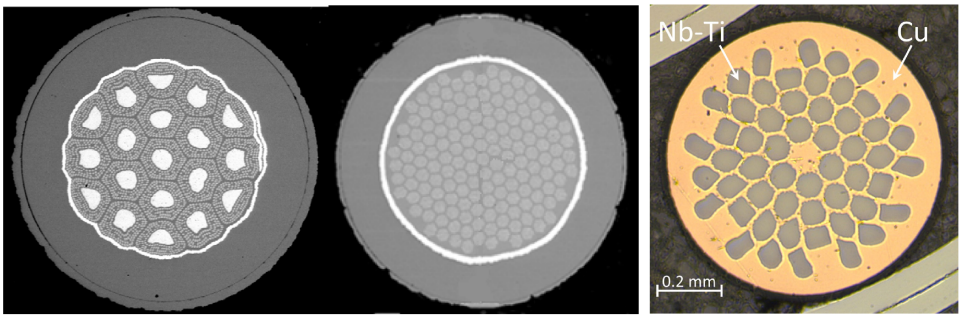

Figure 1.5: Left: *internal tin* (left) and *bronze-route* (right) Nb_3Sn strands for ITER TF [3]; Right: NbTi strand [4].

1.5 Loss in superconductor

Even if superconductors offer a negligible resistance to the passage of current, energy dissipation phenomena which compromise their stability may occur. In fact, when a superconductor is subjected to a changing magnetic field, *screening currents* of density J_c are induced which flow on the surface and tend to shield the superconductor from the external field. These currents, that are in addition to the *transport current* which is the net current energizing the magnet, behave like eddy currents but, due to the zero resistance state of the superconductor, they do not decay. As a first consequence, the presence of these persistent currents produces a magnetization M, a magnetic moment per unit volume, which leads, when no transport current is flowing, to a *hysteresis loss* $Q_{hyst} = \oint M dH$ due to the external field cyclic variation [25]. Filamentary composites are preferred to thick single core or slab configurations to reduce the magnetization, as well as for their efficacy against the flux jump. Unfortunately, when a time-varying magnetic field transverse to the strands is

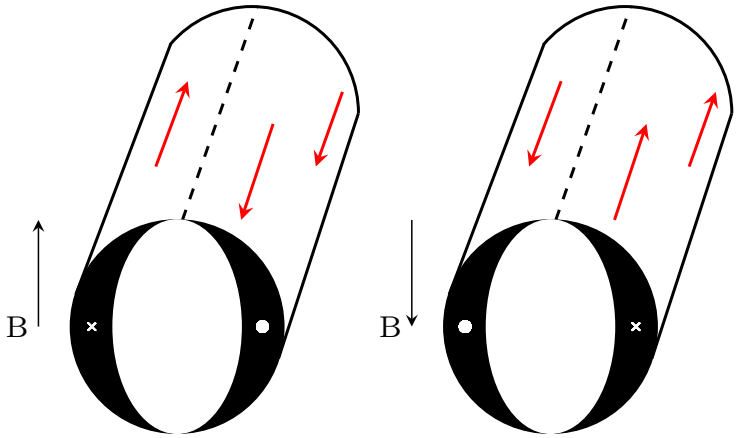

Figure 1.6: Induced screening current on the strand outer surface in presence of an external time-varying uniform magnetic field.

applied, the superconducting filaments are magnetically coupled to each other, and the strand matrix offers the opportunity to the screening currents to pass from one filament to the others. These *coupling currents* represent another source of energy dissipation since they crossover through the resistive matrix in order to close the loops. One of the most powerful solution to reduce the coupling loss, also called *inter-filaments* or *intra-strand* loss, is to twist the filaments together in the strands [26][27]. Another contribution to the total losses due to the presence of an external variable field is given by the eddy currents induced in the normal matrix (pure *eddy currents loss*). This term,

which is negligible at low frequencies in comparison with the others, strongly depends on the strand size and matrix resistivity [28]. At high frequencies, the shielding effect of the currents circulating in the copper layer at the strands surface (*skin effect*) can be significant and lead to a reduction of both coupling and magnetization [29]. In the case of a multi-stage conductor, the strands are in turn magnetically coupled and many different loops are created by the induced currents which flow through the contacts between the twisted strands. A non negligible resistance of these contacts generates the *inter-strand loss* which strongly contributes to the total *AC losses*. The strategy of twisting the strands to form larger and larger bundles with different twist pitches arose from the need to limit the inter-strand loss by the transposition of the strands. The prediction of AC losses is therefore a important issue of a conductor design because of the need to protect the coils against a potential thermal runaway (*quench*) during transient regime or pulsed operations. Unfortunately, a large number of factors affect the final behavior of the conductors, so that the simulation of the AC losses phenomenon is very challenging from the numerical modeling point of view. The analysis of the cable losses must span from the whole conductor down to the individual strands and, if necessary, the strands filaments. Therefore, one of the most important aspects is the accuracy of the conductor geometry which defines the trajectories of the strands and determines the distribution of the contact points where the coupling currents loops can close. Several codes have been developed to study superconductors starting from the description of their geometry and material properties. One of them is THELMA, a thermal-electromagnetic coupled code jointly implemented by Udine and Bologna Universities.
The aim of this thesis was to develop and validate a new geometrical model able to reproduce in a realistic way the geometry of multi-stage superconducting cables with square or rectangular cross-section. In particular, for the model validation, AC losses analyses have been carried out by modeling DEMO TF rectangular conductors in order to calculate the coupling currents loss and compare the numerical results with the experimental ones.

Chapter 2

New geometrical models for multi-stage superconducting cables

2.1 Introduction

When a new conductor is proposed for the realization of a superconducting coil, it is mandatory to verify its properties by means of experimental analysis which are useful to test its behavior in a real operating scenario. For the most common cables used for the fusion reactor magnets, i.e. the CICCs, the prediction of the conductor performances is hard because of the large amount of parameters that characterize the conductor like the diameter, the number and the strands type, the cabling scheme and the twist pitches of all the stages, the void fraction and the final shape of the conductor. All these specifications affect the mechanical and the electromagnetic behaviors. Therefore numerical models have always played a fundamental role in supporting the development of a new CICC, since the manufacturing process of a testing sample can be very expensive as well as time-consuming. A validated model can help to predict the right features that must be satisfy by a cable to ensure a safe operation. At the basis of most of the numerical analyses, an accurate description of the cable geometry and a verisimilar representation of the strands trajectories is necessary. General purpose finite-elements software, that would require an enormous number of mesh elements to describe a very complex geometry, are not suitable. Thus, dedicated codes usually based on the generation of an equivalent lumped or distributed electrical network derived directly from the strands geometry and the materials properties have been implemented to better analyze cables and magnets. The ideal approach to this problem could be a

cable 3D structural analysis like the one adopted for the strands geometry description model shown in [30], which gives a very detailed cable geometry, but at the same time it may be quite cumbersome and able to reproduce the geometry of a single straight petal and not of the whole cable [31][32]. To achieve a compromise between accuracy and applicability, a few heuristic geometrical models based on an analytical approach have been adopted in numerical codes which proved to be acceptable. In the original THELMA model developed for the CICCs the geometries of both bundles and strands were built starting from the cable axis, followed by the sub-cables axis, down to the strand axis. For each cabling stage, the bundle or strand axis geometry was created considering the axis as a helix wound around the axis of the following cabling stage [33]. Another code based on an analytical helical geometry is the one developed by the University of Twente called *JackPot*.
These codes have often been used to model the geometry of CIC conductors with circular cross-section, like ITER conductors, in order to analyzed the contact resistances distribution, to simulate a quench scenario or to compute the AC losses. However, questions may arise about the models applicability to a cable with a rectangular or square shape, since the twisted bundles axes, at any stage of cabling, do not follow an analytical helix trajectory. For this reason, a new geometrical model has been developed for the THELMA code, which is able to reproduce the geometry of multi-stage conductors that are compacted down to a final rectangular cross section. This code implementation arose from the great interest on flat shaped cables for the next fusion reactors [34][6][35] because of their enhanced performances in terms of degradation with electromagnetic loading or thermal cycles thanks to the lower electromagnetic pressure over the superconducting strands [36][9][37].
In the present chapter, the THELMA geometrical models are presented and the new geometrical model for rectangular multi-stage conductors is explained in detail.

2.2 THELMA Geometrical Models

The procedure adopted by the THELMA code to model the geometry of superconducting cables can be summarized into three main steps:

- the first one is the *definition of the cable cross-section* by which the material and the geometrical properties of each strand are imposed and more and more complex bundles are determined by grouping strands or sub-bundle of lower stages according to the cabling scheme. In this step the twist pitches and the void fractions are also defined;

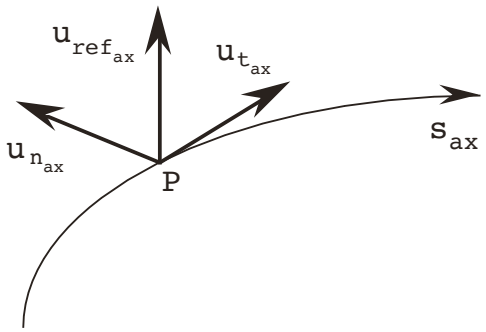

Figure 2.1: Cable axis described as a function of s_{ax} by the local triad [5] (courtesy of Giulio Manfreda).

- the second step is the *definition of the cable axis geometry* making use of embedded primitives to describe e.g. rectilinear segments, helices, circles or circle arcs. The reference unit vector $\mathbf{u}_{ref,ax}$ is used to set the cable angular position around the cable axis and the unit vector $\mathbf{u}_{\mathrm{n,ax}} = \mathbf{u}_{\mathrm{ref,ax}} \times \mathbf{u}_{\mathrm{t,ax}}$ forms, together with $\mathbf{u}_{ref,ax}$ a local 2D triad used to described the geometry of the cable cross-section. A local triad ($\mathbf{u}_{t,ax}$, $\mathbf{u}_{n,ax}$, $\mathbf{u}_{ref,ax}$) is defined as a function of the curvilinear coordinate along the cable axis s_{ax} , as shown in Figure 2.1;

- the third and last step is the *computation of the strands geometry*: starting from the cable cross-section data, the trajectories of the strands can be calculated according to one of three main models which aim the geometry of CIC conductors:

  1. a pseudo-analytical model for circular bundles, referred to as *PAG model*;
  2. the pseudo-structural model for bundle with generic cross-section, referred to as *PSG model*;
  3. the analytical model for Rutherford bundles.

2.2.1 The pseudo-analytical model for multi-stage cables

The computation of each individual strand geometry for a CICC with circular cross-section was first implemented in the THELMA code on the basis of the pseudo-analytical approach described in [33]. The cabling procedure starts with the generation of helices around the cable axis corresponding to

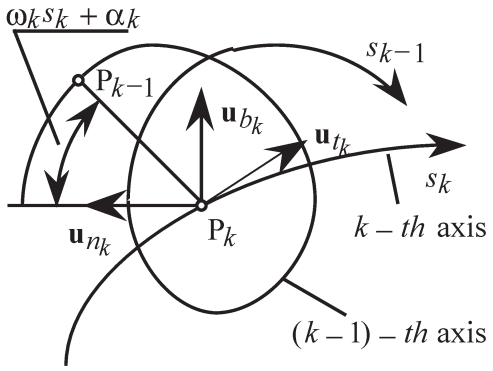

Figure 2.2: Illustration of the $(k-1)^{th}$ axis generation from the k^{th} one [5] (courtesy of Giulio Manfreda).

the so called petals. Then it continues with the generation of *composite helices* around the ones already prepared in the previous step. These new helices correspond to the axes of the last-but-two bundles, i.e. the axes of the petals sub-bundles. In the generic iteration of the procedure the points of $(k-1)^{th}$ axis are derived from the point of k^{th} axis as a function of the curvilinear coordinate along the k^{th} axis s_k, as shown in Figure 2.2, following the equation:

$$\mathbf{OP}_{\mathrm{k-1}} = \mathbf{OP}_{\mathrm{k}} + \mathrm{r_k cos}(\omega_{\mathrm{k}} \mathrm{s_k} + \theta_{\mathrm{k}})\mathbf{u}_{\mathrm{n_k}} + \mathrm{r_k sin}(\omega_{\mathrm{k}} \mathrm{s_k} + \theta_{\mathrm{k}})\mathbf{u}_{\mathrm{ref_k}} \,, \tag{2.1}$$

with $k = 1, ..., n_{\mathrm{st}}$, where $\mathrm{n_{st}}$ is the number of stages. $\mathbf{OP}_{\mathrm{k-1}}$ and $\mathbf{OP}_{\mathrm{k}}$ are the position vectors of the generic points of $(k-1)^{th}$ and $(k)^{th}$ axes, whereas $\mathrm{r_k}$ and θ_{k} are respectively the twisting radius and the initial angular phase of the k^{th} stage. ω_{k} is defined as $\omega_k = \frac{2\pi}{p_{\mathrm{k}}}$ and p_{k} is the current k^{th} twisting pitch. The twisting radii and the twisting pitches of any bundle are cable geometrical parameters, whereas θ_{k} is considered as a random variable since its value is generally unknown in a real cable. Thus, a pseudo-random array of initial angular phases $\mathbf{\Theta}$, called *phase set*, is generally assumed to describe the angular position of the cable bundles around the cable axis. Because of the non uniform curvature of the axis of a composite helix, the curvilinear coordinate cannot be computed analytically for each axis point at each stage. For this reason, a set of $\mathrm{P_{k-1}}$ points is assigned by means of a spline-based description: the points coordinates are first expressed as a function of the curvilinear coordinate s_{k}, in according to the Eq. 2.1, and then arranged as a function of the

curvilinear coordinate s_{k-1} which is numerically computed.
Despite the reliability of this geometrical model already used in several previous studies, e.g. see [38], the need to reproduce the geometry of flat cables with square or rectangular cross-section has led to the development of a new geometrical model, giving also the opportunity to improve the aspect related to the presence of geometric overlap between strands at any cable cross-section. The absence of strands geometrical overlapping cannot be achieved with an analytical or pseudo-analytical approach unless cables with very high, unrealistic void fractions are to be considered.

2.3 The new pseudo-structural geometrical model for rectangular multi-stage cables

The new geometrical model is based on the two main processes, namely the *cabling sequence* and the *compaction procedure*, which mimic the manufacturing process adopted for a real cable. During the first phase, made of several steps, the strands are twisted together to form bundles bigger and bigger thanks to the simulation of the the sub-bundles axes rotation. The strands, that are discretized into a set of several longitudinal elements, start to being wrapped together at one end of the cable making the progressively twisting up to the other end of the current bundle possible. The second main process is the compaction procedure which can be applied to the whole cable, at the end of the cabling sequence, as well as to the bundles of intermediate stages, allowing to wedge and shape the conductor if it is necessary. During this process, all the strands are gradually pushed inwards and get closer and closer as an effect of the compressive action of an external boundary. Both the cabling and the compaction processes are based on an elastic model which is used to remove the interferences between the strands. The overall model is widely applicable, therefore it is possible to easily achieve strands verisimilar trajectories whatever the shape of the cable.
In this section, the new geometrical model and its two main processes are presented for a cable with a rectilinear axis. The procedure creates a straight cable model, then the geometry of the cable strands is adapted to a general cable axis geometry by applying this mapping transformation:

$$\mathbf{x}^* = x_1\mathbf{u}_{\mathrm{t,ax}} + x_2\mathbf{u}_{\mathrm{n,ax}} + x_3\mathbf{u}_{\mathrm{ref,ax}} + \mathbf{x}_{\mathrm{a}}\,, \tag{2.2}$$

where $\mathbf{x} = (x_1, x_2, x_3)$ are the strand coordinates and $\mathbf{x}_{\mathrm{a}}$ is the cable axis point.

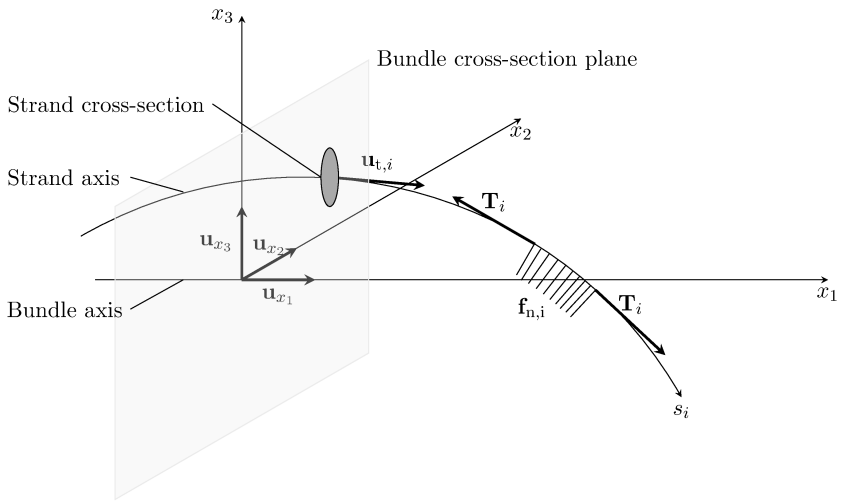

Figure 2.3: Rapresentation of the tensile force.

2.3.1 Strand model

As far as the strand behavior in the longitudinal direction is concerned, in the model, each strand is considered as a string with negligible tensile torsion and bending stiffness and friction coefficient. Therefore the following equations hold along the normal direction:

$$\mathrm{f_n(s)} = \rho \mathrm{T}\,, \tag{2.3}$$

where T is the tensile force [N], f_n is the distributed load [N/m], normal with respect to the strand axis, ρ [m^{-1}] is the axis local curvature, reciprocal of the curvature radius, and s is the curvilinear coordinate along the axis [m] (see Figure 2.3): for a straight axis segment, $\rho = 0$. In addition the tensile force modulus is constant along the axis, due to the absence of friction effects. The tensile force tends to straighten the strands throughout the whole cabling process. In this way, thanks to this tensile force, geometrical correlation between the strands position in close cable cross-section is kept, since an abrupt change of the strand position would result in a strong centripetal force. A non negligible compressive stiffness in the transverse direction is considered which results in inter-strand contact forces that allow to reduce as much as possible the geometric overlap of the strands.

2.3.2 Elastic model for the cable cross-section

To accurately describe the deformation and stress distribution among the strands in the bundle cross-section, a complex non linear analysis of the inter-strand contacts should be set-up. The Hertz contact theory could be a basis for this analysis [39]. More sophisticated models can be obtained using f.e.m. approaches [40]. However, since, in this case, the target of the analysis is the reconstruction of the strands verisimilar geometry, along the cable, a linearized contact model has been adopted, being the consequent approximation errors secondary with respect to the other model approximations, like those made about the strand stiffness.
To model the behavior of the strands in the bundle cross-section, each strand is supposed to have a circular shape. Actually, in a real cable, the strand cross-section in the cable cross-section is elliptical, due to the angle between the strand and the cable axis. This is usually described through the $\cos\theta$ parameter. In the model, to take into account the $\cos\theta$ value, the strand radius is suitably slightly increased. In the transverse direction, the strands are supposed to have a compression stiffness per unit of length K [N/m^2] computed as follow:

$$K = 2E \ , \tag{2.4}$$

where E [N/m^2] is the Young's modulus. This is clearly an overestimation of the actual stiffness, nevertheless, more accurate contact models could be implemented, however with a remarkable increase of the computation burden. An iterative approach is adopted to reduce the interferences between strands occur when the sub-bundles come into contact. Wherever a geometrical interference C_{ij} [m] between the *i-th* and *j-th* strands takes place at the generic coordinate x_1 [m], the interstrand resulting elastic distributed forces $\mathbf{F}_{\mathrm{i}}(x_1)$ and $\mathbf{F}_{\mathrm{j}}(x_1)$ [N/m] acting on the *i-th* and *j-th* strand are computed (see Figure 2.4):

$$\mathbf{F}_i(x_1) = -\mathbf{F}_j(x_1) = F_{\mathrm{ij}}(x_1)\mathbf{u}_{ij} \ , \tag{2.5}$$

$$F_{\mathrm{ij}}(x_1) = C_{\mathrm{i,j}}(x_1)K_{\mathrm{ij}} \ , \tag{2.6}$$

$$K_{\mathrm{ij}} = \frac{K_{\mathrm{i}}K_{\mathrm{j}}}{K_{\mathrm{i}} + K_{\mathrm{j}}} \tag{2.7}$$

$$\mathbf{u}_{ij} = \frac{\mathbf{x}_{\mathrm{i}}^{'}(x_1) - \mathbf{x}_{\mathrm{j}}^{'}(x_1)}{d_{\mathrm{i,j}}(x_1)} \ , \tag{2.8}$$

where $\mathbf{x}_{\mathrm{i}}^{'}(x_1)$, $\mathbf{x}_{\mathrm{j}}^{'}(x_1)$ and $d_{\mathrm{i,j}}(x_1)$ are respectively the two strands center positions and the distance between them in the plane orthogonal to the bundle

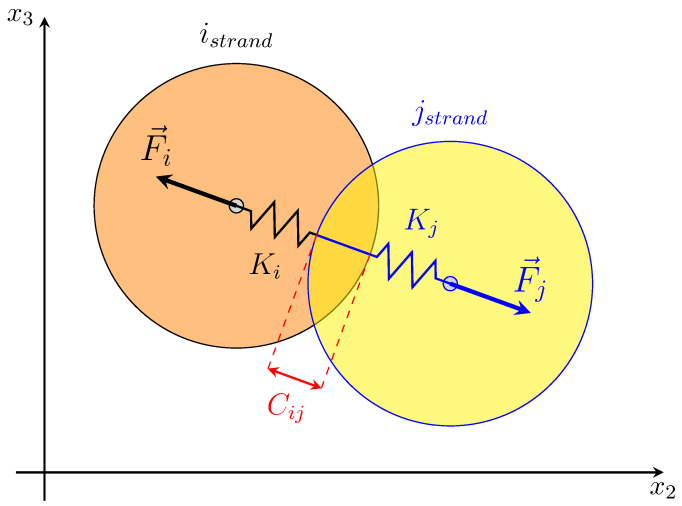

Figure 2.4: Contact detection and elastic forces computation.

axis at the coordinate x_1. For the single *i-th* strand, the resulting interstrand force is obtained by adding the contributions from the contacts in the bundle cross-section. If a number of contacts n is considered, it follows:

$$\mathbf{F}_{i,\mathrm{tot}}(x_1) = \sum_{\mathrm{j}=1}^{n} F_{\mathrm{ij}}(x_1)\mathbf{u}_{ij}\,, \tag{2.9}$$

The tensile force is also applied to the strands. The normal force along the cross-section is:

$$\mathbf{f}_{\mathrm{n,i}}(x_1) = T_i \frac{\mathrm{d}\mathbf{u}_{\mathrm{t,i}}}{\mathrm{d}x_1} \times \mathbf{u}_{\mathrm{i}}(x_1)\,, \tag{2.10}$$

where $\mathbf{u}_{\mathrm{t,i}}$ is the unit tangent vector to the bundle axis. The interferences of the *i-th* strand are progressively removed with an iterative approach on the basis of the resulting displacement $\mathbf{S}_{\mathrm{i}}(x_1)$ (see Figure 2.5):

$$\mathbf{S}_{\mathrm{i}}(x_1) = \frac{\mathbf{F}_{\mathrm{i,tot}}(x_1) - \mathbf{f}_{\mathrm{n,i}}(x_1)}{K_{i,\mathrm{stra}}}\,, \tag{2.11}$$

where

$$K_{i,\mathrm{stra}} = \sum_{j=1}^{n} K_{\mathrm{j}}\,. \tag{2.12}$$

It follows that, at the $(h{+}1)^{th}$ iteration:

$${}^{(h+1)}\mathbf{x}_{\mathrm{i}}^{'}(x_1) = {}^{(h)}\mathbf{x}_{\mathrm{i}}^{'}(x_1) + \mathbf{S}_{\mathrm{i}}(x_1)\,. \tag{2.13}$$

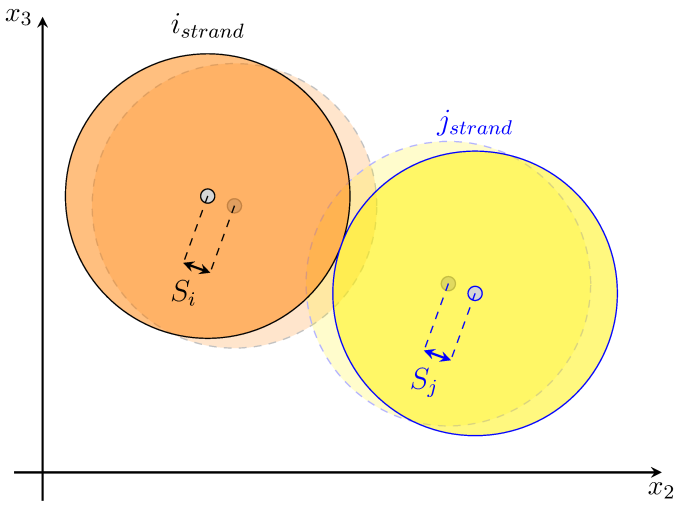

Figure 2.5: Interference removed.

A *minimum displacement* value evaluated on the basis on the strands radii is set as threshold to stop the iterations process. It is computed as a given percentage of the minimum strand radius among all the cable strands. The iterations are repeated until the maximum strand displacement is smaller than the minimum fixed one.

2.3.3 Cabling sequence

Before the cabling procedure starts, all the strands are first organized in sub-bundles according to the cabling scheme already set by the definition of the cable cross-section, as shown in Section 2.2. Then, the sub-bundles are progressively twisted together by the rotation of their axes:

- for the first stage, which is mostly made of triplet, the single strands correspond to the sub-bundle axes (see Figure 2.6 a);
- for the following cabling stages, new axes are created according to the layout scheme, and the sub-bundles being twisted are assembled over them through a suitable coordinate transformation from the sub-bundle reference system to the bundle system (see Figure 2.6 b).

The axes are kept restrained at the initial cross-section, where they are arranged one close with the other, and rotated at the end to simulate the action of the cabling rotating drum. In this way, the current bundle is being progressively twisted from the initial to the final cross-section.

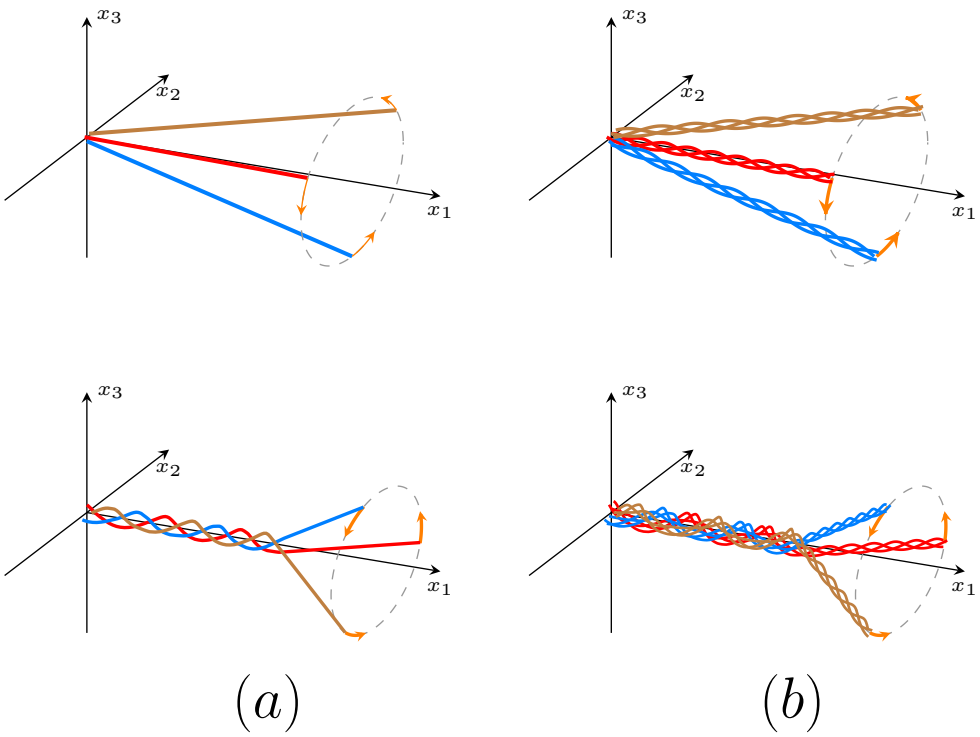

Figure 2.6: Twisting of 1^{st} stage - Triplet (a) and 2^{st} stage - 3×3 bundle (b).

Axes rotation

Each sub-bundle axis is discretized in several segments called *work elements* that are progressively processed and twisted together with those of the other axes thanks to the applied rotation. To start the cabling process the first work element is created by linear interpolation between the first and the last point of the corresponding axis by means of the following data:

- Coordinates of the first axes point $(\rho_{\text{in}}, \vartheta_{\text{in}}, x_{1,\text{in}})$;
- Coordinates of the last axes point $(\rho_{\text{end}}, \vartheta_{\text{end}}, x_{1,\text{end}})$;
- Current bundle desired twist pitch: p_{k};
- Cable axis length: L_{cable}.

The coordinates of the first axes point derived from cable cross-section definition, whereas ϑ_{end} and $x_{1,\text{end}}$ are set equal to ϑ_{in} and L_{cable} respectively in order to obtain straight axes as initial configuration. ρ_{end} is suitable larger than ρ_{in}, to mimic the effects of the cabling rotating drum. It is computed in according to the helix law (see Figure 2.7):

$$\rho_{\text{end}} = 2\pi\rho_{\text{in}}\frac{L_{\text{cable}}}{p_{\text{k}}}. \tag{2.14}$$

As in the real cabling process, the resulting twist pitch of the sub-bundles is due to angle between the straight, not yet wound, part of the sub-bundles, and the bundle axis. Larger angles lead to shorter twist pitches. When a new work element has been created for each axis, the simulation of the cabling procedure start: the strands/sub-bundles are twisted thanks to a gradual rotation applied to the end point of the axes in the plane orthogonal to the bundle axis. This sequence is repeated until the work elements come into contact, so new work elements are assigned starting from the previous one, which are locked, and then twisted together with the others (see Figure 2.8). For the first stage of cabling, in which the work elements correspond to a segment of the strands, the meant contact is the one between the axes, but, for higher order bundles, the contact between strands of different sub-bundles is considered. In this way, the current bundle is cabled by a step-by-step process during which, new segments are created and twisted. Since the sub-bundles cross-section may have any shape depending on the stage and the phase set, the rotation is not fixed a priori, but it is preliminary evaluated as follows:

$$\omega_{\text{k}} = \frac{2\pi * l_{\text{we}}}{p_{\text{k}}} r_{\text{fact}}. \tag{2.15}$$

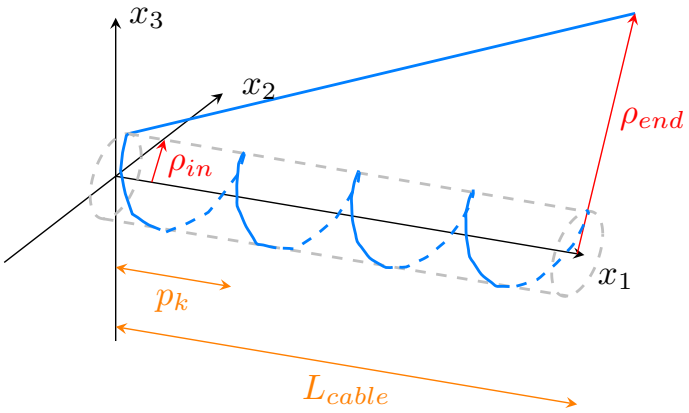

Figure 2.7: Helix law rapresentation.

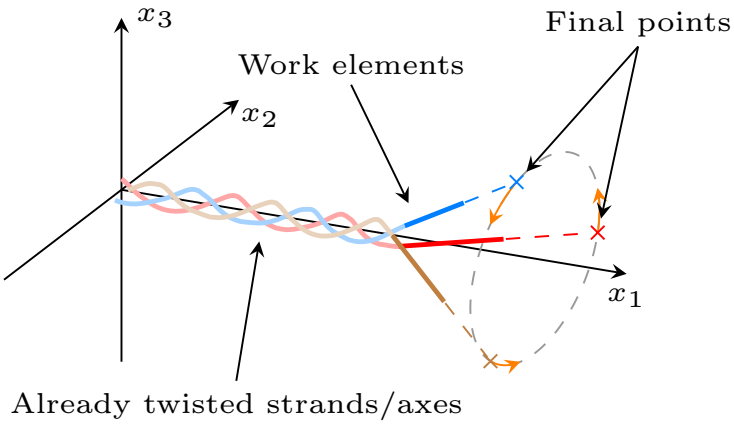

Figure 2.8: Sketch of the cabling sequence.

where l_{we} is the work elements length, which is determined by the longitudinal discretization of the cable, and r_{fact} is the *rotation damping factor* used to adapt the rotation to the current sub-bundles configuration. At each step of cabling, the end point of the axes is moved forward along the cable axis to keep constant the distance from the current work elements and the final points until the whole bundle is twisted, so that the proper twisting pitch is preserved.

2.3.4 Compaction procedure

The new geometrical model provides also a procedure for the cable compaction which is applied after the cabling sequence completion, if necessary. For each stage of cabling of the bundle, it is possible to shrink its boundary until the final or an intermediate size and shape is reached, in order to obtain a circular or a rectangular cross section:

- bundles of intermediate orders are usually *pre-compacted* to a circular shape;
- the final bundle corresponding to the whole cable is compacted down to the final circular or rectangular shape.

The rectangular compaction can be preceded by a circular one according to the real cable manufacturing procedure.
The compaction procedure is based on the progressive shrinking of the bundle external boundary until the final dimensions expressed in terms of minimum and maximum coordinates are reached, as shown in Figure 2.9. The compaction process is completed when all the strands are contained between the boundary final values which are set according to the void fraction of the current bundle.

Boundary shrinking

The first step of the compaction procedure is to set a work temporary boundary including all the uncompacted strands. The second iterated step is to shrink the boundary: its sizes are gradually reduced by steps of a given percentage of the minimum strand radius (see Figure 2.10). This boundary shrinking usually gives rise to a new set of strand-boundary interferences, with consequent elastic transverse force. As for the strand-strand contacts, the model considers an elastic force $\mathbf{F}_{\text{i,bound}}(x_1)$ acting on the *i-th* strands cross-section at the coordinate x_1 evaluated on the basis of the strand-boundary interference size and the strand transversal stiffness K_{i}. This force is normal

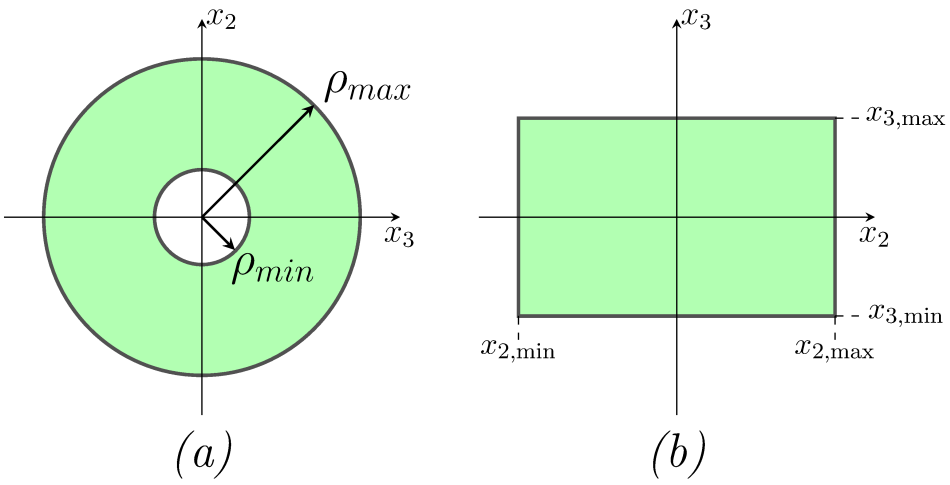

Figure 2.9: Maximum and minimum coordinates of circular (a) or rectangular (b) final cross section.

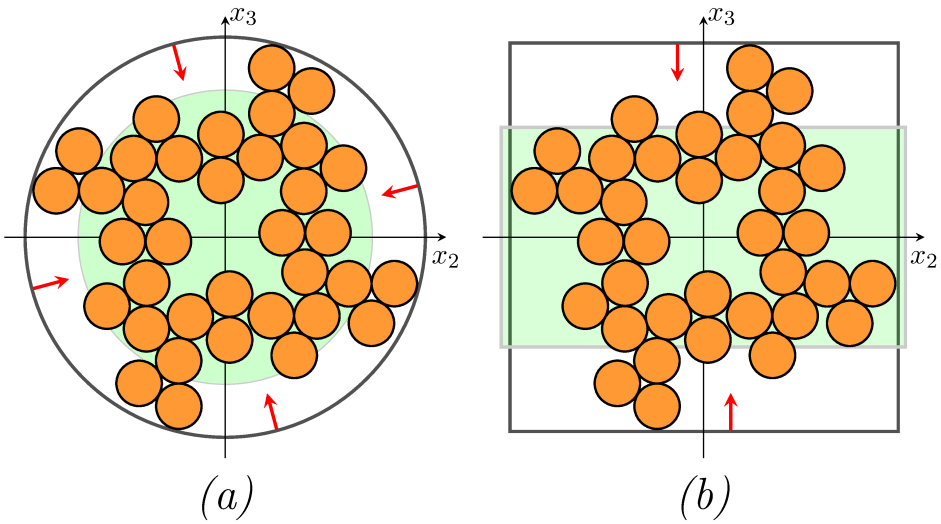

Figure 2.10: Circular (a) and rectangular (b) shrinking boundary.

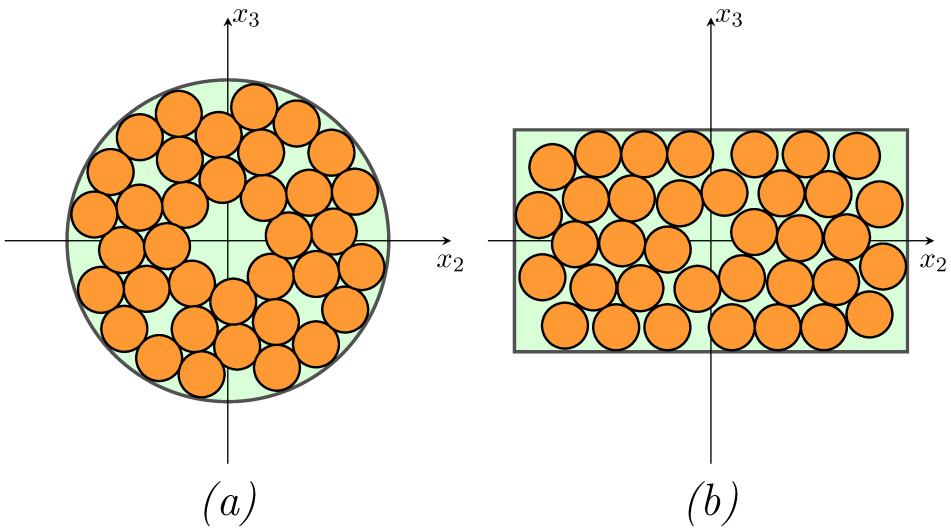

Figure 2.11: Circular (a) and rectangular (b) final boundary.

with respect to the boundary surface. As a consequence of these boundary forces $\mathbf{F}_{\mathrm{i,bound}}$, the outermost strands tend to move inwards to the transverse direction creating new interferences with the adjacent inner strands which in turn are forced towards the centre of the bundle. Since the same iterative method presented in 2.3.2 is adopted, the forces and the stiffness derived from both strand-strand and strand-boundary contacts are considered. The resulting displacement of the *i-th* strand becomes:

$$\mathbf{S}_{\mathrm{i}}(x_1) = \frac{\mathbf{F}_{\mathrm{i,Tot}}(x_1)}{K_{\mathrm{i,stra}}(x_1)}, \tag{2.16}$$

where

$$\mathbf{F}_{\mathrm{i,Tot}}(x_1) = \mathbf{F}_{\mathrm{i,stra}}(x_1) - \mathbf{f}_{\mathrm{n,i}}(x_1) + \mathbf{F}_{\mathrm{i,bound}}(x_1)\,. \tag{2.17}$$
$$\tag{2.18}$$

When all the interferences appear on the current bundle cross-sections have reached the minimum non-interference value, the external boundary is shrinked again.

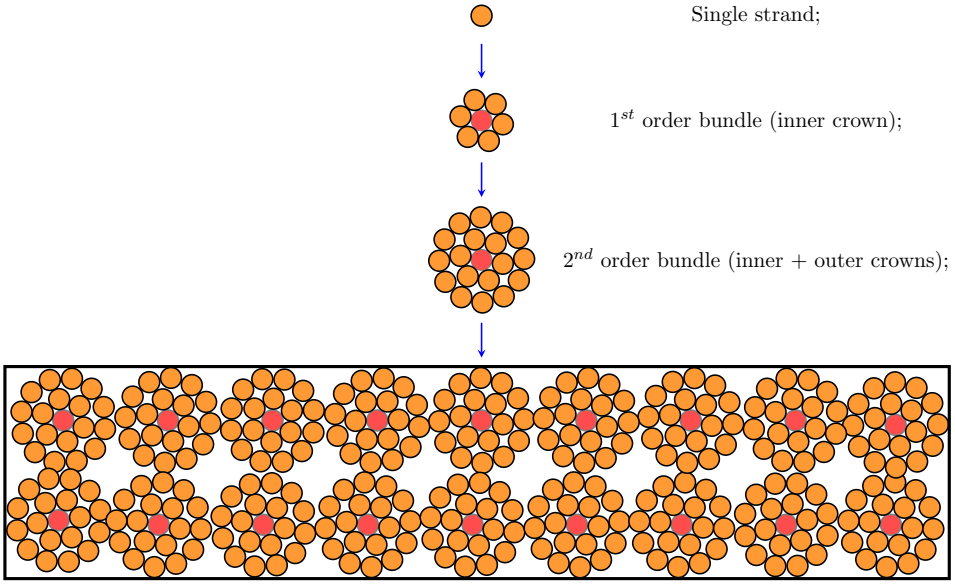

Figure 2.12: 2D sketch of a multi-stage Rutherford cable layout.

2.4 New geometrical model improvement for multi-stage Rutherford-like cables

The new geometrical model has also been adapted to make the strands coordinates calculation possible also for cables with a Rutherford-like geometry, i.e. planar cables arranged on two layers, in which transposed strands are replaced by bundles. This cable layout for fusion application has been adopted for instance in the RW prototype for the DEMO TF conductor [41], in which each sub-cables is composed by two "crowns" of strands which are twisted around a central strand with a proper pitch (see Figure 2.12).

A first attempt to model this kind of cables has been made with the model of Section 2.3. However, the final compaction procedure applied to the whole conductor did not give satisfactory result. The cable cross-section at the end of the last stage of cabling, i.e. before the final compaction down to the rectangular shape, is shown in Figure 2.13: the sub-cables are arranged on a cylindrical surface with a relatively large diameter compared to the one of the single bundle. As a consequence of this, during the first part of the compaction procedure, the strands are forced to move towards the cable middle plane, and only in a later phase they would be actually compacted. Due to this, and to the simplifying structural model, whole bundles tend to locally jump over the others because of the high level of compaction. It must be noticed that similar

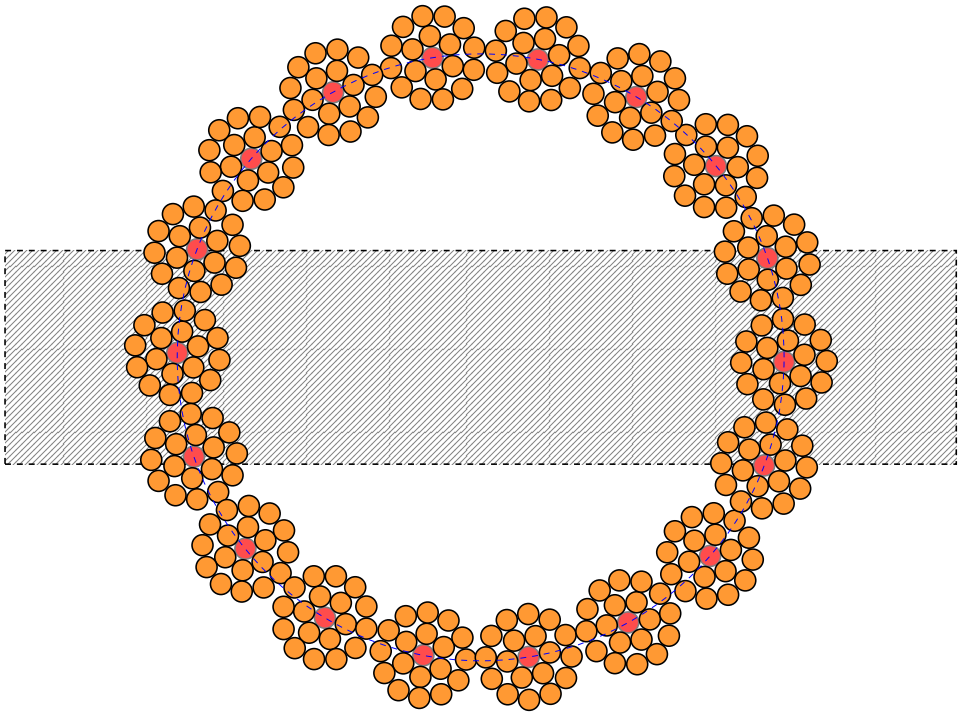

Figure 2.13: Cable cross-section at the end of the last stage of cabling procedure. The dimensions of the desired final cable cross-section are also picked up by the gray dashed area.

effect would occur during compaction in the real manufacturing process. This is avoided thanks to a suitable inner mould in the cabling zone.
To model this kind of cables, a different strategy has therefore been adopted, and the THELMA geometrical model previously developed for classic Rutherford cables made up of two layers of strands, has been used in order to optimize the modeling of multi-stage Rutherford-like cables. Both models are outlined in the following two sections.

2.4.1 Rutherford Cable

The geometrical model dedicated to the computation of the strands axis coordinates of a Rutherford cable was already developed for the THELMA code, as described in detail in [5] and summarized here for clarity purposes. It is an analytical based model built up by some geometrical parameters listed in Table 2.1 and shown in Figure 2.14 [5]. The following relations hold:

$$k = \arctan\left(\frac{\omega_{\mathrm{M}} - \omega_{\mathrm{m}}}{2h}\right) = \frac{\alpha}{2}\,, \tag{2.19}$$

Table 2.1: Main geometrical parameters of the Rutherford cable cross-section.

Parameter	
h^e	external height
ω_m^e	min. external width
ω_M^e	max. external width
h	middle layer height
ω_m	min. middle layers distance
ω_M	max. middle layers distance

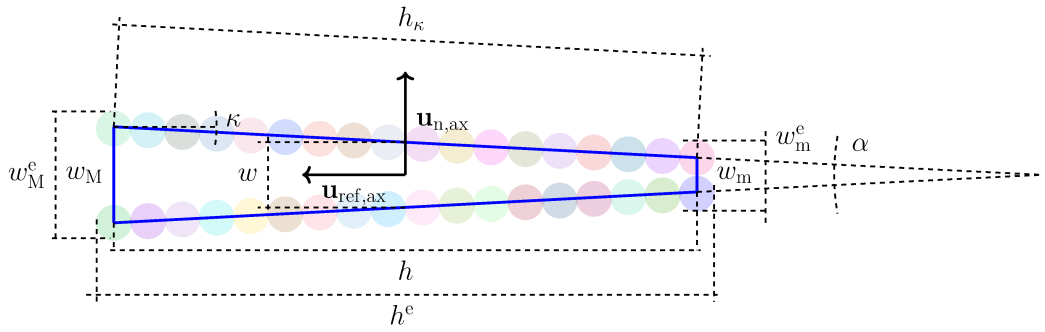

Figure 2.14: Schematic of a keystoned Rutherford cable cross-section to point out all the model geometrical parameters [5] (courtesy of Giulio Manfreda).

$$\omega = \frac{\omega_{\mathrm{M}} + \omega_{\mathrm{m}}}{2}\,, \tag{2.20}$$

$$h_{\mathrm{k}} = \frac{h}{\cos k}. \tag{2.21}$$

To calculate the coordinates of each strand along the cable axis, two models can be used:

1. *Piece-Wise linear* model;
2. *Smoothed* model.

The first one is a preliminary simplified model that calculates the strands trajectories by considering three different regions depending on the curvilinear coordinate. Indeed, since in the cable cross-section the strands describe an isosceles trapezoid (the blue line in Figure 2.14) because of the keystoning angle α, one set of equations can be written for the strands crossing the largest short-edge cable face, one for the strands laying on the long-edge cable face, and another for the strands crossing the smallest short-edge cable face. In case of a non-keystoned Rutherford cable, only two sets of equations are needed to describe the two different regions, i.e. the short-edge and the long-edge cable faces. However, the simplified model leads to discontinuities when the strand moves from one region to the following one along the cable. For this reason, the smoothed model was developed to remove the discontinuities through suitable circle arcs.

2.4.2 Multi-stage Rutherford cable

The model outlined above has been combined with the new one described in Section 2.3 in order to achieve the generation of a multi-stage Rutherford cable geometry. All the bundles up to the last-but-one stage are prepared according to the cabling sequence described in Section 2.3. When all the last-stage subcables undles have been twisted, the Rutherford cable model is used to create their axes in the final cable starting from the input geometrical parameters of Table 2.1 (see Figure 2.15). The equivalent outer diameter of the bundles is considered to set the pre-compaction geometry, as shown in Figure 2.16. Once that the axes have been analytically generated, the coordinates of each strand previously referred to the subcable reference frame, are then referred to the cable main reference frame. At the end, the compaction procedure is applied to the whole cable to achieve the final cross-section sizes as described in Section 2.3.4.

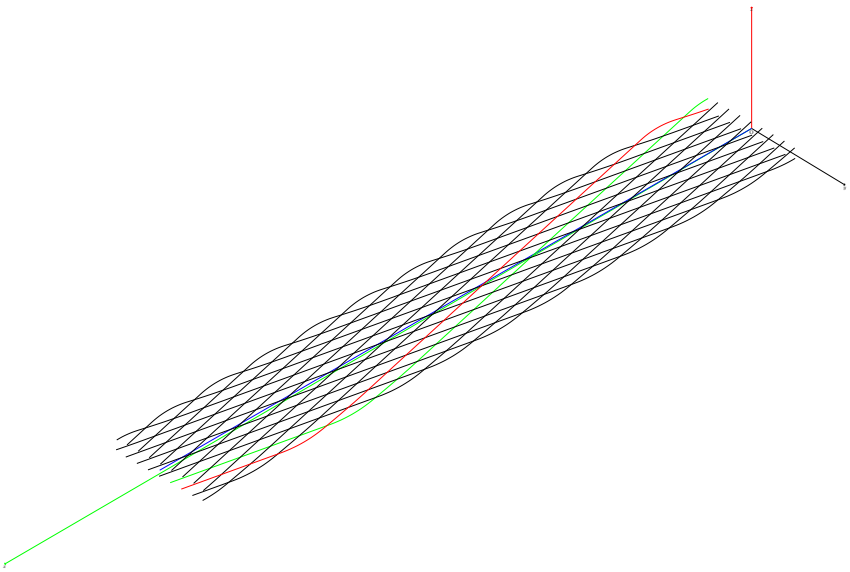

Figure 2.15: 3D sketch of the new sub-bundle axes created for the last stage of cabling of a multi-stage Rutherford cable.

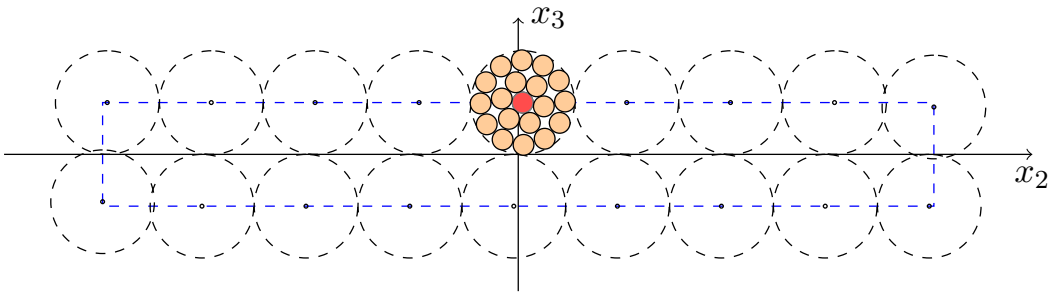

Figure 2.16: Cross-section of the new sub-bundle axes created for the last stage of cabling of a multi-stage Rutherford cable. For each axis, the equivalent diameter of the corresponding sub-bundle is considered.

Chapter 3

Contact resistances analysis

3.1 Introduction

In a superconducting cable, even if it is generally possible to consider the longitudinal resistance of the strands as null, the transverse resistance experienced from the current transfer from one strand to the neighboring one is not negligible. These resistances, called *inter-strand*, represent the effect of the contact between different strands which have been twisted together and compacted. The inter-strand resistances play a key role regarding the superconducting cables behavior: large values are underside since, in case of a localized electromagnetic disturbance, they do not allow the current redistribution among the strands; on the other hand, too low values of contact resistances are also unwanted since they facilitate the induced currents due to a variable regime, leading to significant coupling loss dissipated inside the conductor which may negatively influence the cable thermal stability [42][43][44]. Several factors may affect the inter-strand resistances, such as the actual contact area which depends on the geometry and the applied load [45], or the presence of resistive barrier on the strand surface of the strand due to a thin oxide layer [46] or an external coating [47] suitably adjusted to better control the distribution of the resistances. Sometimes, for the same purpose, a resistive stainless steel strip is also interposed between the two layers of a Rutherford cable or, in case of a CIC conductor, is wrapped around the petals.

3.1.1 Multi-stage conductors

The complexity and the randomness of the strands geometry due to the arbitrary angular positions of the strands in a multi-stage cable bundles, and to the cabling process uncertainties, does not allow the employment of feasible theoretical models to describe a priori the contact resistances distribution

inside the conductor. Nevertheless, this aspect strongly influences the cable stability and the energy dissipation inside the conductor by the current redistribution and the induced current loops formation. For this reason, dedicated measurements are usually carried out on cable samples to analyze the inter-strand resistances. These tests are performed by specific devices, e.g. the *Twente Cryogenic Press* [48], in which pairs of strands chosen among all the cabling stages are fed in turn, starting from two strands of the same triplet up to couples of strands belonging to different petals. If necessary, the cable is mechanically loaded with a transverse compression. For each pair of strands, if v is the measured voltage [V] and I the measured current [A], then the equivalent contact resistance per unit length r_c [Ωm] is derived as follow:

$$r_c = \frac{v}{I} L \,, \tag{3.1}$$

where L is the sample axial length that should be not less than the twist pitch of the last stage of cabling.
Typical values of r_c are in rage from 1 to some hundreds of nΩm according to the cabling stage but, given the strand layout and the geometry of the cable, they strongly depend on the applied force and mechanical cycling load. Even if r_c tends to decrease with the applied load because of the pressure undergoes by the strands that improves the contacts, for a given load, it saturates after thousand of cycles [49][44][50]. Usually, the resistances measured between two strands of the same petal are referred to as *intra-petal* resistances per unit length $r_{c,intra}$ [Ωm], whereas two strands belonging to different petals are in contact through the so called *inter-petal* resistances per unit length $r_{c,inter}$ [Ωm].

3.2 Inter-Strand Resistances in the THELMA Code

The THELMA code is able to simulate the contact resistances measurement by means of the *linear lumped network* model developed by the University of Udine, referred to as *Udine EM Module*, which describe superconducting cables, joints and terminations in conditions far from the critical surface ($J << J_c$, $B << B_c$, $T << T_c$). The inter-strand contact model is also utilized, according to which the strand resistivity parameters have to be assigned. Both the Udine EM and the contact models are described in the following sections.

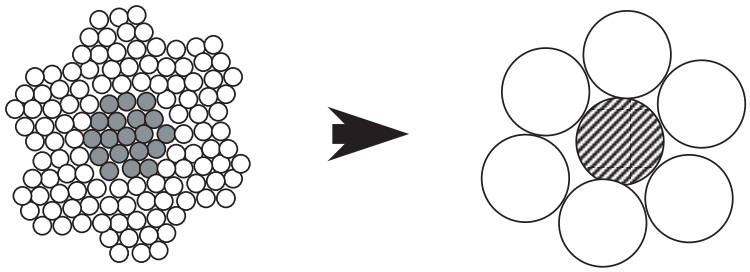

Figure 3.1: Equivalent macrostrands obtained starting from a bundle of strands.

3.2.1 Udine EM model

The electromagnetic model generates the equivalent network of the strands once that the cable geometry has been created, as described in detail in [33]. To simplify the system by reducing the number of unknowns, cable bundles can also be grouped in equivalent macrostrands/cable elements (CEs) as shown in Figure 3.1. The axis geometry of each macrostrand is computed as the barycentric line of all the strands represented by the macrostrand. The N_{ce} strands/macrostrands of the conductor are discretized into a suitable number of longitudinal elements N_{em}, each characterized by a value of current. In each longitudinal elements the current density is supposed uniform. In the equivalent network, the superconducting strands are modeled in a different way with respect to the resistive ones, i.e. copper strands: purely inductive components are used to represent the superconducting elements, whereas a non-negligible longitudinal resistance is also added to the resistive segments. In this way, it is possible to generate a linear inductive network N-ports by computing the self and mutual inductance coefficients through an integral method based on the cable element geometry. Moreover, several additional components have been implemented in the code that may be considered in the network, e.g. current or voltage sources. As an example, Figure 3.2 shows a part of an equivalent network composed of four longitudinal elements.

The network is solved in the time domain thanks to the *modified node analysis* (MNA) method in which the unknowns are:

- all the *node potentials*, but one whose potential value is assigned;
- all the *currents* in the ports of the current-driven components.

If the Kirchhoff's laws and the component voltage-current characteristics are applied to a general case, the following system can be written:

$$\begin{pmatrix} \mathbf{A} & \mathbf{R} \\ \mathbf{G} & \mathbf{B} \end{pmatrix} \cdot \begin{pmatrix} \mathbf{V} \\ \mathbf{I} \end{pmatrix} + \begin{pmatrix} \mathbf{0} & \mathbf{M} \\ \mathbf{C} & \mathbf{0} \end{pmatrix} \cdot \frac{\mathrm{d}}{\mathrm{d}t} \begin{pmatrix} \mathbf{V} \\ \mathbf{I} \end{pmatrix} = \begin{pmatrix} \mathbf{E} \\ \mathbf{J} \end{pmatrix}, \tag{3.2}$$

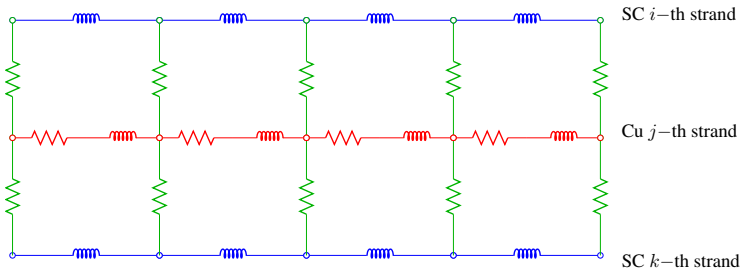

Figure 3.2: Detail of an equivalent electrical network with four longitudinal elements of two superconducting strands (in blue) and one resistive strand (in red). The contact resistances (in green) are also drawn.

where $\mathbf{A}$ and $\mathbf{B}$ are the branch and nodal incidences matrices, $\mathbf{R}$ and $\mathbf{G}$ are the matrices of the self and mutual resistances respectively, $\mathbf{E}$ and $\mathbf{J}$ are the arrays of the known impressed e.m.f.s and currents and $\mathbf{V}$ and $\mathbf{I}$ are the arrays of unknown potentials and currents. To conclude, $\mathbf{M}$ is the matrix of the self and mutual inductances and $\mathbf{C}$ is the matrix of the capacitances which is not considered in this type of analysis ($\mathbf{C} = 0$).
Since (3.2) is an algebraic-differential system with state variables or simple unknown quantities, the system can be rewritten by organizing the equations and unknowns so that algebraic equations and the simple unknowns are considered first. It follows:

$$\underbrace{\begin{pmatrix} \mathbf{D}_{S_{\mathrm{aa}}} & \mathbf{D}_{\mathrm{S_{ad}}} \\ \mathbf{D}_{\mathrm{S_{da}}} & \mathbf{D}_{\mathrm{S_{dd}}} \end{pmatrix}}_{\mathbf{D}_{\mathrm{S}}} \cdot \underbrace{\begin{pmatrix} \mathbf{X}_{\mathrm{Sa}} \\ \mathbf{X}_{\mathrm{S_d}} \end{pmatrix}}_{\mathbf{X}_{\mathrm{S}}} + \underbrace{\begin{pmatrix} \mathbf{0} & \mathbf{0} \\ \mathbf{0} & \mathbf{F}_{\mathrm{S_{dd}}} \end{pmatrix}}_{\mathbf{F}_{\mathrm{S}}} \cdot \frac{\mathrm{d}}{\mathrm{d}t} \begin{pmatrix} \mathbf{X}_{\mathrm{S_a}} \\ \mathbf{X}_{\mathrm{S_d}} \end{pmatrix} = \underbrace{\begin{pmatrix} \mathbf{Y}_{\mathrm{S_a}} \\ \mathbf{Y}_{\mathrm{S_d}} \end{pmatrix}}_{\mathbf{Y}_{\mathrm{S}}}, \quad (3.3)$$

where $\mathbf{X}_{\mathrm{S}}$ is the array of the sorted unknowns, $\mathbf{Y}_{\mathrm{S}}$ is the array of the sorted known terms, $\mathbf{F}_{\mathrm{S}}$ and $\mathbf{D}_{\mathrm{S}}$ are the sorted matrices. The first sub-subscript is "a" for the algebraic equations and "d" for the differential ones, whereas the second sub-subscript is "d" for the unknown state variables and "a" for the other case. If $\mathbf{X}_{\mathrm{Sa}}$ is derived from the algebraic equations and replaced in the differential ones, it turns out that:

$$\frac{\mathrm{d}\mathbf{X}_{\mathrm{S_d}}}{\mathrm{d}t} = \mathbf{F}_{\mathrm{S_{dd}}}^{-1} \left[\mathbf{Y}_{\mathrm{S_d}} - \mathbf{D}_{\mathrm{S_{da}}} \mathbf{D}_{\mathrm{S_{aa}}}^{-1} \mathbf{Y}_{\mathrm{S_a}} + \left(\mathbf{D}_{\mathrm{S_{da}}} \mathbf{D}_{\mathrm{S_{aa}}}^{-1} \mathbf{D}_{\mathrm{S_{ad}}} - \mathbf{D}_{\mathrm{S_{dd}}} \right) \mathbf{X}_{\mathrm{S_d}} \right] \quad (3.4)$$

The system matrices are constant with time because of the equations linearity. The LU matrix factorization can be used to invert $\mathbf{D}_{\mathrm{Saa}}$ and $\mathbf{F}_{\mathrm{Sdd}}$ to improve the solution efficiency. To numerically solve the system of ordinary differential equations, a suitable Runge-Kutta method is then applied.
The MNA approach is very efficient when dealing with networks made of

voltage-controlled components, since all the contacts can be represented also in terms of contact conductances, as for the steady-state analysis presented in Section 3.3. In the end, the MNA is also very efficient when the THELMA equivalent thermal network is analyzed, in which the temperatures correspond to node potentials [51]. Presently, the *modified loop analysis* method is going to be implemented in the code to study networks in which both voltage and current controlled components are present.

3.2.2 Contact model

To compute the inter-strand resistances, the vertical ones in Figure 3.2, a contact model must be chosen. The original contact model already developed for the THELMA code is based on two strand parameters and an additional one [33]:

- the *strand spot contact resistance* R^s_{st} [Ω] used for occasional spot-like contacts along the cable axis, as it is e.g. for couples of strands of different bundles;
- the *strand distributed contact resistance* r^d_{st} [Ωm] used for contacts that are supposed to be uniform along the cable axis, like the contact between two strands of the same triplet;
- the *stainless steel spot additional contact resistance* $R^s_{\mathrm{SS_a}}$ [Ω] used to account for the possible contribution of the petal wrapping.

This model, referred to as *(0D+1D) model*, has been validated [33] and used for several analyses and showed a good capability to reproduce the experimental results [38][52]. However, the new cable model described in Section 2.3.4, that represents the inter-strands geometrical contact in a more realistic way, avoiding strands overlapping, gave the opportunity to implement a new inter-strand contact model, referred to as *2D model*, based on 2D contacts. With this model, it is now possible to estimate the local width w of the area of each contact (see Figure 3.3): generally, when two strands are in contact, the contact width is not uniform, having the contact surface an almost elliptical shape [39], and, if the two strands are *quasi parallel*, i.e. the angle between the incident strands is small, the contact surface length is comparable or even much longer than the strands diameters. In these conditions the contact width is a function of the curvilinear coordinate s along the strands, and a variable contact resistance per unit length $\varrho_{\mathrm{c}}/w(s)$ is considered, so that the overall contact resistance per unit length $r_{\mathrm{c,2D}}$ [Ωm] computed with the 2D model can

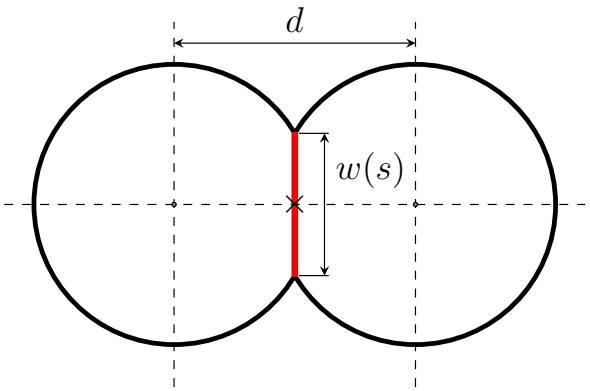

Figure 3.3: Detailed view of the interstrand contact cross-section, showing the distance d and the contact surface width w at the curvilinear coordinate s along the contact.

be expressed as:

$$r_{\mathrm{c,2D}} = \frac{\varrho_{\mathrm{c}}}{\int w(s)\,\mathrm{d}s} L\,, \tag{3.5}$$

where ϱ_{c} [$\Omega\mathrm{m}^2$] is the new *strand 2D contact resistivity* parameter. As shown in Figure 3.3, the contact width is computed directly from the distance d between the strands centres, assuming circular strands cross-sections and neglecting any strand radius change. The following relation is considered:

$$w = \sqrt{D_0^2 - d^2}\,, \tag{3.6}$$

where D_0 is the strands original diameter. With this contact model, if two strands are simply in touch with a negligible interferences, the contact would not be taken into account. In fact, for $w \approx 0$ it follows that $r_{\mathrm{c,2D}} \to \infty$, but, actually, an electric contact with a finite $r_{\mathrm{c,2D}}$ can be present as well albeit with much higher resistance. For this reason, a minimum width w_0 value has been introduced as a model parameter in order not to neglect minor contacts and also to represent, in a very rough way, possible non linearities of the contact conductances with the width. As for the old (0D+1D) model, an additional *stainless steel resistivity* $\rho_{c,steel}$ [$\Omega\mathrm{m}^2$] has been defined in the 2D model as a parameter, to be used when stainless steel petal wraps or strip are present in the cable.
Once that the model parameters have been set, a specific routine calculates the location of the contacts, the length and the width of the contacts surface by considering the distance between one strand and all the others along all the cable axis.

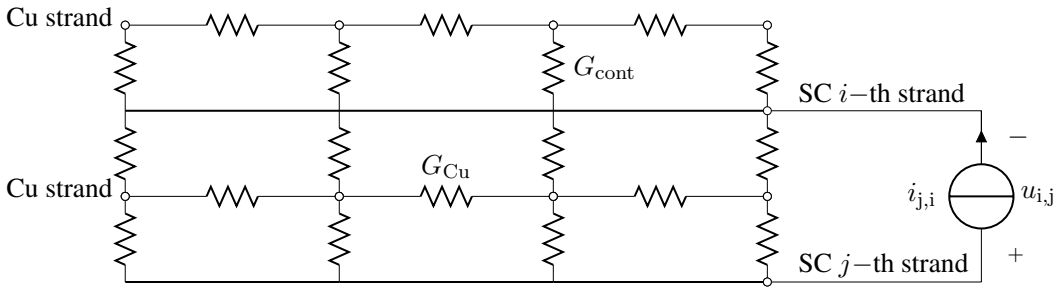

Figure 3.4: Sketch of a simplified network used to model the inter-strand resistance measurement. The current generator, the contact conductance $\mathrm{G_{cont}}$ and the longitudinal conductances $\mathrm{G_{Cu}}$ of the copper strands are shown.

3.3 Numerical Analysis of Inter-Strand Resistances

Thanks to the Udine EM model and the inter-strand contact models, the measurement of contact resistances can be simulated with the THELMA code: the equivalent network is indeed completed with the installation of a current generator to the i_{th} and j_{th} superconducting strands of interest, as shown in Figure 3.4, and then the system of equations (3.2) is solved. To simplify the system, the superconducting strands are considered as zero longitudinal resistance elements so that all the nodes of a single strand can be merged together resulting in one potential for each strand. This can be done since a steady state analysis is considered, i.e. no inductances are involved. Moreover, to strongly improve the solution efficiency, all the network resistive components have been represented in terms of conductances, i.e. voltage controlled components, so that the modified nodal approach can be adopted without unnecessary increasing the set of unknowns with the resistor currents. In this way a symmetric system matrix can be obtained, so that iterative methods like BiCGStab [53] can be used. In the following sections, the contact resistances distributions of two cable prototype which have been proposed for the DEMO TF coil are analyzed. The samples geometry has been modeled with the new geometrical model and the inter-strands resistances have been computed by considering the new 2D contact model.

3.3.1 Contact resistances analysis: DEMO - WR WP2

One of the cables proposed for the DEMO toroidal field coils is presently being developed by ENEA [54][34]. It is the Winding Pack 2 (WP2) conductor

Table 3.1: Main geometrical parameters of the WR WP2 [34].

Parameter	Value
Operating current [kA]	81.7
Effective magnetic field [T]	13
N. of SC strands	1080
N. of Cu strands	132
SC strand diameter [mm]	1.0
Cu strand diameter [mm]	1.5
Type-I petal layout	1SC×3×3×4×(5 + Core1)
Type-II petal layout	1SC×3×3×4×(5 + spiral)
Core1 layout	1Cu×3×4
Core2 layout	1Cu×3×4×(6 + Core1)
Cable layout	(4 type-I petals + 2 type-II petals) around Core2
Cable twist pitches [mm]	103/135/175/227/690
	Core1: 102/180
	Core2: 102/180/240
Cable external dimension [mm^2]	38.8 × 80.6
Spiral outer diameter [mm]	6.6
Spiral inner diameter [mm]	4.6
Void fraction in bundle	24.6%

based on the Wind&React (WR) technique. It consists of a CIC conductor with rectangular cross-section, designed to operate at 82 kA in a magnetic field of about 13 T and with a current sharing temperature $T_{cs} > 6.5$ K. The main difference between the WP2 and the ITER cables is not only the shape, being rectangular instead of circular, but also the strand type and the cable layout. The superconducting Nb_3Sn strands, produced by the Chinese company *Western Superconducting Technologies* (WST) according to the internal tin process [55], have a diameter of 1.0 mm and Cu:nonCu ratio equal to 1. As described in Table 3.1, the cable is composed of 6 petals cabled together around a central core made of copper strands with a diameter of 1.5 mm and high value of RRR (>100) supplied by Luvata. Since forced Liquid-He flow as a coolant is adopted, two petals are formed by sub-petals wound around a central steel spiral that constitutes a cooling channels, whereas the other four contain a central core made of segregated copper strands. In order to guarantee a regular distribution of strands in the cable cross-section, in spite of the compaction down to a rectangular shape, a long twist pitch criteria has been chosen [56] [57], instead of the short twist pitch one adopted for the ITER Central Solenoid cable-in-conduit conductors [58] [59]. Moreover, petal

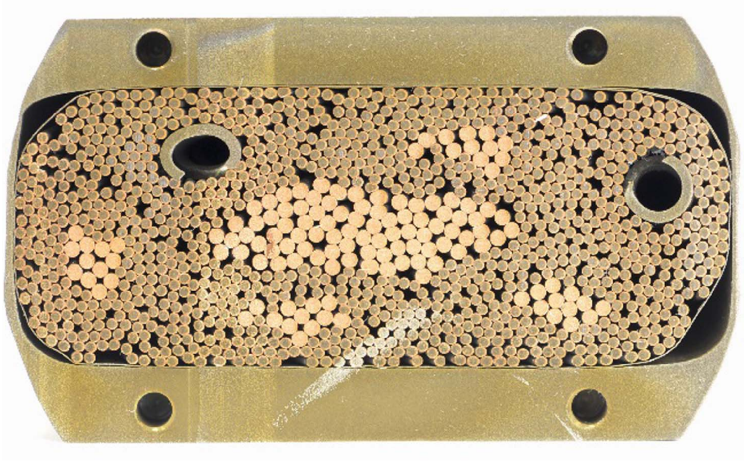

Figure 3.5: WR WP2 cross-section [6].

wraps are absent. A cross-section of the WR WP2 sample used for the contact resistances measurement is reported in Figure 3.5.

Contact resistances measurements

As described in detail in [6], the inter-strand resistances measurements have been carried out by the University of Twente in the Twente Press. A set of 20 pairs of strands was selected in order to find a significant resistance value for each cabling stage. In total, 10 combinations of non-equivalent resistances were identified, as shown in Figure 3 of [6] and summarized here in Table 3.2. The first 5 combinations correspond to the intra-petal $r_{c,intra}$, whereas those taken from stage 6 to the inter-petal $r_{c,inter}$. The resistances were measured with a 400 mm long sample at 4.2 K in liquid He bath, without background magnetic field, by feeding each pair of strands with a current of 50 A. The results of the contact resistances measurement obtained in virgin condition, i.e. before any application of cyclic loading, are shown in Figure 3.6. These date are kindly provided by A. Nijhuis from University of Twente.

Numerical analysis results

The experimental resistances values shown in Figure 3.6 have been assumed as target for the analysis. Since the trajectory of the strands inside the conductor, and therefore the occurrence of the contacts, depends on their initial position, the effect of the initial angular phase on the measurements results cannot be ignored [52]. For this reason, a number of 5 different cable samples are modeled that differ from each other only by the initial strands phase sets

Table 3.2: Strands couples combination for the contact resistances measurement of the WR WP2 [34].

Combination	Configuration
1) R_{st1}	Strands from the same triplet;
2) R_{st2}	Strands from the same 3×3 bundle;
3) R_{st3}	Strands from the same 3×3×4 bundle;
4) $R_{st4,a}$	Strands from the same 3×3×4×5 bundle, adjacent;
5) $R_{st4,na}$	Strands from the same 3×3×4×5 bundle, not adjacent;
6) $R_{st5,P2}$	Strands from Petal 1 - Petal 2;
7) $R_{st5,P3}$	Strands from Petal 1 - Petal 3;
8) $R_{st5,P4}$	Strands from Petal 1 - Petal 4;
9) $R_{st5,P5}$	Strands from Petal 1 - Petal 5;
10) $R_{st5,P6}$	Strands from Petal 1 - Petal 6.

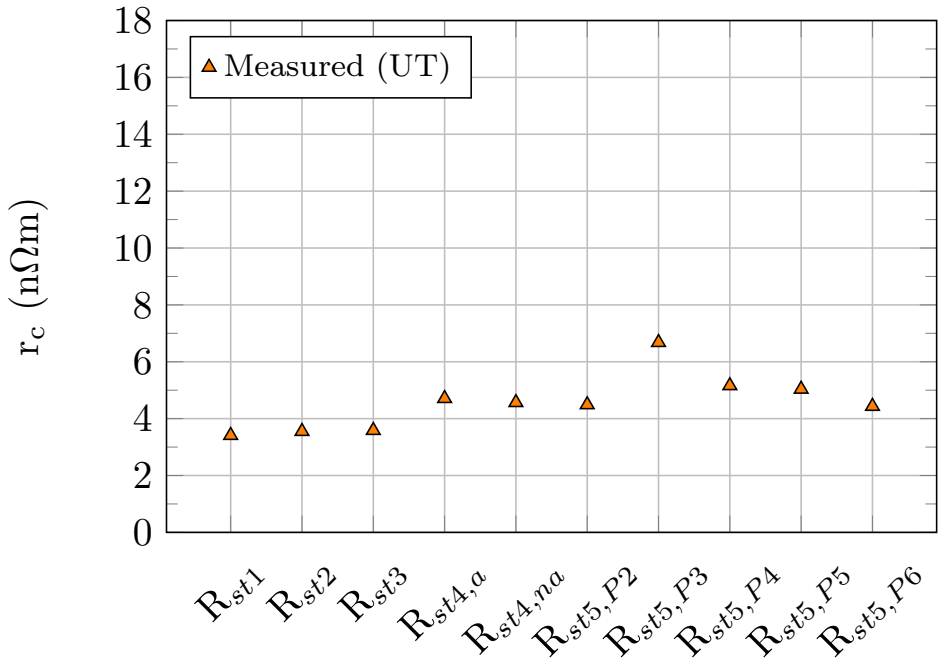

Figure 3.6: WR WP2 inter-strand contact resistances measured in virgin condition by the University of Twente (Courtesy of A. Nijhuis).

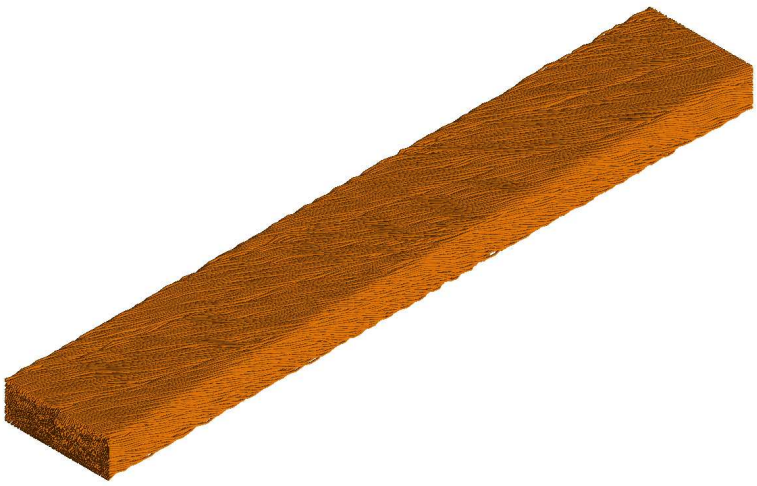

Figure 3.7: 3D sketch of the WR WP2 cable model.

that are generated as a random array $\boldsymbol{\Theta}$. The cooling channels have been modeled with bundles made of strands with high longitudinal and inter-strand contact resistivity. 3D view of one modeled sample geometry is shown in Figure 3.7, whereas a cable cross-section is reported in Figure 3.8. The aim of this study is therefore not only to try to reproduce the experimental results by means of a suitable tuning of the model parameters ϱ_c and w_0 (see Section 3.2.2), but also to investigate the model and the experimental results sensitivity to the strands initial phases. Only five samples have been considered because of the quite demanding and time-consuming simulations for the cable geometry modeling. For more detailed investigations of the effect of the strands initial phases, a statistical approach such that described in [52] could be used, which requires a much more numerous of different phase sets to be considered. For each sample, the same set of couples of strands is selected according to the measurement combination of Table 3.2.
A preliminary value of the minimum contact width was set as $w_0 = 0.2D_0$, where D_0 is the strand diameter, so that the only free parameter of the model was ϱ_c [Ωm^2]. Anyway an analysis of the effect of w_0 was carried out, as explained below. In particular, the best fit for this analysis is obtained by imposing $\varrho_c = 8.5{\cdot}10^{-13}$ Ωm^2 to all the strands, i.e. both the superconducting and resistive ones since their surface coating is the same. The mean values of resistances computed with the five samples are plotted and compared with the experimental ones in Figure 3.9. To investigate on the influence of the parameter w_0, the resistances have been also calculated by setting $w_0 = 0.0$, i.e. considering only the contacts between geometrically intersecting strands are

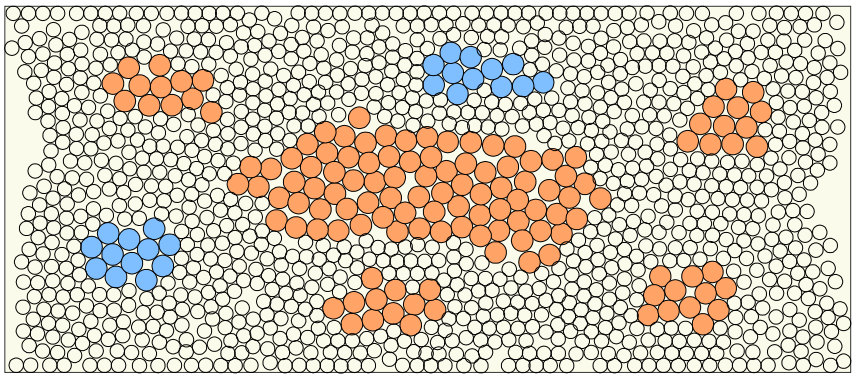

Figure 3.8: WR WP2 cross-section. The blue strands represent the cooling channels whereas the orange ones correspond to the copper strands.

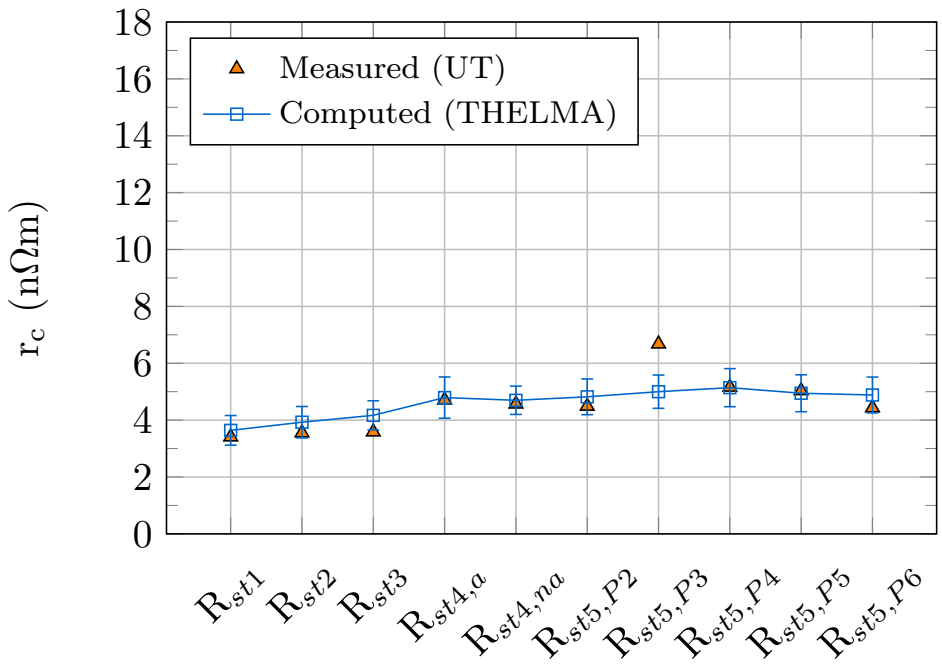

Figure 3.9: WR WP2 contact resistances in virgin condition: comparison between the measured ones and the mean ones computed with the THELMA code by considering a number of 5 samples modeled with different initial angular phases. The line is a guide for the eye.

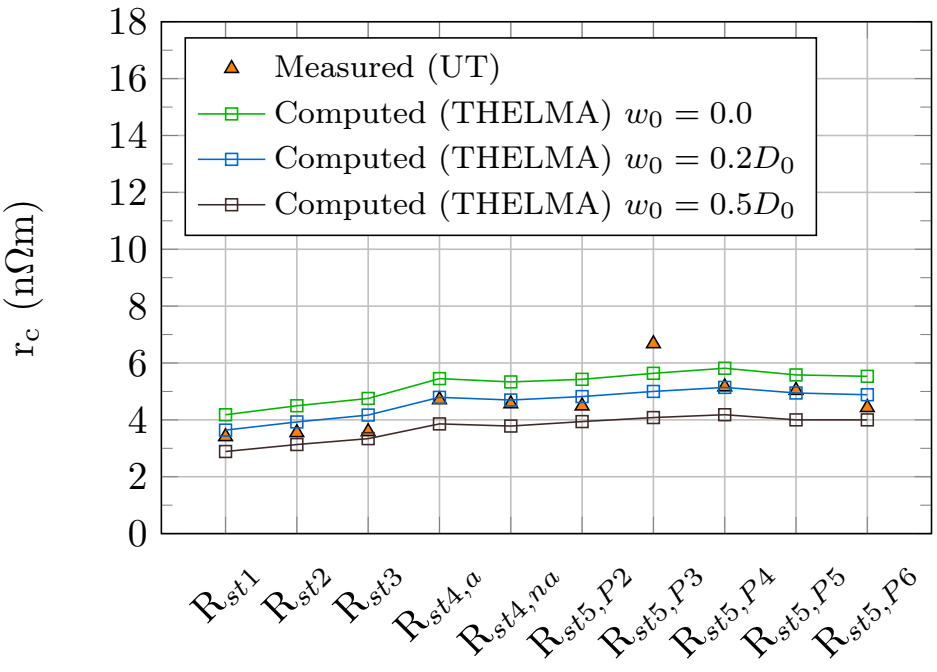

Figure 3.10: WR WP2 contact resistances in virgin condition: comparison between the measured ones and the mean ones computed with the THELMA code by considering a number of 5 samples modeled with different initial angular phases. The numerical results have been obtained with three different values of w_0.

considered, and $w_0 = 0.5D_0$: as can be seen in Figure 3.10, the overall trend of the resistances distribution does not change significantly, although it increases or decreases inversely with w_0 because of a smaller or larger minimum contact surface considered.

3.3.2 Contact resistances analysis: DEMO - RW1 WP1

Another cable that has been proposed for the DEMO toroidal field coils is the Winding Pack 1 (WP1). It is being developed by the Superconductivity Group of the Swiss Plasma Center (SPC) and, differently from the WR WP2, it is based on the React&Wind technology. Since this conductor is described in Chapter 5, only the main characteristics of its geometric layout are given here. It is a multi-stage Rutherford-like cable made of 17 sub-cables referred here as petals, since represent the sub-bundles of the last stage of cabling. The Nb_3Sn superconducting strands are produced by WST with the internal

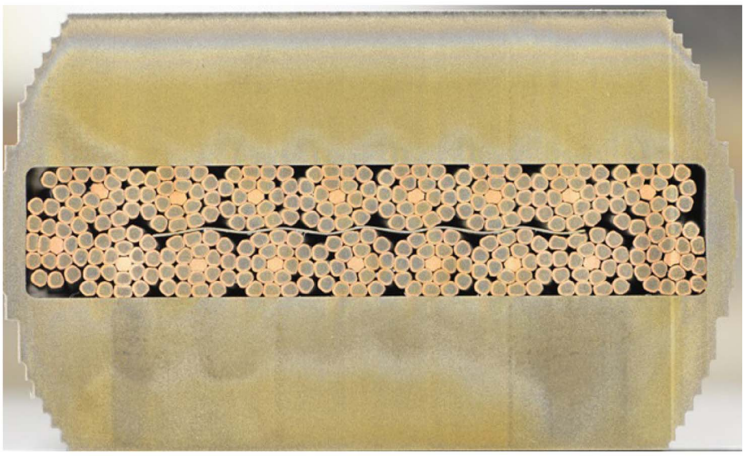

Figure 3.11: RW1 WP1 cross-section [6].

Table 3.3: Main geometrical parameters of the RW1 WP1 [7].

Parameter	
Operating current [kA]	82.4
Effective magnetic field [T]	13.5
N. of SC strands	306
N. of Cu strands	17
SC strand diameter [mm]	1.5
Cu strand diameter [mm]	1.5
Cable layout	(1Cu+6SC+12SC)×17
Cable twist pitches [mm]	90/190/-595
Cable inner dimension [mm^2]	11.9 × 62.1
Void fraction in bundle	20%

Sn technology and have a diameter of 1.5 mm. Three stages of cabling are applied in total to the conductor, so that the petals are composed by two crowns of strands that are twisted one around the other with two different twist pitches. As regards the last stage of cabling, the negative twist pitch and the presence of a central resistive strip are aimed at reducing the coupling currents loss. Most of the copper needed for the cable stabilization is not in the form of strands, but it is arranged around the conductor as shown in Chapter 5. The cable cross-section is shown in Figure 3.11 whereas the main features of the conductor are summarized in Table 3.3.

Table 3.4: Strands couples combination for the contact resistances measurement of the RW1 WP1 [7].

Combination	Configuration
1) $R_{st1,a}$	Strands from inner crown, adjacent;
2) $R_{st1,na}$	Strands from inner crown, not adjacent;
3) $R_{st1,o}$	Strands from inner crown, opposite;
4) R_{st2}	Strands from outer crown;
5) $R_{st3,P2}$	Strands from Petal 1 - Petal 2;
6) $R_{st3,P3}$	Strands from Petal 1 - Petal 3;
7) $R_{st3,P5}$	Strands from Petal 1 - Petal 5;
8) $R_{st3,P7}$	Strands from Petal 1 - Petal 7;
9) $R_{st3,P8}$	Strands from Petal 1 - Petal 8;
10) $R_{st3,P9}$	Strands from Petal 1 - Petal 9.

Contact resistances measurements

The inter-strand resistances measurements of the RW1 WP1 were also carried out in the Twente Press by researches from the University of Twente [7]. The measurements conditions were the same ones adopted for the WR WP2, so a 400 mm long sample was prepared and tested at 4.2 K in liquid He bath, without background magnetic field. Since the cabling layout is different from the CICC proposed by ENEA, the combinations of strands considered for the resistance measurement was different, as visible in Figure 2 of [6] and reported here in Table 3.4. In this case, the first 4 strands combinations correspond to the intra-petal $r_{c,intra}$, whereas the last 6 combinations refer to the inter-petal $r_{c,inter}$. The values of contact resistances measured with the sample in virgin condition are reported in Figure 3.12. Two remarks can be made:

- The intra-petal resistances measured on RW sample are lower than those measured on the WR sample: the minor number of strands and cabling stages probably result in a more regular strands distribution along the cable axis, so the strands tend to remain closer to each other;

- the inter-petal resistances measured on RW sample are higher than those measured on the WR sample: this is due to the presence of the central stainless steel strip; the WR sample is indeed characterized by no petal wraps.

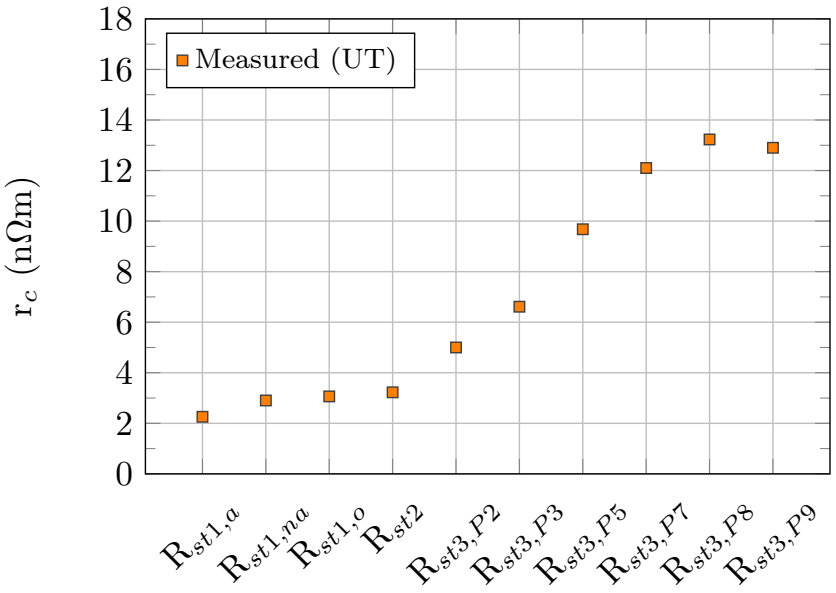

Figure 3.12: RW1 WP1 inter-strand contact resistances measured in virgin condition by the University of Twente [7].

Numerical analysis results

For the RW1 WP1 contact resistances analysis, ten samples 400 mm long have been modeled by considering ten phase sets. 3D view of the cable model geometry is shown in Figure 3.13, whereas a cable cross-section is drawn n Figure 3.14. Since the superconducting strands used for both the RW and WR conductor have the same layout except for the outer diameters, it is reasonable to expect the strand 2D resistivity parameters to be about the same for both the samples. For this reason, the starting value adopted for the inter-strand resistances calculation was $\varrho_c = 8.5{\cdot}10^{-13}$ Ωm^2, with a minimum contact width set equal to $0.2D_0$ again. In this case, to simulate the presence of the central strip, an additional resistance is therefore assigned to the strands that are positioned on the two different layers of the cable, according to the model parameter $\rho_{c,steel}$. For the present analysis, the stainless steel resistivity was set as $\rho_{c,steel} = 1.0{\cdot}10^{-9}$ Ωm^2. The mean values of contact resistances computed from all the samples with the THELMA code are plotted in Figure 3.15 and compared with the measured ones.

The intra-petal resistances obtained with the THELMA code and the new contact model are in a very good agreement with the experimental ones, whereas the computed inter-petal resistances are quite lower than the measured ones. This result is probably attributable to the pronounced anisotropy of the con-

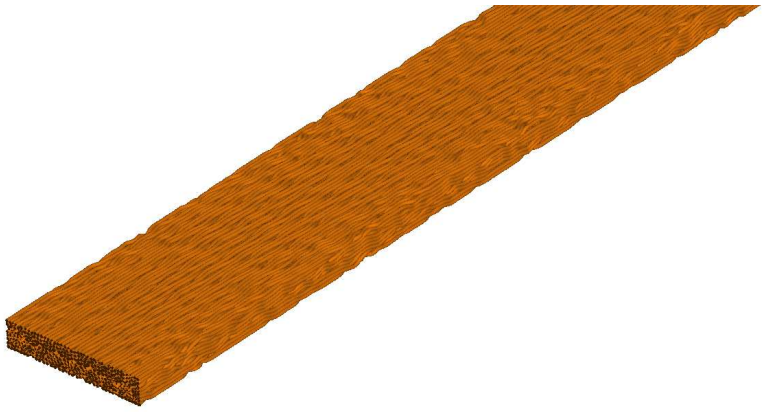

Figure 3.13: 3D view of a part of the RW1 WP1 cable model.

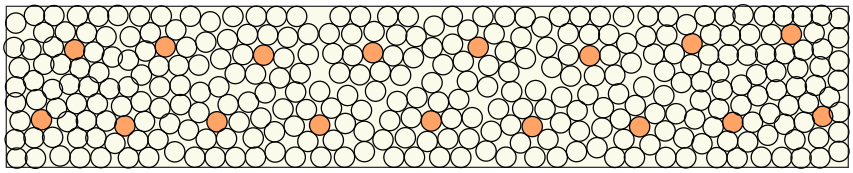

Figure 3.14: RW1 WP1 cross-section. The orange strands correspond to the copper strands.

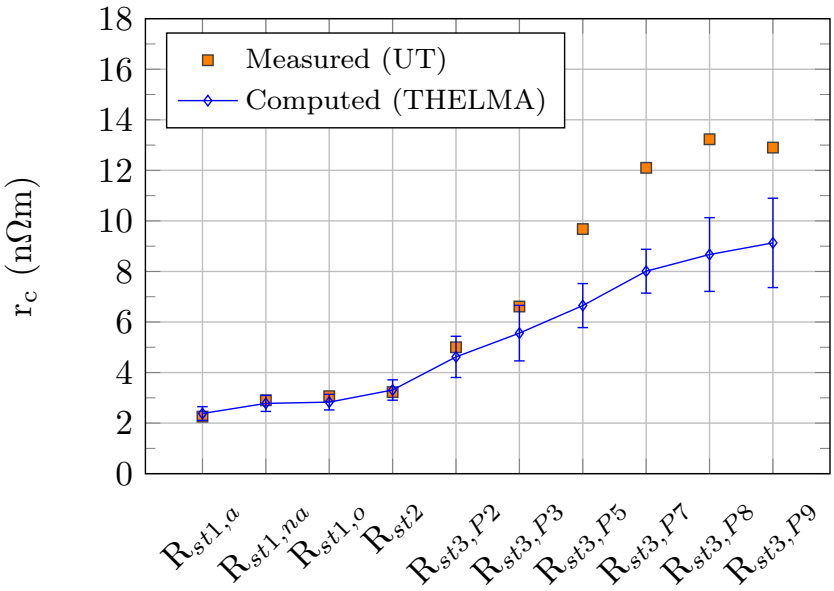

Figure 3.15: RW1 WP1 contact resistances in virgin condition: comparison between the measured ones [7] and the mean ones computed with the THELMA code by considering a number of 10 samples modeled with different initial angular phases. The line is a guide for the eye.

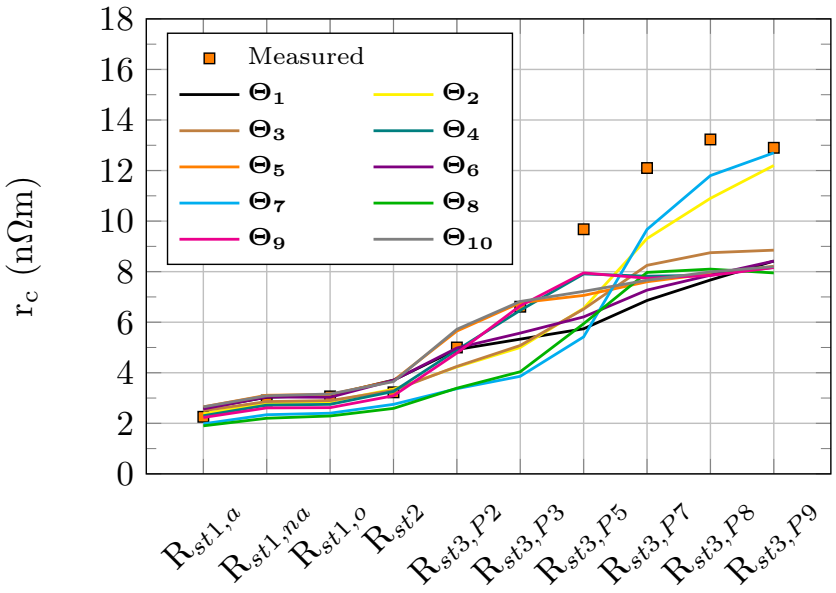

Figure 3.16: RW1 WP1 contact resistances in virgin condition: comparison between the measured ones [7] and the ones computed with the THELMA code by considering a number of 10 samples modeled with different initial angular phases. The line is a guide for the eye.

ductor that strongly increase the dependence of the inter-petal resistances on the strands initial angular phase. In fact, the standard deviation of the mean computed values of $r_{c,intra}$ is small since the strands of the same 2^{nd} order bundles have a regular distribution along the cable length, whatever the initial positions. Instead, the arrangement of the petals strongly affects the final resulting $r_{c,inter}$, as visible in Figure 3.16 where two angular phases out 10 reach values of inter-petal resistances that are close to the experimental ones. This phenomenon is predominant especially for samples that are shorter than the maximum twisting pitch.

Chapter 4

Coupling loss modeling

4.1 Introduction

The energy dissipation in superconducting cables due to the presence of an external time-varying magnetic field may results in a loss of stability in the coils of a Tokamak reactor. The conductors are exposed to the pulsed mode operation of the Central Solenoid and the Poloidal Field coils, but also to transient situations like the ramp up and ramp down phases of the Toroidal Field coils during which the AC losses are concentrated. In a multi-stage conductor, the coupling currents loss constitutes a crucial term of the AC losses, which also include the hysteresis loss related to the magnetization produced by the screening currents, and the pure eddy currents loss induced in the copper stabilizer. In particular, the inter-strand loss are predominant compared to the inter-filament one since the current is forced to cross the resistance attributable to the contact between the strands involved, in addition to the resistive matrix of the strands. Moreover, the inter-strand coupling current loops are linked to a greater volume fraction of the cable then the ones induced between the superconducting filaments inside a single strand. At very low frequencies, i.e with full penetration of the applied field, the hysteresis loss is constant [27] whereas the coupling loss per volume of strands per cycle is proportional to the frequency f [Hz] and the square of the amplitude $\mathrm{B_a}$ [T] of the sinusoidal external field [60]:

$$\mathrm{Q_{cpl}} = \frac{\pi\,\mathrm{B_a^2}\,\omega\,\mathrm{n}\tau}{\mu_0}\ , \tag{4.1}$$

where n is the shape factor, defined as $n = 1/(1-D)$ with D demagnetization factor [61], and τ [s] is the decay time constant of the induced coupling currents. It can be shown that, for a round multifilamentary strand in a perpendicular

applied field the time constant is:

$$\tau = \frac{\mu_0}{2\rho_\perp}\left(\frac{t_\mathrm{p}}{2\pi}\right)^2 , \tag{4.2}$$

where t_p is the twist pitch and $\rho_\perp$ is the electrical resistivity in the transverse direction [62]. Unfortunately, this is not the case of a whole cable, where a large number of loops are present which give rise to a set of time constants. The most common method to calculate the coupling currents loss of magnets operating at low ramp rates is therefore to experimentally deduce the effective $n\tau$ [s] of the cable from the slope α of the linear part of the loss curve per cycle $Q_{cpl}(f)$ [60]:

$$n\tau = \alpha\frac{\mu_0}{2\pi^2 B_a^2} . \tag{4.3}$$

Broadly speaking, at low frequencies it is possible to identify the main $n_\mathrm{i}\tau_\mathrm{i}$ for each stage of cabling i, and by combining all of them, the characteristic one comes out as [63]:

$$n\tau = \sum_{\mathrm{i}=0}^{n_\mathrm{st}} n_\mathrm{i}\tau_\mathrm{i} \tag{4.4}$$

where n_st is the number of stages. However, this is valid under simplifying assumptions quite far from the real case. Several factors indeed influence the $n\tau$ value, such as the strands and cable layout, the twist pitches, the void fraction and the shape of the conductor. Nevertheless, it is a paramount feature to be investigated since it gives the possibility to predict the behavior of each conductor in the presence of an external variable magnetic field with a specific change rate [T/s]. Analytical models based on theoretical basics can hardly predict the mechanism of coupling loss affecting multi-stage conductors of composite strands. Few number of cabling stages can be done considering, up to 2 [64], whereas, for more accurate analysis, semi-analytical or numerical calculations based codes are needed [65] [66] [67][68].
In this chapter, the old version of the THELMA electromagnetic module implemented by the University of Bologna, referred to as *Bologna EM module*, for the computation of the current distribution among the cable strands is summarized [69], and the numerical analysis about the coupling loss performed with the WR WP2 prototype conductor for the DEMO TF coils in order to validate the new geometrical model for flat cables is presented.

4.2 Bologna EM Module description

The Bologna EM module is a 3D model based on a non-linear distributed parameter network approach. The model equations, reported in detail in [69],

are derived from the Magneto-Quasi-Static formulation of the Maxwell equations, supposing that no magnetizable materials are present. The problem unknowns are the currents and the voltages in all the cable elements (CEs). In this model, the currents are assumed uniformly distributed in the cross section of a given CE. The following equations are hence considered:

$$\mathbf{E} = -\nabla V - \frac{\partial \mathbf{A}}{\partial t}\,, \tag{4.5}$$

$$\nabla \cdot \mathbf{J} = 0\ . \tag{4.6}$$

If the difference of currents $i_{\mathrm{k}}(s,t)$ given as a function of time t by the deviation of current $I_{\mathrm{k}}(s,t)$ flowing in the k^{th} CE at the curvilinear coordinate s from an uniform current distribution among all the N_{st} strands is defined:

$$i_{\mathrm{k}}(s,t) = I_{\mathrm{k}}(s,t) - \frac{N_k}{N_{\mathrm{st}}} I(t)\,, \tag{4.7}$$

where N_{k} is the number of strands represented by the k^{th} CE and I(t) is the total transport current, these two sets of equations can be hold:

$$\begin{aligned}\frac{\partial V_k}{\partial s}(s,t) = -\mathbf{E}_k \cdot \frac{d\mathbf{y}_k}{ds} - m_{u,k}(s)\frac{dI}{dt}(t) - \sum_{\beta=1}^{N_{ext}} m_{e,k}^{\beta}(s)\frac{dI_e^{\beta}}{dt}(t) \\ - \sum_{\alpha=1}^{N_{ce}} \int_0^L m_k^{\alpha}\left(s,s'\right)\frac{\partial i^{\alpha}}{\partial t}\left(s',t\right) ds'\,,\end{aligned} \tag{4.8}$$

$$\frac{\partial i_k}{\partial s}(s,t) = -\sum_{i=1}^{N_{ce}} \sigma_{ki}(s)\left[V_k(s,t) - V_i(s,t) - h_{u,ki}(s)\frac{dI}{dt}(t) - \sum_{\lambda=1}^{N_{ext}} h_{e,ki}^{\lambda}(s)\frac{dI_e^{\lambda}}{dt}(t)\right]\,, \tag{4.9}$$

with $k = 1, \ldots, N_{\mathrm{ce}}$. Equations (4.8) represent the longitudinal variation of the voltage along the axis line of a CE, and it derives from four terms of the voltage drop:

1. electric field: $\mathbf{E}_k$ is evaluated from the current density through appropriate constitutive relations, depending on the local temperature, magnetic induction and applied strain. The other normal materials that compose the strands are supposed in parallel with the superconducting one;

2. voltages induced by time variations of the self field generated by the transport current I(t) flowing along the whole cable;

3. mutual inductive coupling of each CE with the β^{th} external coil eventually present;

4. mutual inductive coupling (relative to the current imbalance) between different cable elements.

Equations (4.9) derived from (4.6), represent the k^{th} CE current changes due to the distributed contacts with the other CEs, and it is expressed by the integral of the electric field along a line connecting two different CEs center. In particular, it accounts for:

1. the difference between the two voltages at the ends of the line;

2. the voltages induced by variation of the self magnetic field generated by the conductor, and the variation of the magnetic fields generated by the external coils.

The transversal per unit length conductance σ_{ki} [S/m] between the k^{th} and the i^{th} CEs is computed directly from the strands geometry by means of the contact model and the Udine EM module described in Section 3.2. As regards the per unit length self and mutual induction coefficients $h_{\mathrm{u,ki}}(s)$, $h^{\lambda}_{\mathrm{e,ki}}(s)$, $m_{\mathrm{u,k}}(s)$, $m^{\beta}_{\mathrm{e,k}}(s)$ and $m^{\alpha}_{\mathrm{k}}(s,s')$, a detailed derivation is given in [69]. Finally, with some suitable algebraic arrangements, the $2\mathrm{N_{ce}}$ number of equations and unknowns of the complete system made of equations (4.8) and (4.9) can be reduced to $\mathrm{N_{ce}}-1$, corresponding to the difference currents in all CEs but the last.
The Bologna EM module is used to compute the coupling currents loss in the following sections.

4.3 Preliminary study: coupling loss computation in the PITSAM1 conductor

Before starting to analyze the coupling loss with the two W&R and R&W DEMO TF prototype conductors, a preliminary study has been done with a relatively small superconducting cable with rectangular cross-section in order to assess the relation between the parameters of new geometrical model used to reproduce the strands geometry and the Bologna EM module. For this reason, the PITSAM1 conductor designed for the EFDA dipole magnet [9] has been taken into account as first test benchmark because of its simple layout in terms of number of strands and final dimensions compared to the WP1 and WP2 cables. Indeed, it is a flat cable-in-conduit conductor consisted of only 144 superconducting strands which are first twisted together by means of four

Table 4.1: PITSAM1 Main properties of the cable.

Parameter	Value
Num. Sc strands	144
Num. Cu strands	0
Cu/nonCu	1
SC strand diam. [mm]	0.81
Final cable layout	$3 \times 3 \times 4 \times 4$
Twist pitches [mm]	58/95/139/213
CICC inner dim. [mm]	17.9×6.3
Void fraction [%]	30

stages of cabling and then compacted down to the design void fraction of 30% (see Table 4.1).
The geometry of a one meter long sample has been modeled with the new THELMA geometrical model, and the AC loss due to the inter-strand coupling currents have been computed in order to compare the numerical results with the experimental ones measured by the Superconductivity Group of the Swiss Plasma Center at the *SULTAN* test facility in Villigen (CH) [70], as reported in [9]. For this preliminary analysis, the strand 2D contact resistivity is considered as a fitting parameter used to match the experimental AC losses curve, since no contact resistances measurements have been carried out for this conductor.

4.3.1 Model description

Two different discretizations have been considered for the modeling of the PITSAM1 cross-section. The first one is composed of 144 CEs corresponding to the whole detailed cable model, whereas a second simplified discretization made of 16 CEs equivalent macrostrands each corresponding to the 3×3 SC bundle has been also taken into account. The macrostrands geometry and contact resistances are computed on the basis of the represented strands starting from the detailed cable geometry, and the material is modeled as an homogeneous medium whose properties are calculated through a weighted mean of copper and superconductor fractions according to the Cu/nonCu ratio λ. 3D views of both the detailed and the simplified PITSAM1 geometrical models are reported in Figure 4.1 and 4.2 respectively. The final cross-section of the cable after the final compaction is shown in Figure 4.3. As regards the longitudinal discretization of the sample, each strand is divided into a number of 200 elements along its axis, resulting in 42 elements for maximum twist pitch.

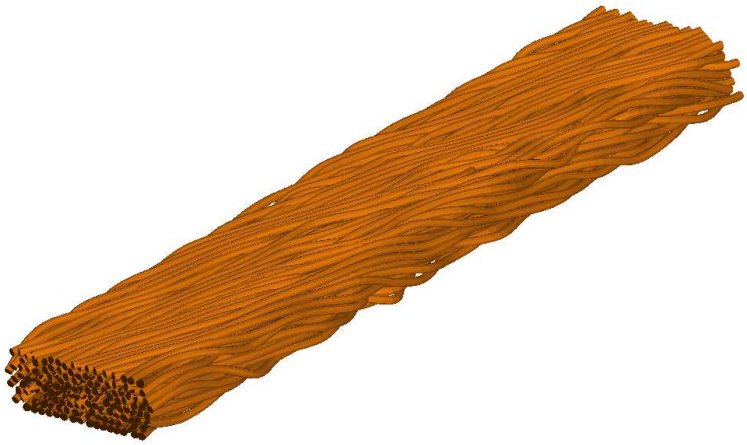

Figure 4.1: 3D view of the PITSAM1 complete geometrical model made of 144 superconducting strands.

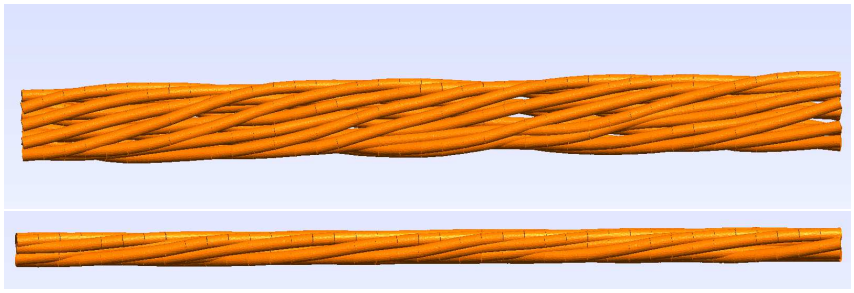

Figure 4.2: 3D view of the PITSAM1 simplified geometrical model made of 16 CEs [8].

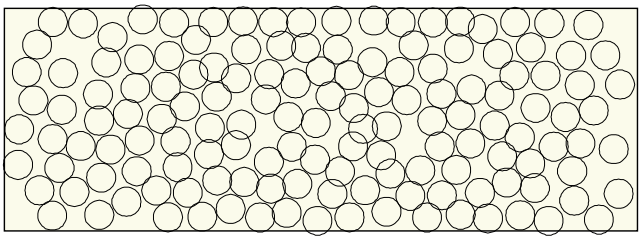

Figure 4.3: Final cable cross-section modeled with THELMA.

Table 4.2: Durham scaling law parameters for the PITSAM1 strands.

p	q	n	ν	w	u	ϵ_M
[-]	[-]	[-]	[-]	[-]	[-]	[%]
1.0404	2.919	2.500	1.500	2.200	0	0.0722
$A(0)$		$T_C^*(0)$	$B_{C2}^*(0,0)$	c_2	c_3	c_4
[A m^{-2} T^{3-n} K^{-2}]		[K]	[T]	[-]	[-]	[-]
$1.493{\cdot}10^8$		16.90	30.20	-0.6362	-0.4346	-0.0578

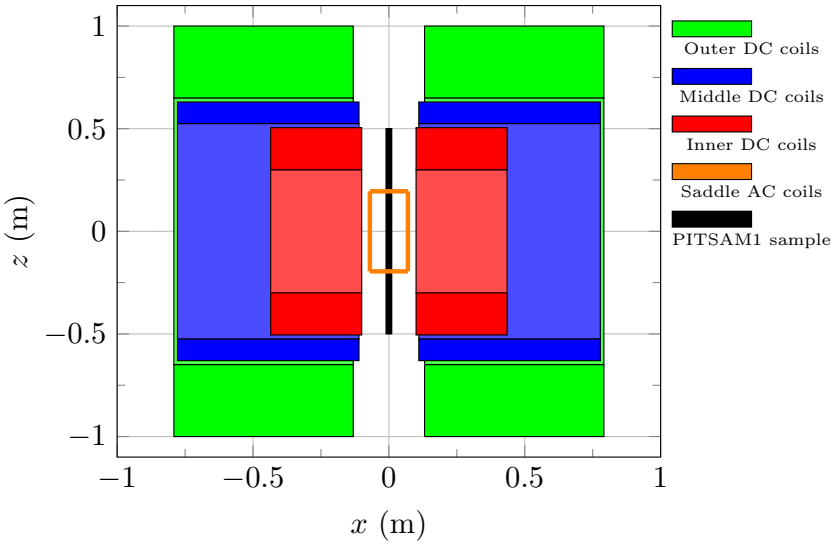

Figure 4.4: Sketch of the Sultan coils modeled with the THELMA code.

The strand/macrostrand critical current density is modeled with the Durham scaling law [3] by considering the fit parameters summarized in Table 4.2 [71].

To compare the computed and the experimental results, both the DC and AC coils of the SULTAN facility are modeled and the magnetic flux density generated by them is taken into account together with the self field of the cable under testing. An illustrative cross-section of SULTAN coils is drawn in Figure 4.4. The samples tested in SULTAN usually consist in two conductors, the so called *left* and *right legs*, with a bottom joint or a U-bend at one end [70]. For this case study, the only left leg conductor is modeled. To reproduce the testing conditions, a DC background field of 2 T and a sinusoidal AC field of amplitude 0.3 T with a direction perpendicular to the wide side of the rectangular cross-section is imposed, as shown in left side of Figure 4.5. Indeed, in a flat conductor, the coupling loss is strongly influenced by the orientation of the external field as well as the aspect ratio [72] since, unlike the

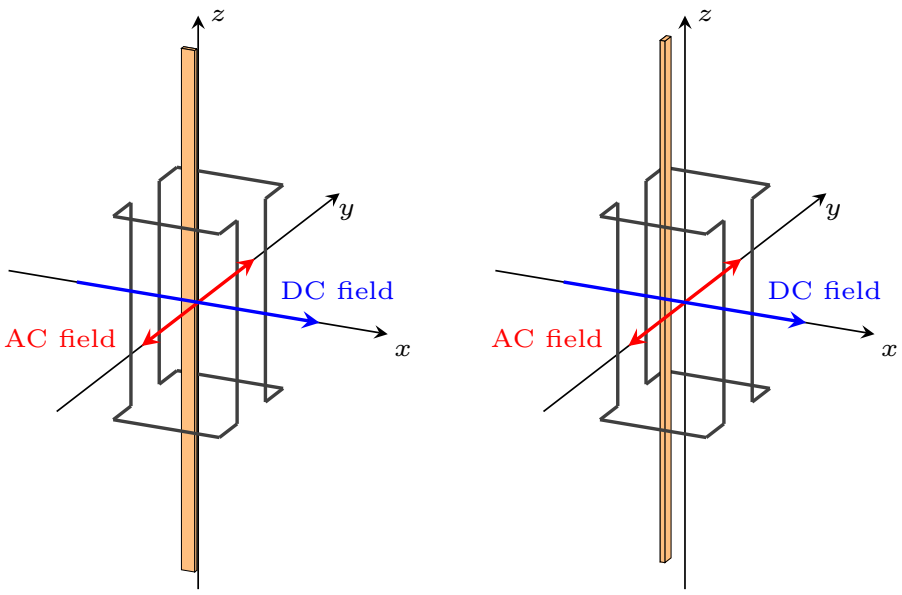

Figure 4.5: Detailed view of the Sultan saddle coils. Left: external AC field perpendicular to the wide side of the sample. Right: external AC field parallel to the wide side of the sample;

ITER circular CICCs, the cable surface exposed to the field changes with the field orientation. The experimental AC losses obtained with the virgin sample are considered as target for this first numerical analysis carried out with the THELMA code (see Figure 7 in [9]).

4.3.2 Numerical results

A first set of simulations has been run with the 16 CEs model for a faster calibration of the strand 2D resistivity parameter needed to compute the inter-strand contact resistances. Considering the frequency range of interest from 0.2 to 3 Hz, the best match between the experimental and the numerical results is obtained with $\varrho_c = 8.4{\cdot}10^{-13}$ Ωm^2, whereas the minimum contact width has been set equal to $0.2D_0$, as for the DEMO TF prototypes case. Finally, the same value of ϱ_c [Ωm^2] has been adopted to compute the coupling loss with the complete 144 CEs model. Since the measured data refer to the total AC losses, an offset of 70 kJ/m^3 is added to the numerical results to take into account the contribution of the hysteresis loss that is not modeled in the old version of the Bologna EM module. This value was determined by the linear extrapolation of the measured total AC losses towards zero frequency [9].

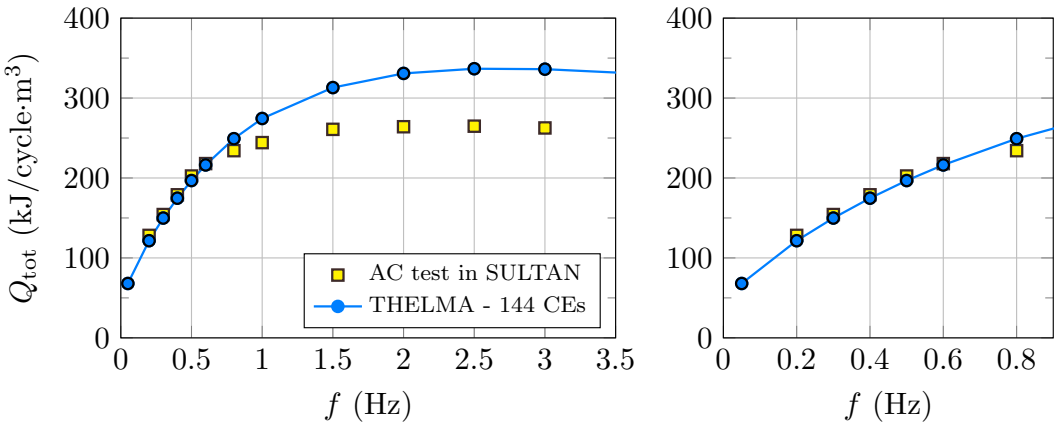

Figure 4.6: AC losses density per cycle versus frequency of the PITSAM1 conductor: comparison between the experimental data [9] and the THELMA numerical results.

The computed losses are first normalized per volume of conductor assumed as the SULTAN bore *high field zone* length (∼380 mm) multiplied by strands number and cross-section, and then plotted together with the measured ones in Figure 4.6. The agreement is very good in the low frequency range, i.e. where the coupling loss time constant $n\tau$ [s] is derived by means of equations (4.3). In particular, the numerical results give $n\tau = 103$ s, whereas $n\tau = 100$ s was found with the AC losses test [9]. At high frequencies, where the coupling loss linearity vanishes, the THELMA code gives losses which are ∼25% higher than the experimental ones. Generally, the AC losses behavior at high frequencies is of difficult understanding because of the screening effect [73]. From the physical point of view, the addition of the hysteresis loss as a fixed value to the numerical results is correct only in the low frequency range. In fact, at higher frequencies, both the inner superconducting filaments and the strands located inside the cable tend to be shielded because of the screening current effect that leads to a reduction of the magnetization and hence of the hysteresis loss [29][27][60]. On the other hand, the discrepancy is too large to be attributable to the demagnetization of the superconducting filaments so, further investigation has been made. Three more samples have been modeled with three different initial strands phases generated as a random array $\boldsymbol{\Theta}$. For each sample, two longitudinal discretizations are considered for the modeling of the strands geometry, referred to as N_{em}^{200} and N_{em}^{400}, composed by a number of 200 and 400 elements respectively. For all these samples, the same value of strand 2D resistivity is used to compute the inter-strand contact resistances, i.e. $\varrho_c = 8.4{\cdot}10^{-13}$ Ωm^2, and, to save computational time, the 16 CEs simpli-

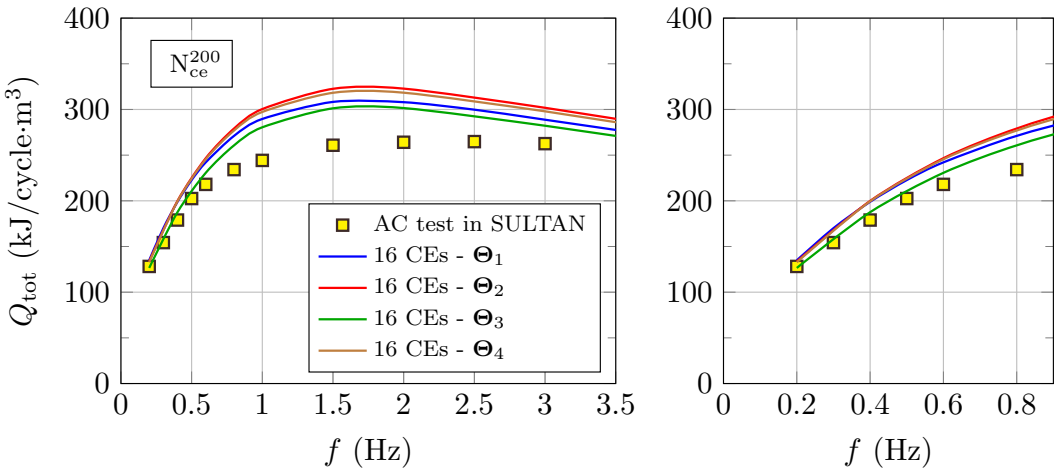

Figure 4.7: PITSAM1 total losses density per cycle: comparison between the experimental data [9] and the THELMA numerical results obtained with the 16CEs simplified model and the N_{em}^{200} discretization. Four different phase sets are considered.

fied cable model is adopted to calculate the coupling currents loss. As above, the hysteresis loss contribution is added. The numerical results of the N_{em}^{200} and N_{em}^{400} discretizations are plotted in Figure 4.7 and 4.8 respectively. As it can be noticed, in both cases, the results obtained at magnetic field frequencies lower than 1 Hz are in good agreement with the measured values whatever the phase array. On the other side, at higher frequencies, the N_{em}^{400} discretization gives coupling losses that are lower than the N_{em}^{200} one, even if the effect of the initial positions is more pronounced.
This preliminary analysis is encouraging since in the low frequency range, where no screening effect occurs and the cable time constant $n\tau$ can be extrapolated, the results of the coupling loss simulations are quite stable for any case study. Differently, at higher frequencies, a denser longitudinal discretization of the strands is recommended to improve the matching of the experimental data. Finally, the detailed 144CEs geometrical model gives better results than the 16CEs simplified one at low frequencies, if the same value of 2D contact resistivity in considered.

To investigate the $n\tau$ dependence on the external field orientation, the currents coupling loss has been also computed with an AC field parallel to the wide side of sample. Since there are no other experimental data about AC losses measurements with the PITSAM1 sample, some qualitative results are just given and discussed. To simulate this test scenario, one 16CEs PITSAM1 sample ($\boldsymbol{\Theta} = \boldsymbol{\Theta}_1$) has been rotated around its axis by 90° inside the SULTAN

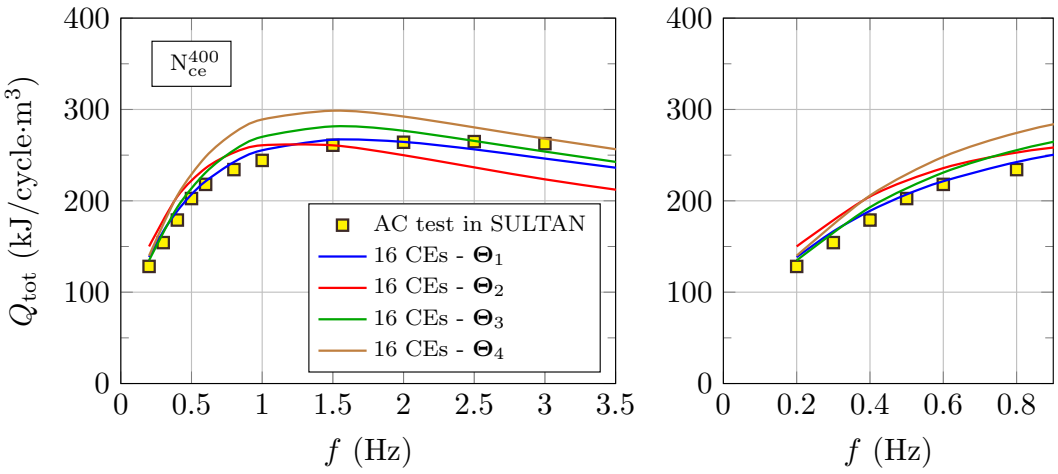

Figure 4.8: PITSAM1 total losses density per cycle: comparison between the experimental data [9] and the THELMA numerical results obtained with the 16CEs simplified model and the N_{em}^{400} discretization. Four different phase sets are considered.

bore modeled with THELMA, in order to switch from a perpendicular to a parallel configuration of the AC applied field, as shown in the right side of Figure 4.5. The strand 2D resistivity value is the same as in the previous case for both the field configurations. The frequency range considered is from 0.2 to 1 Hz. The numerical results obtained with THELMA are shown in Figure 4.9. The dependence of the AC loss with the orientation of the external field was analyzed in [61] and the following relation was proposed for a rectangular conductor whose filaments are homogeneously distributed on its cross-section:

$$\frac{(n\tau)_{90}}{(n\tau)_0} \approx \frac{a^4}{4b^4} \,, \tag{4.10}$$

where a is the wide side of the conductor and b the short one. Starting from the $(n\tau)_{90}$ and $(n\tau)_0$ values calculate from the loss curves reported in Figure 4.9 referred to the perpendicular and the parallel field orientations with (4.3), the loss anisotropy of the PITSAM1 sample is estimated as:

$$\frac{(n\tau)_{90}}{(n\tau)_0} = 11.82 \,,$$

which is smaller than the one expected with (4.10):

$$\frac{a^4}{4b^4} = 16.29 \,,$$

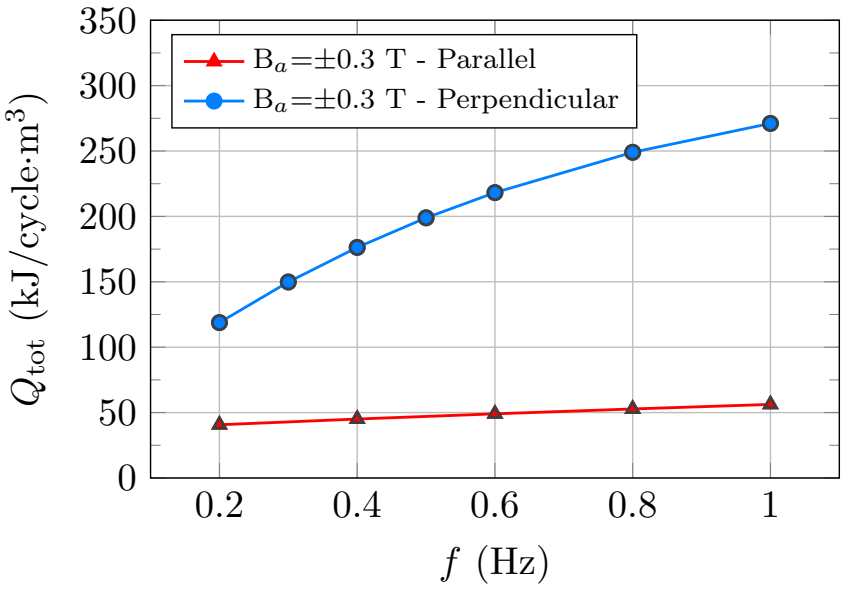

Figure 4.9: PITSAM1 total losses density per cycle: comparison between the THELMA numerical results obtained with two sinusoidal field orientations, parallel and perpendicular to the cable. The 16CEs simplified model, the $\mathrm{N}_{\mathrm{em}}^{200}$ discretization and one phase set are considered.

where $a = 17.9$ mm and $b = 6.3$ mm are the inner dimensions of the conductor. The discrepancy between the two ratios confirms that the anisotropy of a flat twisted multi-strand conductor, even if present, is not as large as for a rectangular monolith with a single time constant [74][75]. In fact, in case of CICCs, the Campbell's formula (4.10) is not strictly valid since the layout of a multi-stage conductor involves different twist pitches, the presence of contact resistances between the strands and a void fraction in the cable cross-section.

4.4 Coupling loss analysis in the WR WP2 DEMO TF prototype conductor

To validate the new geometrical model developed for flat multi-stage cables, the coupling currents loss are computed for the WR WP2 prototype conductor proposed for the DEMO TF coils. Differently from the analysis presented in Section 4.3, the strand 2D resistivity parameter has been already fixed on the basis of the inter-strand contact resistances measurements, as shown in Section 3.3. For this reason, the subsequent study has a deep impact on the geometrical model validation. The coupling loss modeling with the RW1 WP1 conductor is still ongoing.

4.4.1 AC losses measurements in the WP2 conductor

The total AC losses were measured by the University of Twente in the dipole setup [42] with the same 400 mm long WR WP2 sample already prepared and used for the contact resistances measurements [6]. In the dipole setup, the conductor can be subjected to both DC and AC magnetic field by the superimposition of a constant term and a term sinusoidal with time. The homogeneous field length is about 50 cm. The AC losses are measured via calorimetry by means of a calorimeter installed inside the bore of the magnet, or via magnetization method by means of a set of compensated pick-up coils wound around the conductor. In this case, two field orientations were considered because of the conductor rectangular shape. The following AC test conditions are chosen for the validation of the new geometrical model:

- WP2: virgin sample tested at 4.2 K in liquid He bath and a sinusoidal field of ± 0.15 T without an offset field. The experimental data are reported in Figure 1 of [6].

Broadly speaking, the virgin WP2 conductor has shown same level of hysteresis loss but higher coupling loss compared to the ITER Nb_3Sn cables [76],

Table 4.3: Fit parameters of the ITER scaling law for the WR WP2 strands critical current density.

p	q	C	B_{c20m}	T_{c0m}
[-]	[-]	[AT/mm^2]	[T]	[K]
0.593	2.16	34547	33.24	16.34
C_{a1}	C_{a2}	ϵ_m	$\epsilon_{0,a}$	ϵ_{appl}
[-]	[-]	[%]	[%]	[%]
50.06	0	-0.059	0.312	-0.21

resulting in a relatively high values of time constant. This result is probably attributable to the low void fraction of the conductors and the absence of the petals wraps.

4.4.2 Coupling loss numerical analysis: DEMO - WR WP2

Model description

Since the WR WP2 conductor is composed of a huge number of strands, it has been modeled with 43 equivalent macrostrands, each corresponding either to the 3×3×4 SC bundle or the 3×4 Cu core bundle, in order to make the computational time reasonable. As for the PITSAM1 conductor, the macrostrands geometry and contact resistances are computed on the basis of the detailed cable geometry made up of 1236 strands modeled with the new geometrical model. In this case, the five samples geometries with different phase set generated for the contact resistances analysis are used. The two cooling spirals inserted in two petals are modeled as two more 3×4 core bundles made of strands with high longitudinal and inter-strand contact resistivity. For the other 1080 superconducting and 136 copper strands, the set value of 2D contact resistivity $\varrho_c = 8.5{\cdot}10^{-13}$ Ωm^2 (see Section 3.3.1) is adopted for the inter-strand resistances computation. The macrostrand critical current density is modeled with the official *ITER scaling law* [24] adopted for Nb_3Sn critical surface which has been proposed by the University of Twente as a more accurate description of the Summers' fit [77]. In Table 4.3 are reported the strand fit parameters used for this analysis [7]. The cross-section and the 3D view of the simplified cable geometry composed of 43 equivalent macrostrands are respectively shown in Figure 4.10 and 4.11.

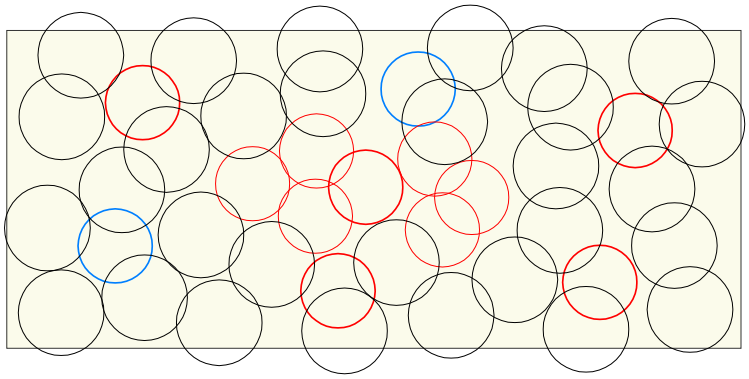

Figure 4.10: Cross-section of the simplified W&R WP2 cable model made of 43 CEs; two of the bundle cores (blue macrostrands) represent the cooling channels.

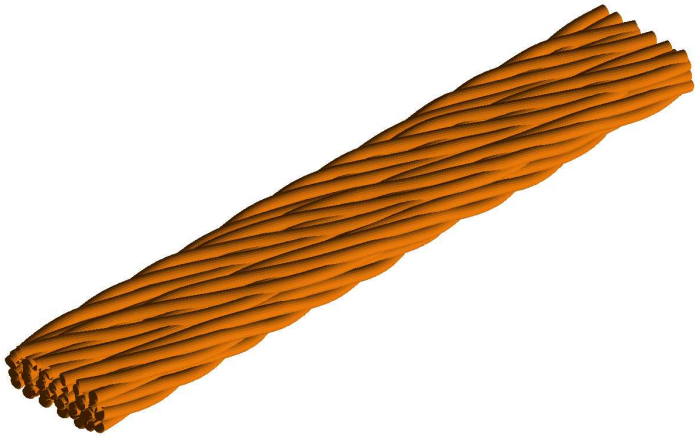

Figure 4.11: 3D view of the W&R WP2 simplified geometrical model made of 43 CEs.

Numerical results

The coupling current loss computed with the THELMA code are plotted in Figure 4.12 together with the measured one. The overall trend of the experimental AC losses versus frequency is respected by all the samples modeled with THELMA. At frequencies below 8 mHz, where the linear behavior of the measured coupling loss deviates [6], the agreement between the experimental and the numerical results is good whatever the phase set $\mathbf{\Theta}$. The coupling time constant of the conductors found numerically, $n\tau_c \approx 41.80$ s, is close to the one derived from the AC test, $n\tau_m = 37.9$ s, and also the position of the calculated loss peaks appear to be in accordance with the experimentally one. At frequencies above 10 mHz, the coupling loss given by the THELMA simulations are quite higher in comparison with the AC test results, but a not negligible dependence on the strands initial positions can be noticed. This was expected since the maximum twist pitch of the conductor is ∼1.7 times the length of the tested sample, so the field screening may be strongly influenced by the coupling currents paths and hence by the strands initial positions. As regards the hysteresis loss, it has not been considered since it is negligible in comparison with the total AC losses, and then it was extrapolated at very low frequencies where the experimental data were few and less accurate [6].
The five samples of the WR WP2 have been modeled with 80 longitudinal elements because it represented a reasonable compromise between the accuracy of the coupling loss simulations and the computational cost related to the modeling of the demanding cable geometry. However, the increase of longitudinal points number may results in lower coupling loss for frequencies higher then 8 mHz, as seen with the PITSAM1 case study.

Parametric analysis

In order to investigate the 2D model sensitivity to the strand contact resistivity parameter ϱ_c, which is used to compute the contact conductances for the Bologna EM module (see Section 4.2), parametric studies have been carried out. As reasonably expected, as the contact resistances between strands increase, coupling loss tends to decrease and the frequency f_M [Hz] corresponding to the maximum AC losses value tends to increase, with a consequent reduction of the coupling time constant [60]. For this reason, the contact conductances and the coupling loss have been also computed with the 2D strand contact resistivity increased by 10% and 20% with respect to the reference value (ϱ_c=8.5·10^{-13} Ωm^2). It follows:

- $\varrho_{c,10\%}$=9.35·10^{-13} Ωm^2 ;

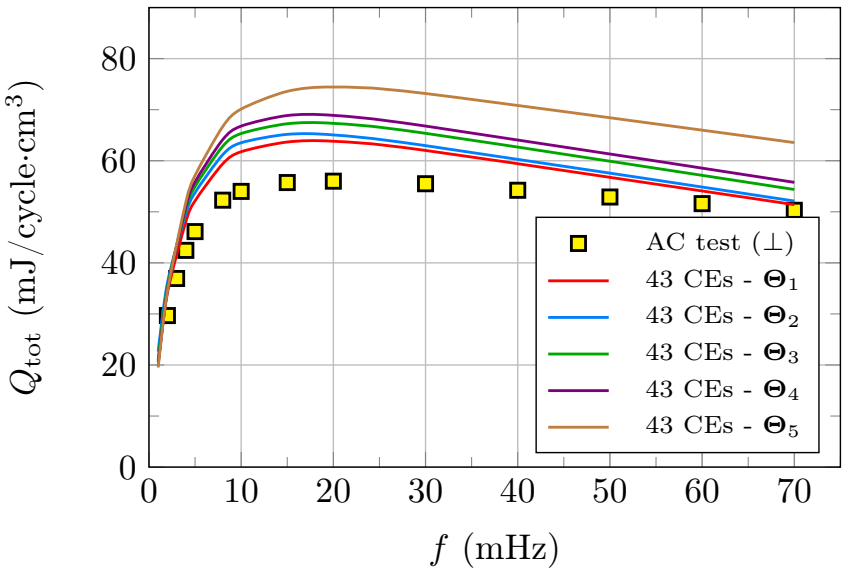

Figure 4.12: AC losses density per cycle versus frequency of DEMO WR WP2: comparison between the experimental data [6] and the THELMA numerical results obtained with the 43CEs simplified model. Five different phase sets are considered.

- $\varrho_{\mathrm{c},20\%}$=1.02·10^{-12} Ωm^2 .

In Figure 4.13, the numerical results obtained with the five samples of the WR WP2 modeled with THELMA are shown. The numbers of equivalent macrostrands and longitudinal elements and the minimum width parameter w_0 have not been changed for this analysis (see Section 4.4.2). From the numerical data in Figure 4.13, a slight reduction of the effective $n\tau$ can be observed. This reduction is about 0.5% in the case of $\varrho_{\mathrm{c},10\%}$ and 1.3% in the case of $\varrho_{\mathrm{c},20\%}$, compared to the reference case. Actually, no reduction of the maximum loss is visible, whereas an increase of f_M occurs.

The effect of the ϱ_{c} variation on the contact resistances distribution is now shown. As described in Section 3.3.1, the analysis with the five WR WP2 samples has been performed again assuming $\varrho_{\mathrm{c},10\%}$ and $\varrho_{\mathrm{c},20\%}$. Figure 4.14 shows that the computed resistances per unit length increased proportionally to the ϱ_{c} value for all 10 strands combinations (see Table 3.2).

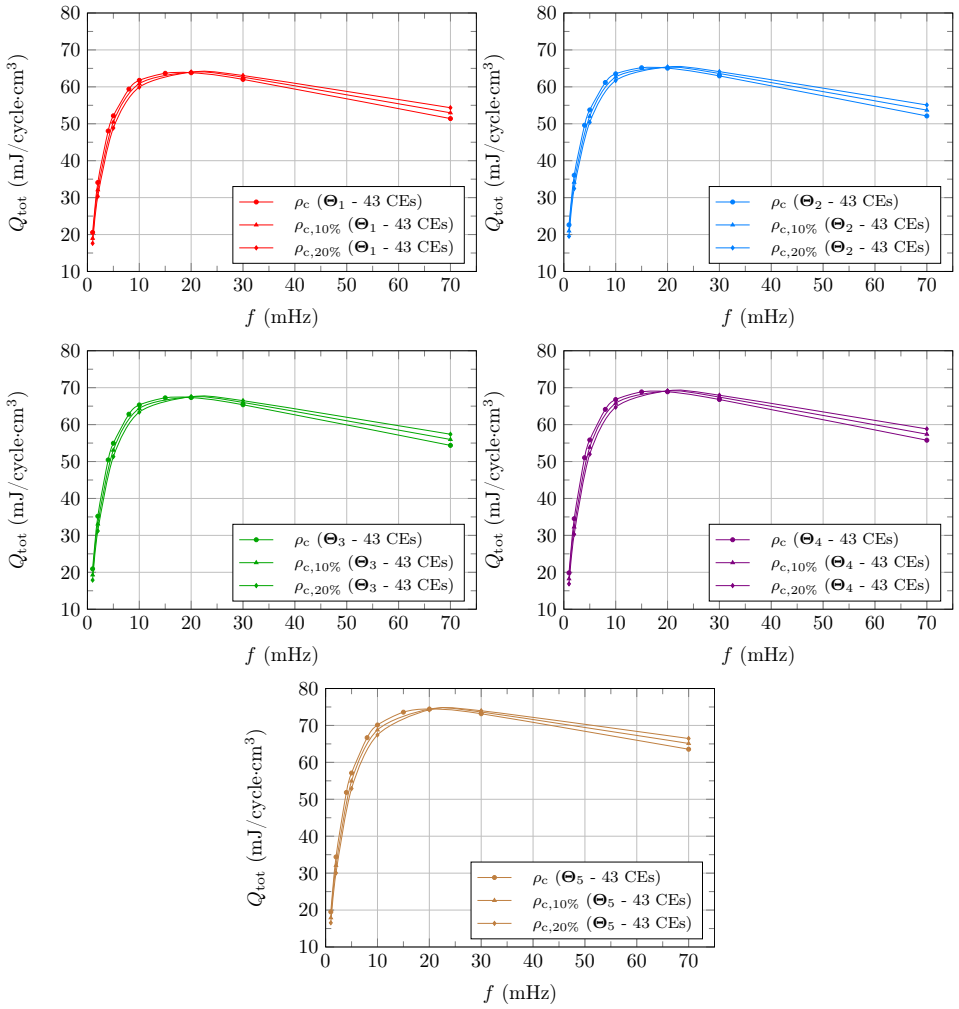

Figure 4.13: Results of parametric analysis: coupling loss density per cycle versus frequency computed assuming three different values of the contact resistivity parameter used to calculate the contact conductances between the cable strands. In each chart, one phase set $\boldsymbol{\Theta}$ used to model the geometry of the sample is considered.

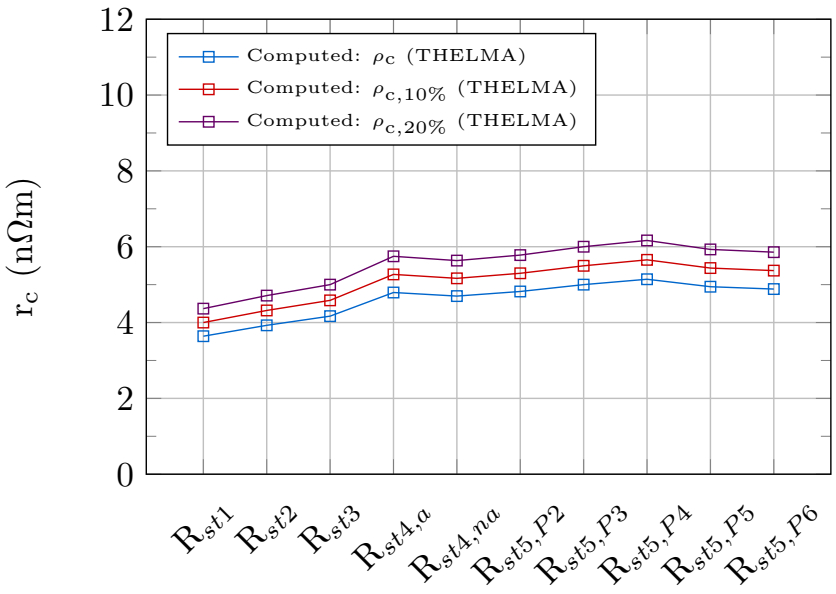

Figure 4.14: Results of parametric analysis: contact resistances distribution assuming three different values of the contact resistivity parameter.

Chapter 5

Eddy currents loss prediction

5.1 Introduction

One of the main solutions proposed for the conductor of the DEMO toroidal field (TF) magnets is based on the Nb_3Sn react&wind (RW) technology. Since with this technology the jacketing process is made after the heat treatment, the compressive thermal strain on the Nb_3Sn strands is reduced resulting an increase of the critical current density and hence to a significant reduction of the required amount of Nb_3Sn compared to the wind&react (WR) technology [78]. In addition, there is more freedom regarding the shape of the jacket as it can be composed by two longitudinally shells welded together after the heat treatment. This allows to get jackets with different thickness in the winding radial and the toroidal directions and hence to optimize the amount of steel according to the mechanical loads in the layers of the TF coils [79]. The RW option is therefore a promising choice from both the cost and the reliability points of view, taking into account the final size of the TF WP and the stability of the strands under cyclic loading and thermal cycles.
The RW method leads to a flat cable design in order to arrange the strands as close as possible to the neutral bending axis [80] and hence to minimize the bending strain on the heat-treated strands during the conductor manufacturing and the coil winding. For this reason, in the proposed prototypes of cables, the copper stabilizer is not homogeneously distributed inside the cable, as it is in the ITER TF cable-in-conduit conductors made by superconducting and copper strands twisted together, but it is segregated and it forms an outer layer around the central conductor. In the case of segregated copper, it is mandatory to investigate on the contribution of the eddy currents to the total losses due to an external variable magnetic field, e.g. during the charge and discharge operations of the coils and the plasma fast transients.

In the following sections, the prototype cable based on the RW technology designed and tested by the superconductivity group of the EPFL - Swiss Plasma Center (SPC) for the DEMO TF coils is presented. The contact resistances measurements and the modeling of the eddy currents loss in the new copper stabilizer proposed for the so called RW2 conductor are also shown and discussed.

5.2 SPC React&Wind cables

Two prototype RW TF conductors have been proposed, manufactured and tested in the past by the SPC. The first one, RW1 [41], was designed for 82.4 kA in 13.5 T field, corresponding to the DEMO 2013 reference design [81]. This is the cable that was modeled and analyze in Chapter 3. The second prototype, RW2 [78][82], was optimized for 63.3 kA and 12.2 T of the DEMO 2017 baseline [83]. Both the conductors have a similar layout: they are flat cables made of a central core with a small thickness, 12.3 mm and 11.0 mm for the RW1 and RW2 respectively, to have a low strain during the bending process of the coil winding. The core is composed by twisted Nb_3Sn strands and it is surrounded by the stabilizer. For the RW1 a layer of thick chromium-coated copper wires was considered, while, for the RW2, two solutions based on a solid block of Cu/CuNi "mixed matrix", e.g. the half-size (HP) and the full-size (FP) profile, were preferred as stabilizers (Figure 5.1).

The AC measurements carried out with the RW2 prototype in the SULTAN facility [70], by applying an external sinusoidal field, showed acceptable coupling loss in the conductor [82], but large eddy currents loss in the stabilizer leading to an unwished amount of total AC losses in the cable [84]. A large contribution due to the eddy currents was already expected, since the RRR values measured in the longitudinal and the transverse directions were low in the half-size profile and much higher in the full-profile stabilizer, leading to a low ratio of longitudinal to transverse RRR for both the solutions, as shown in Table 5.1 [78]. Indeed, a stabilizer with high transverse resistance and a good conductivity along the cable is desired to minimize the AC losses and to guarantee a safe behavior in case of quench.

To reduce the eddy currents loss, a Rutherford cable made by CuNi-clad copper strands has been proposed as new stabilizer for the RW2 conductor instead of the solid mixed matrix profiles. The high longitudinal RRR of the copper (400-450), the CuNi cladding of the strands to increase the transverse resistance and the undemanding manufacturing process are the main features of this promising solution.

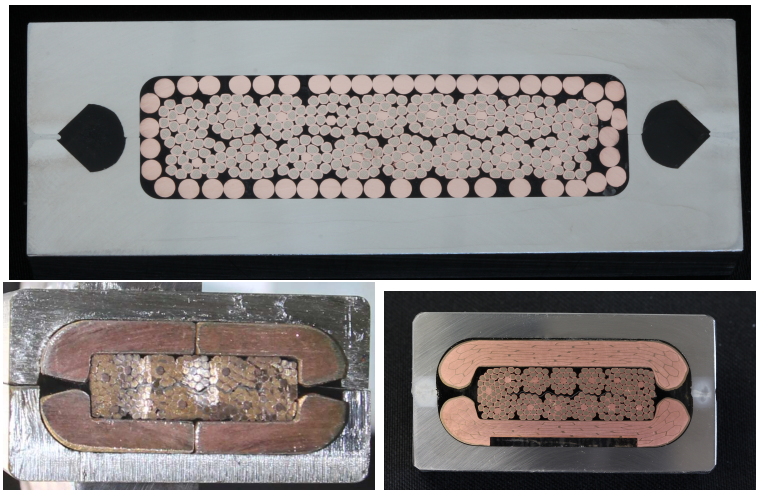

Figure 5.1: Upper: RW1 with chromium-coated copper strands around the central conductor. Below: RW2 with half-profile (left) and full-profile (right) Cu/CuNi mixed matrix stabilizer (courtesy of P. Bruzzone).

Table 5.1: Longitudinal and transversal RRRs of the RW2 stabilizers.

Stabilizer	RRR_l	RRR_t	RRR_l/RRR_t
Half-profile	45	19	2.4
Full-profile	400 - 450	140	3.2

Table 5.2: Main characteristic data of the new RW2 Rutherford stabilizer.

Parameter	
Strands material	Copper
RRR	400 - 450
Strands cladding	Cu-Ni
Strands diameter [mm]	3.3
Number of strands	30
Void fraction [%]	10
Transposition pitch [mm]	450

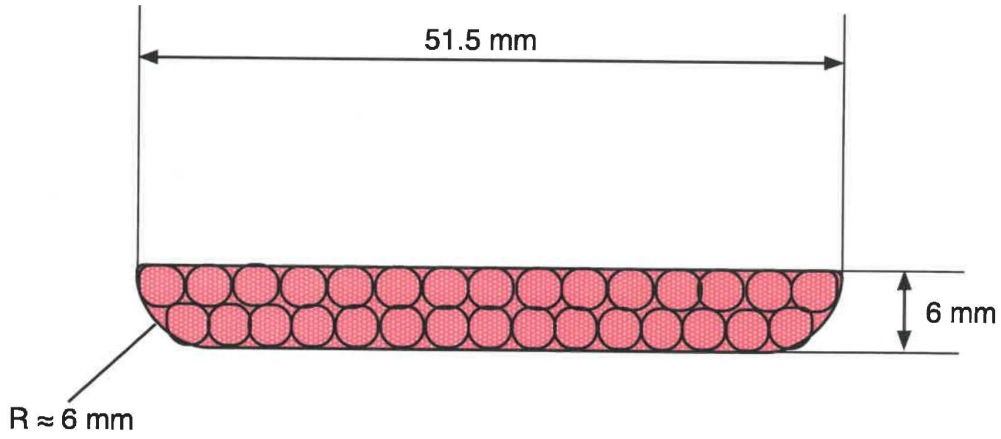

Figure 5.2: Cross-section of the Rutherford copper cable (courtesy of P. Bruzzone).

5.2.1 Rutherford cable

The specifications for the manufacturing process of the cable are summarized in Table 5.2 and the sizes of the cross-section are indicated in Figure 5.2.

5.3 Contact resistances analysis in the Rutherford copper cable

The electromagnetic part of the THELMA code presented in Section 4.2 that describes the cable through a distributed parameter electrical circuit model [69] has been used for the calculation of the losses inside the Rutherford cable due to an external AC field. All the strands are discretized into a

set of longitudinal elements, that are magnetically coupled to each other and are in electrical contact through contact conductances, computed thanks to the interstrand 2D model (see Section 3.2.2). As regards the following analysis, starting from the measurements of contact resistances between two copper strands made by the SPC group at the Paul Scherrer Institute, the 2D contact resistivity ϱ_c [Ωm^2] of the strands is tuned in order to model the Rutherford cable and carried out a preliminary analysis of the eddy current loss inside the new stabilizer.

5.3.1 Contact resistances measurement

One of the main aspects that rules the AC loss phenomenon in a superconducting cable is the distribution of the interstrand contact resistances, which strongly influences the induced current loops and hence the energy dissipation inside the conductor [42][43][44]. If a contact between copper strands is considered, as in the case of the stabilizer, the longitudinal resistance must also be considered since it is no longer negligible.
The resistance between two copper strands has been measured as function of the applied mechanical transverse load in order to achieve a parameter database of the Rutherford cable behavior when an external AC field is applied.

Measurement layout

Two chromium-coated copper strands were selected and inserted in an insulated steel track closed by a plate which is used to apply the load and press the strands. The current was injected and extracted at the opposite ends of the strands and the total resistance, accounting for the longitudinal and the contact one, was calculated from the voltage value measured between the two soldered voltage taps (see Figure 5.3). The sketches of the measurement layout are in Figure 5.4 and 5.5. The resistance was measured at different levels of applied load.

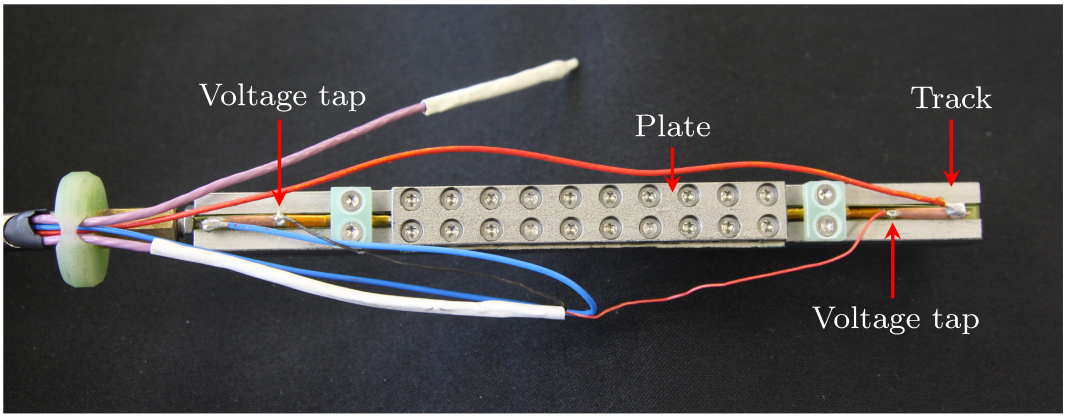

Figure 5.3: Layout of the contact resistance measurements carried out at PSI.

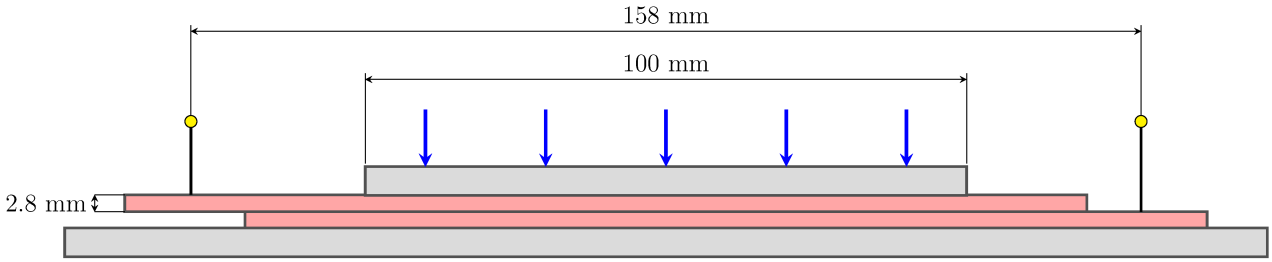

Figure 5.4: Sample longitudinal cross-section.

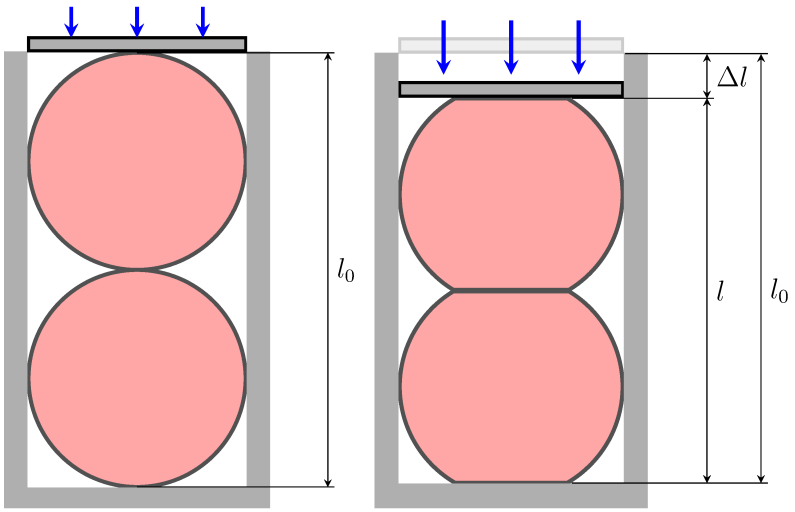

Figure 5.5: Sample transverse cross-section.

Table 5.3: Specifications of the contact resistances measurement.

Data	
Strands material	Copper
RRR	250 - 300
Strands diameter (D) [mm]	2.8
Strands coating	Cr
Number of sample pairs	4
Number of compressive levels	6

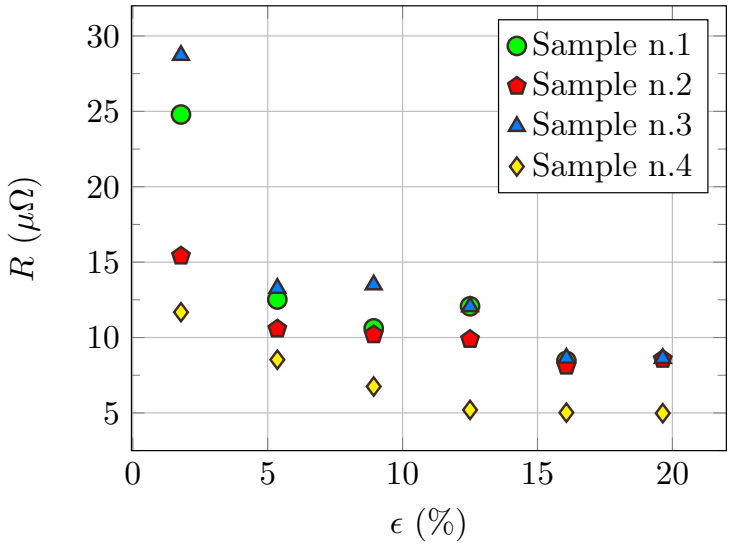

Figure 5.6: Experimental results of the contact resistances measurement performed at PSI.

Measurement results

In Figure 5.6 the values of the resistances measured between the two voltage taps are plotted versus the transverse percentage strain $\epsilon = \Delta l/2D$. Although the obtained results have a slightly scattered distribution for any load level, the overall trend seems to be reasonable. In addition, at high levels of compression, three samples out of four show quite close value of resistance.

5.3.2 The current diffusion in resistive inter-strand contacts

The contact resistance measurement described above can be used to tune the parameter of the interstrand 2D contact model, i.e. the 2D contact resistivity ϱ_c [Ωm^2] to be used for the stabilizer analysis.
Considering two parallel resistive strands, the contact length can affect the measurement because of the non negligible longitudinal resistance of the material. In this case, not only the contact resistance is involved and the two strands may be not considered as equipotential so that the current diffusion process along the strands may not be linear. For this reason, a simple model of current diffusion between two resistive (NM) strands is here presented and analyzed with the 2D contact model.

Distributed parameter network model

The geometry considered is represented in Figure 5.7: two strands are in contact and both are characterized by their contact 2D resistivity ϱ_{c} [Ωm^2]. Let x be the curvilinear coordinate along the couple of strands and let ϱ_{NM} and A_{NM} be respectively the strand resistivity [Ωm] and the cross section area [m^2]. The following current and balance equations can be written:

$$\begin{cases} \dfrac{du}{dx} = -r_{NM} i(x) - r_{NM}(i_{tr} - i(x)) = -r_{NM} i_{tr}\,, \\ \dfrac{di}{dx} = g_c w u(x)\,, \end{cases} \tag{5.1}$$

where $u(x)$ is the voltage between the two strands [V], $r_{\mathrm{NM}} = \varrho_{\mathrm{NM}}/A_{\mathrm{NM}}$ is the longitudinal resistance per unit length [Ω/m], i_{tr} is the transport current [A], $i_{tr} - i(x)$ is the current in the upper strand [A], $i(x)$ is the current in the lower strand [A], $g_c = 1/(\varrho_c + \varrho_c)$ is the transverse conductance per unit surface [S/m^2] and w is the width of the contact [m] (see Figure 3.3) which is constant in this model. Combining these two equations, one finds:

$$\frac{d^2 i}{dx^2} = -r_{NM} g_c w\, i_{tr}\,, \tag{5.2}$$

whose solution can be written as:

$$i(x) = -\frac{i_{tr}}{2\lambda^2} x^2 + I_1 x + I_2\,, \tag{5.3}$$

where I_1 and I_2 are two indetermination constants and $\lambda = \dfrac{1}{\sqrt{g_c w r_{NM}}}$ [m] is the *diffusion length*.

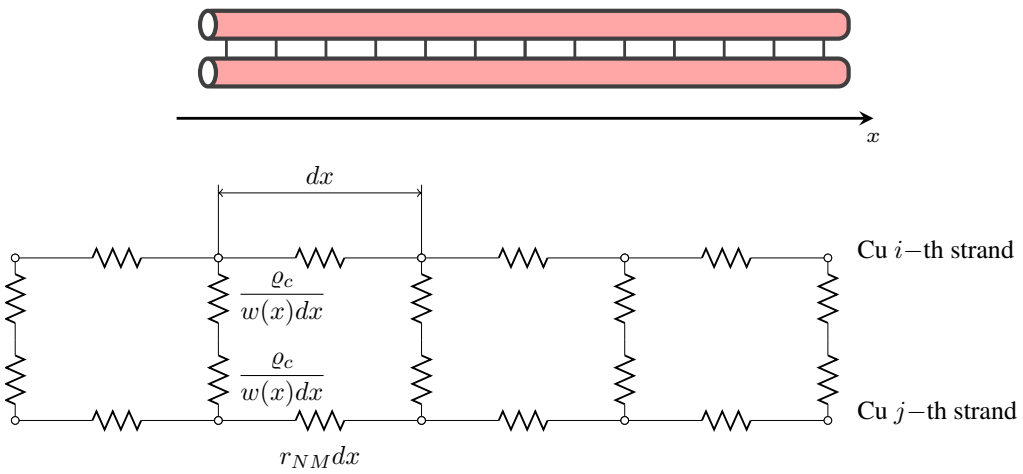

Figure 5.7: Above: view of two resistive (NM) strands in contact. Below: sketch of the equivalent distributed network, where an infinitesimal part, dx long, is put into evidence.

The distributed parameters model is completed with a current generator connected to the two strands ends (see Figure 5.8), and the resistance R [Ω] is computed as follow:

$$R = \frac{u_{AB}}{i_{tr}} \,. \tag{5.4}$$

The current in the lower strand $i(x)$ is obtained imposing the following boundary conditions to (5.3):

$$\begin{cases} i(0) = 0 \,, \\ i(l) = i_{tr} \,, \end{cases} \tag{5.5}$$

which lead to:

$$\begin{cases} I_1 = \dfrac{i_{tr}}{l}\left(1 + \dfrac{l^2}{2\lambda^2}\right) = \dfrac{i_{tr}}{l}\left(1 + \dfrac{\xi^2}{2}\right) \,, \\ I_2 = 0 \,. \end{cases} \tag{5.6}$$

where $\xi = l/\lambda$ is the ratio between the contact and the diffusion lengths. The value of u_{AB} is therefore calculated from:

$$\begin{cases} u_{AB} = u_{AC} + u_{CB} \,, \\ i(x) = i_{tr}\left(-\dfrac{x^2}{2\lambda^2} + \left(1 + \dfrac{l^2}{2\lambda^2}\right)\dfrac{x}{l}\right) = i_{tr}\dfrac{x}{l}\left(-\dfrac{\xi^2}{2}\dfrac{x}{l} + \left(1 + \dfrac{\xi^2}{2}\right)\right) \,. \end{cases} \tag{5.7}$$

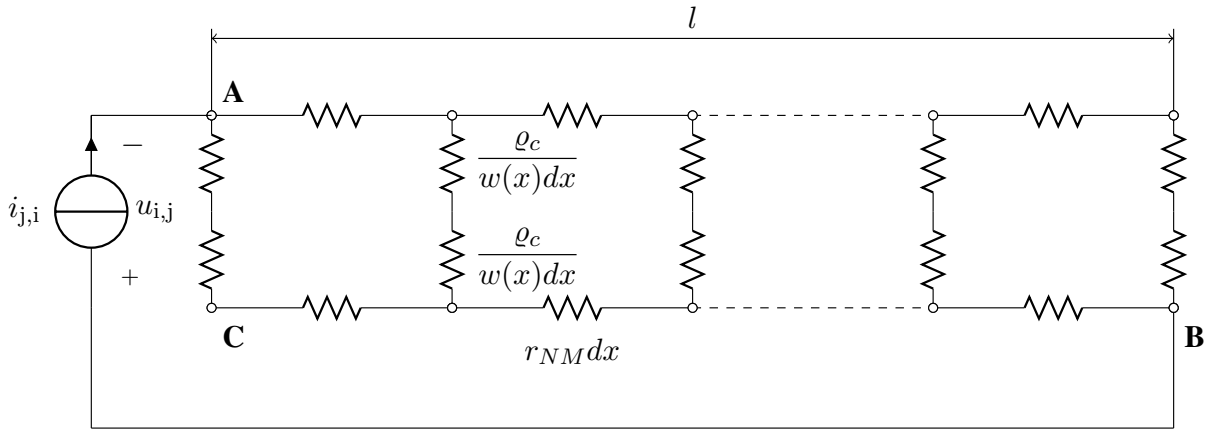

Figure 5.8: Model of the inter-strand resistance measurement.

It follows that:

$$\begin{aligned} u_{AC} &= \frac{1}{g_c w}\frac{di}{dx}\bigg|_{x=0} = \lambda^2 r_{NM}\frac{i_{tr}}{l}\left(1+\frac{\xi^2}{2}\right), \\ u_{CB} &= \int_0^l i(x) r_{NM}\, dx = \frac{r_{NM} i_{tr} l}{2}\left(\frac{\xi^2}{6}+1\right), \end{aligned} \tag{5.8}$$

hence

$$u_{AB} = i_{tr}\ l\ r_{NM}\left(\frac{\xi^2}{12}+1+\frac{1}{\xi^2}\right). \tag{5.9}$$

Given the contact width w, the transport current i_{tr}, the longitudinal resistance per unit length r_{NM} and the contact length l, it is possible to set the 2D model parameter, i.e. the strands contact resistivity ϱ_c, in order to obtain the proper value of resistance R.
Although the phenomenon of the current diffusion between two resistive strands depends on the quantities listed above, the diffusion length may also influenced this process. Two limit cases can be pointed out:

1. if $l \ll \lambda$, $\xi \to 0$:

   $$u_{AB} \to i_{tr}\ l\ r_{NM}\frac{1}{\xi^2} = i_{tr}\frac{1}{lgw},$$

   the contact resistance dominates the process and the diffusion of the current from one strand to the other covers uniformly the whole length of the contact. Each strand is equipotential;

2. if $l \gg \lambda$, $\xi \to \infty$:

   $$u_{AB} = i_{tr}\ l\ r_{NM}\frac{\xi^2}{12} = i_{tr}\frac{R^2 G}{12},$$

where $R = r_{NM}l$ is the total longitudinal resistance of one strand and $G = lg_c w$ is the total transverse conductance between the two strands. In this case the current diffusion is pronounced at the contact longitudinal ends.

5.3.3 Contact model

To analyze the experimental data, being the two strands parallel, the contact length is l [m] and $w(x)$ [m] is constant along the strands, whereas local contact areas are present between the strands in the Rutherford and the cable-in-conduit conductors. Here two models are considered to represent the cross-section of the two strands in contact. Both models neglect any possible strand longitudinal strain due to Poisson's ratio.

First model

In the first contact model, already presented and used in Section 3.3, the width of the contact is computed directly from the distance d between the strands centers in the cross-section, neglecting any strand radius change (see Figure 5.9).
Assuming circular strands cross-sections with the original diameter D_0, since ϵ is negative, it follows:

$$l = l_0 - \Delta l = 2D_0 - \Delta l\,, \tag{5.10}$$

$$\epsilon = \frac{\Delta l}{l_0} = \frac{d}{D_0} - 1\,, \tag{5.11}$$

$$w = \sqrt{D_0^2 - d^2} \Rightarrow \frac{w}{D_0} = \sqrt{-2\epsilon - \epsilon^2}\,. \tag{5.12}$$

The graph of w/D_0 as a function of ϵ is shown in Figure 5.10.

Second contact model

In principle, in the absence of longitudinal strain, a compensation between the local cross-section reduction in the contact zone and the rest of the cross-section should be taken into account. This compensation leads to an increased contact width. A second model has therefore been developed in which, once the contact occurs, the cross-section is still assumed circular, however with a diameter suitably augmented to keep the strand cross-section area constant (see Figure 5.11). Actually, this model is relevant for the current geometry,

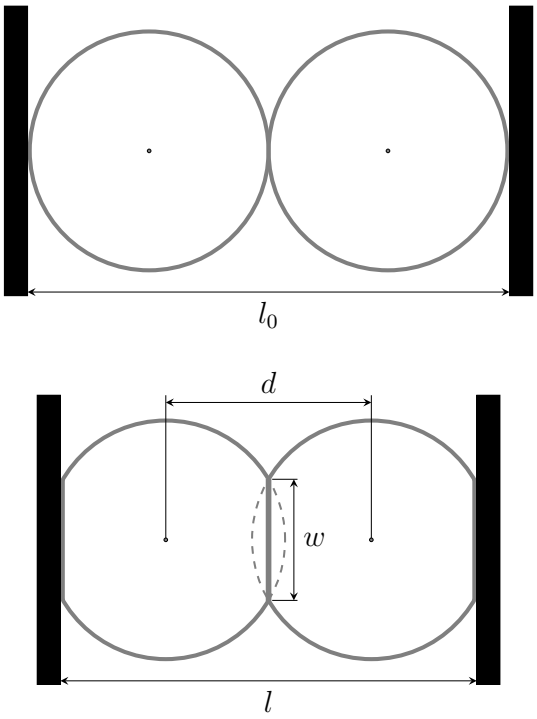

Figure 5.9: First contact model. Above: initial state. Below: pressed state.

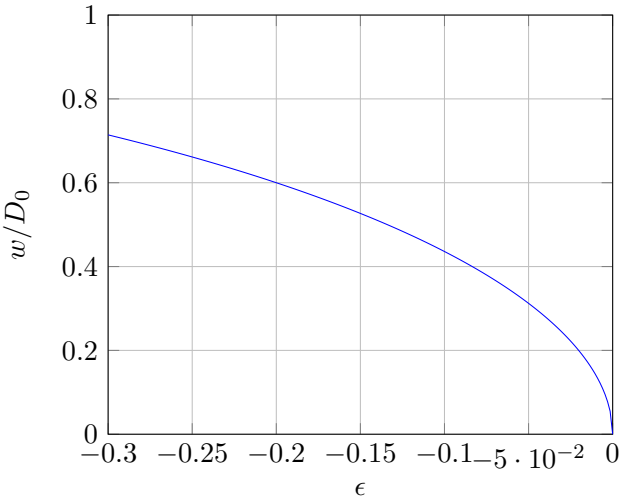

Figure 5.10: First contact model: contact width as a function of the strands transverse deformation ϵ.

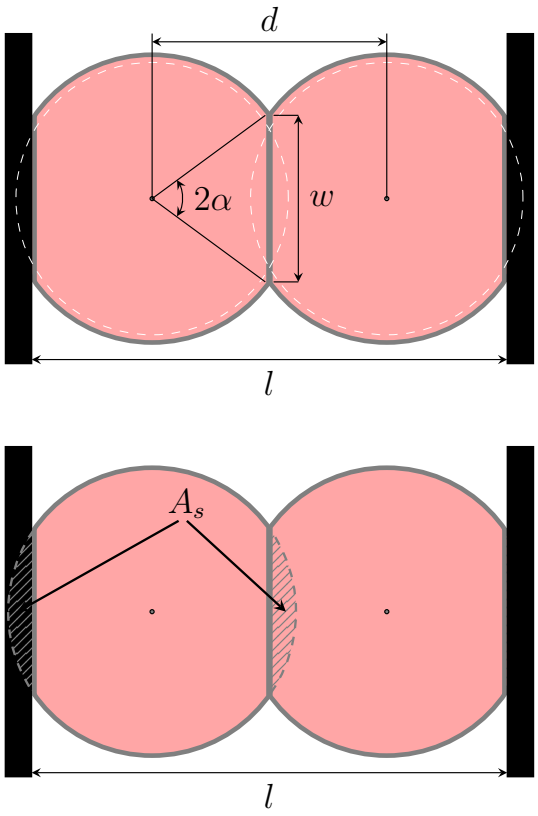

Figure 5.11: Press state with the new contact model. Above: the net strands area (red) and the initial strands circumference (dashed lines). Below: detail of the lateral circular segments (dashed areas) of one strand after the diameters enlargement.

whereas in case of a multi-strand conductor, several contacts occur between one strand and the others at any cable cross-section reducing the feasibility of this contact model. The area of the deformed cross-section is:

$$A = r^2 \left(\pi - 2\alpha + \sin\left(2\alpha\right)\right) \,, \tag{5.13}$$

$$d = D\cos(\alpha)\,, \tag{5.14}$$

$$w = D\sin(\alpha)\,, \tag{5.15}$$

where $D = 2r$ is the augmented radius and 2α is the angle at centrum corresponding to the deformation. Calling again $D_0 = 2r_0$ the original undeformed

strand diameter, the conservation of the cross-section area gives:

$$\frac{D}{D_0} = \frac{1}{\sqrt{1 - \dfrac{2\alpha - \sin(2\alpha)}{\pi}}} = \psi(\alpha)\,, \tag{5.16}$$

$$\epsilon = \psi(\alpha)\cos(\alpha) - 1\,. \tag{5.17}$$

$$\frac{w}{D_0} = \psi(\alpha)\sin(\alpha)\,, \tag{5.18}$$

$$\frac{d}{D_0} = \psi(\alpha)\cos(\alpha)\,, \tag{5.19}$$

The graph of $\psi(\alpha)$, plotted in Figure 5.12 (a), shows that a non negligible diameter increase is to be considered when $\alpha \geq 40°$, corresponding to $\epsilon \approx -0.18$. For each level of compaction, α can be obtained by numerically solving (5.17). An approximate expression of α as a function of d/D_0 can be found as:

$$\alpha = 0.52615 - 0.52353(d/D_0) + 1.4556(1 - d/D_0)^{0.51236}\,. \tag{5.20}$$

With (5.20), a straightforward computation of (5.18) and (5.19) is possible, so that a smaller computational effort is achieved.

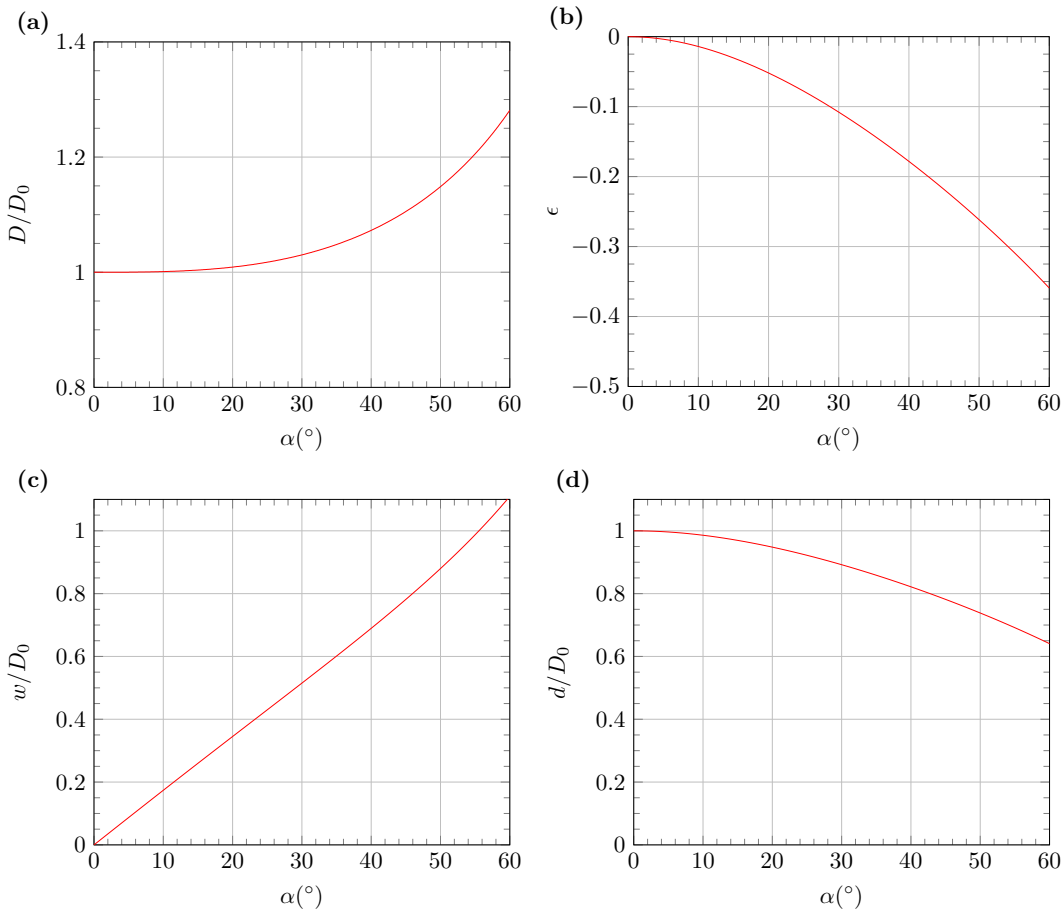

Figure 5.12: Second contact model. Graphs of functions: (a) $\psi(\alpha) = D/D_0$; (b) $\epsilon(\alpha)$; (c) w/D_0; (d) d/D_0.

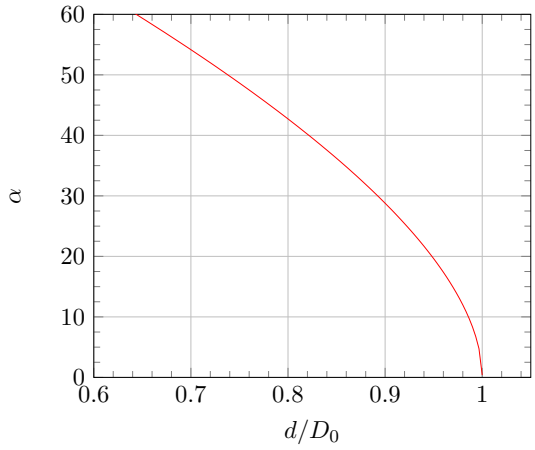

Figure 5.13: Graph of the approximate expression of α.

5.3.4 Contact resistances simulations

The aim of this analysis is to model the resistance measurements presented in section 5.3.1 and to tune the strands parameter ϱ_c [Ωm^2], in order to match the measured values shown in Figure 5.6. Then, this parameter has been adopted to compute the inter-strand contact resistances used in the Rutherford cable losses analysis presented in section 5.4.
The measured mean reference value at $\epsilon = 16.07\%$, which corresponds to R=7.55 $\mu\Omega$, was selected as target for tuning the 2D contact resistivity. Two 100 mm long copper strands with a diameter D_0=3.3 mm and RRR=250 were modeled and placed at distance d:

$$d = D_0 - (\Delta l/2) = 3.3 - (1.061/2) = 2.77\,\text{mm},$$

where

$$\Delta l = 2\,D_0\,\epsilon = 2 \times 3.3 \times 0.1607 = 1.061\,\text{mm}.$$

Since the longitudinal resistance of the strands is not negligible, and two strand tails were present in the tested sample, an additional length $2l_{end} = 58$ mm was considered (see Figure 5.14). So, the effective resistance value taken as target was:

$$R_{eff} = R - R_{2l_{end}} = 7.55 - 0.4585 = 7.092\,\mu\Omega.$$

Analytical model

The contact resistances was first calculated by an analytical approach based on the modeling process shown in Section 5.3.2. The final 2D contact resistivity values adopted to compute the effective resistance R_{eff} with both contact models presented in Sections 5.3.3 and 5.3.3 were:

- $\varrho_c = 5.64E\text{-}10\ \Omega m^2$ for the first model;
- $\varrho_c = 6.73E\text{-}10\ \Omega m^2$ for the second model.

THELMA model

The analysis was also carried out with the electrical lumped network model of the THELMA code. In this case the final adopted values were:

- $\varrho_c = 5.89E\text{-}10\ \Omega m^2$ for the first model;
- $\varrho_c = 7.02E\text{-}10\ \Omega m^2$ for the second model.

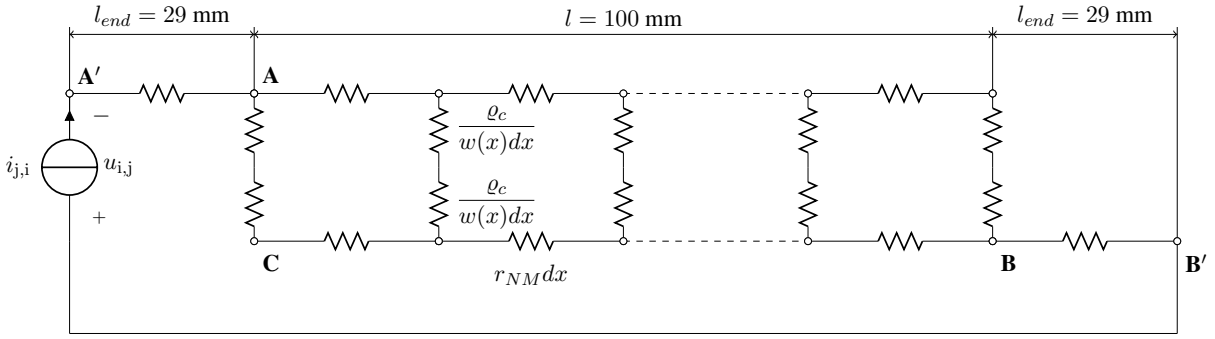

Figure 5.14: THELMA Model of the resistance measurement between two copper strands made at the *PSI* laboratory.

Modelling results

The parameters tuned with both models were used to calculate the resistance at any stage of compression by only modifying the distance d between the two strands centres. The comparison between measured and computed values is shown in Figure 5.15. Few remarks about these results can be made:

1. The resistances computed with the first and the second geometrical contact models show the same trend at high levels of compression, i.e. the selected condition for the 2D resistivity setting, but a deviation is noticeable at the low levels where the contact widths computed with the two models become comparable and the difference in the 2D resistivity leads to different resistance values.

2. The 2D resistivity parameters found with the analytical and the THELMA models are not equal: this is probably due to the lumped nature of the equivalent network analyzed by the THELMA code which is composed by a finite number of contact resistances to allow the current to flow from one strand to the other. Although there are many longitudinally elements to achieve convergence, a non entirely constant contact is considered unlike the analytical case.

3. At any levels of compression, the diffusion length is greater than the contact length ($\xi = l/\lambda < 1$, Figure 5.16): the longitudinal resistance of the copper only slightly influences the measurement of the contact resistance. As a consequence, the current $i(x)$ [A] in the lower strand increases quite linearly along the strand axis as shown in Figure 5.17.

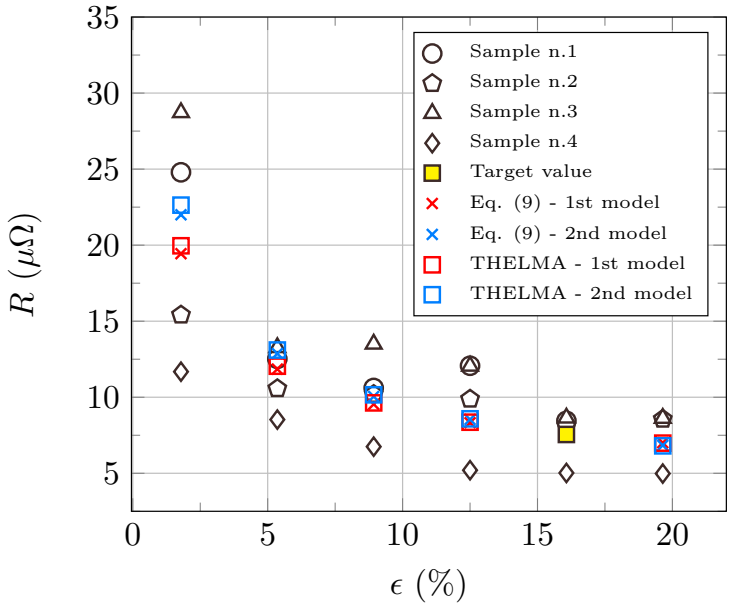

Figure 5.15: Comparison between the computed and the measured resistances; the target value (yellow) selected for the strand parameter $\varrho_c\,(\Omega\mathrm{m}^2)$ setting-up is pointed out.

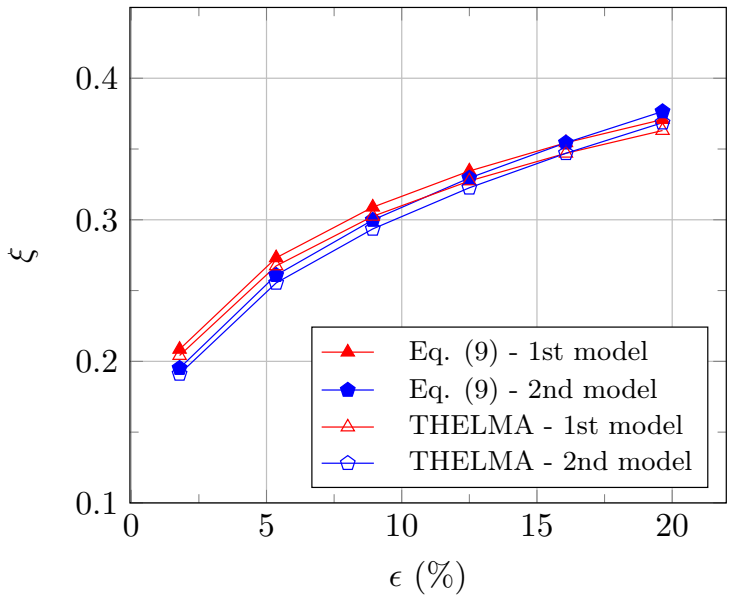

Figure 5.16: Ratio between contact and diffusion length ($\xi = l/\lambda$) as a function of the strands transverse deformation ϵ.

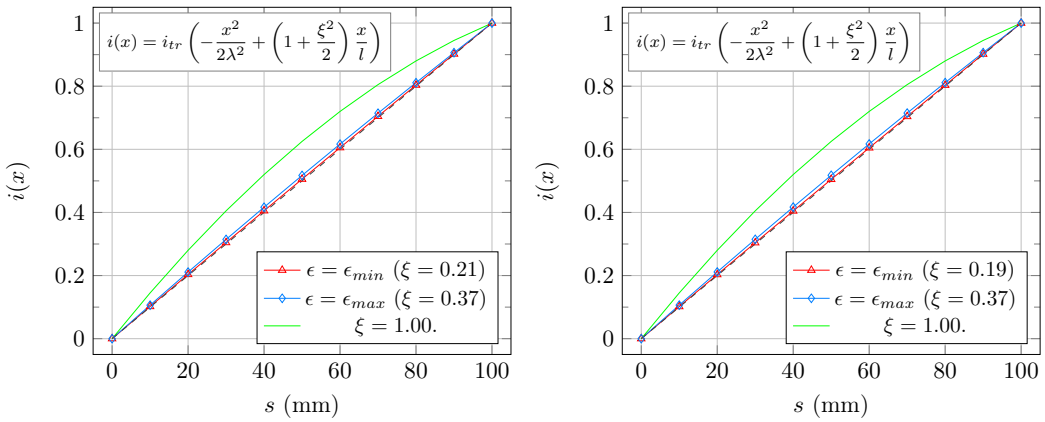

Figure 5.17: Current $i(x)$ in the lower copper strand along the 100 mm contact length computed with the analytical model. Left: first contact model. Right: second contact model.

5.4 Eddy currents loss modeling

The final goal of the presented activity was to predict the AC losses due to the eddy currents induced in the Rutherford cable which has been proposed as the new stabilizer of the (DEMO) RW2 conductor. This preliminary study is based on the contact resistance measurements carried out at SPC with strands which actually are different from those to be used to manufacture the cable. The CuNi cladding, instead of the Chromium coating, of the tested strands is one of the main differences which should give a higher transverse resistance to the cable. So, further investigation will be necessary on the real behavior of the stabilizer.

5.4.1 Cable geometry modeling

The THELMA geometrical model for Rutherford cables (see Section 2.4.1) has been used to reproduce the geometry of the new stabilizer with the following main characteristics [5]:

- Strands diameter: 3.3 [mm];
- N. of strands: 30;
- Dimension: 6×48.33 [mm];
- Void fraction: $\frac{A_t - A_{st}}{A_t} \times 100 \simeq 11.56\,\%$;
- Transposition pitch: 450 [mm].

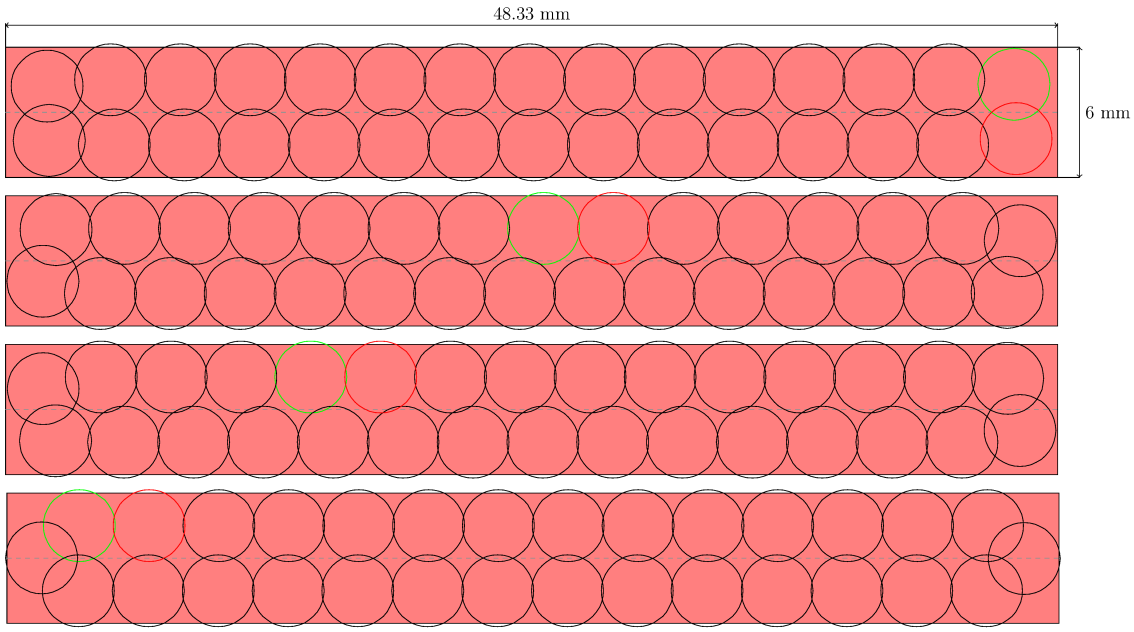

Figure 5.18: Cable cross-sections along its axis; the first (green) and the last (red) strands are also pointed out.

The geometry of a 1 metre long sample with rectilinear axis was modeled and each copper strand was discretized in $N_{em} = 64$ longitudinal elements. In Figure 5.18 four cross-sections at different curvilinear coordinates along the cable axis are shown.

5.4.2 AC losses simulations

To compute the transverse inter-strand conductances of the cable equivalent distributed network, the value of contact resistivity determined as described in Section 5.3.4, i.e. $\varrho_c = 7.02E\text{-}10\,\Omega m^2$, and the geometry of Section 5.4.1 have been considered. Even if the stabilizer is composed by 30 strands, the second contact model has been used to calculate the conductances without introducing a significant error. In fact, as noticeable in Figure 5.18, the main contacts take place between couples of strands from different layers and not between adjacent strands. This is due to the high state of compaction in the direction perpendicular to the broad faces of the conductor. Since the tests are supposed to be carried out in the SULTAN facility, both the DC and AC coils of SULTAN have been modeled to simulate the testing scenario. The temperature is set equal to 4.5 K while a DC background field of 2 T and a sinusoidal AC field of amplitude 0.3 T with a direction perpendicular to the wide side

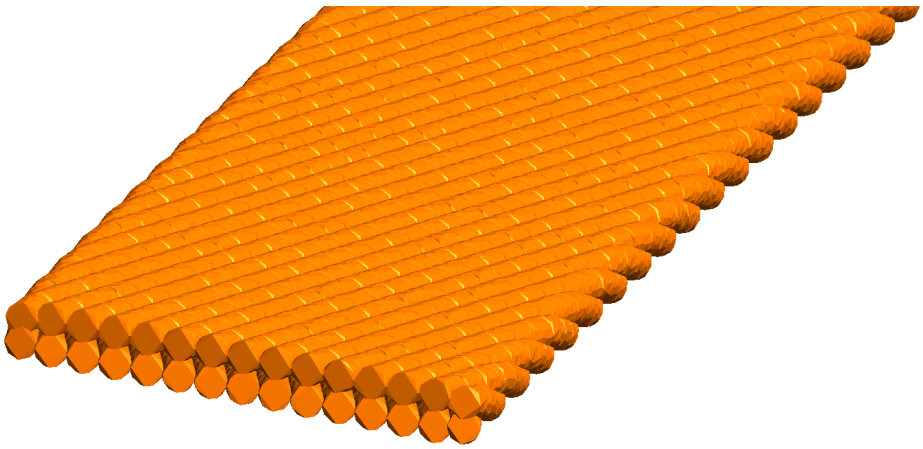

Figure 5.19: 3D view of a end of the cable.

of the rectangular cross-section are imposed. The only left leg conductor has been modeled (see Figure 4.5), and a frequency range from 0.01 to 1 Hz has been considered.
To account for the intra-strand loss resulting by the currents loops induced inside the single resistive strands with a non negligible longitudinal resistance ($R_{\parallel}$), an analytical approach has been adopted. The following formula taken from [85] is considered:

$$P_{ed} = \frac{1}{8}\frac{B_0^2\omega^2 r_{st}^2}{\varrho_m}\ [W/m^3]. \tag{5.21}$$

This formula refers to a round wire made by a normal metal in a transverse external field $B = B_0 sin(\omega t)$, where r_{st} is the strand radius and ϱ_m the resistivity of the metal. The intra-strand loss is first calculated at different frequencies with (5.21) and then added to the inter-strand loss, obtained with the THELMA code, due to the eddy currents crossing the transverse contact resistances between the cable strands ($R_{\perp}$). In Figure 5.20, the numerical results are shown and compared with the experimental ones measured in SULTAN with the "Full Profile" RW2 prototype [84]. The losses are not normalized to the volume of the conductor because the portion of the samples exposed to the AC field is the same and equal to about 400 mm, i.e. the SULTAN bore high field zone. Since the RW2 central core is sandwiched between two stabilizing shells, the computed loss multiplied by 2 are also plotted to get a qualitative estimate of the loss in both the Rutherford cables. It must be noticed that, in this model the screening effect due to the superconducting strands is not taken into account.

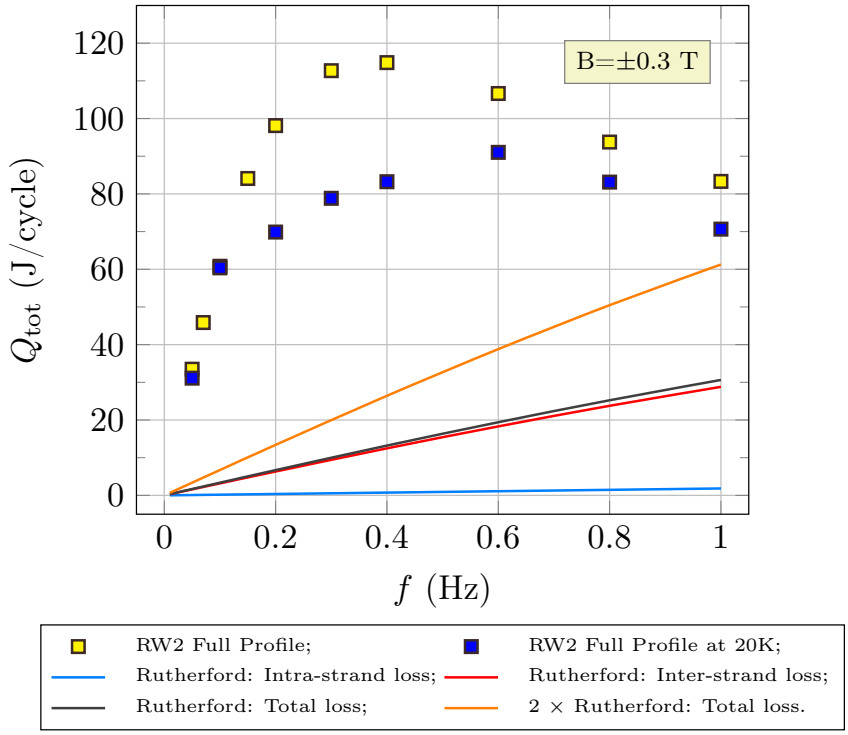

Figure 5.20: Comparison between the computed AC losses in the Rutherford stabilizer and the measured losses in the RW2 conductor with the "Full Profile" stabilizer (one leg).

To further investigate the eddy currents loss, the simulations were made considering different key parameters of the copper stabilizer. As first analysis, the RRR of the copper strands was changed from 250 to 400: since the changing parameter involved the strands behavior, the value of contact resistivity ϱ_c was trimmed to cope with the measured values in order to calculate the inter-strand conductances necessary for the AC loss computation. The second set of simulations aimed at studying the effect of the transposition pitch of the cable: two more samples with a transposition pitch of 400 and 500 mm respectively were modeled. Looking at the results in Figure 5.21, both cases seem to indicate that the inter-strand loss is dominant with respect to the intra-strand one. In fact, the increase of the strand RRR, i.e. the lower copper resistivity, does not lead to substantial changes in terms of losses, whereas the initial slope of the loss curves and hence the time constant $n\tau$ of the Rutherford cable varies significantly with different transposition pitches. This result is reasonable if $R_{\parallel} \ll R_{\perp}$: in this case, the contact resistances are large enough so that the longitudinal one is negligible and the cable behaves like a zero re-

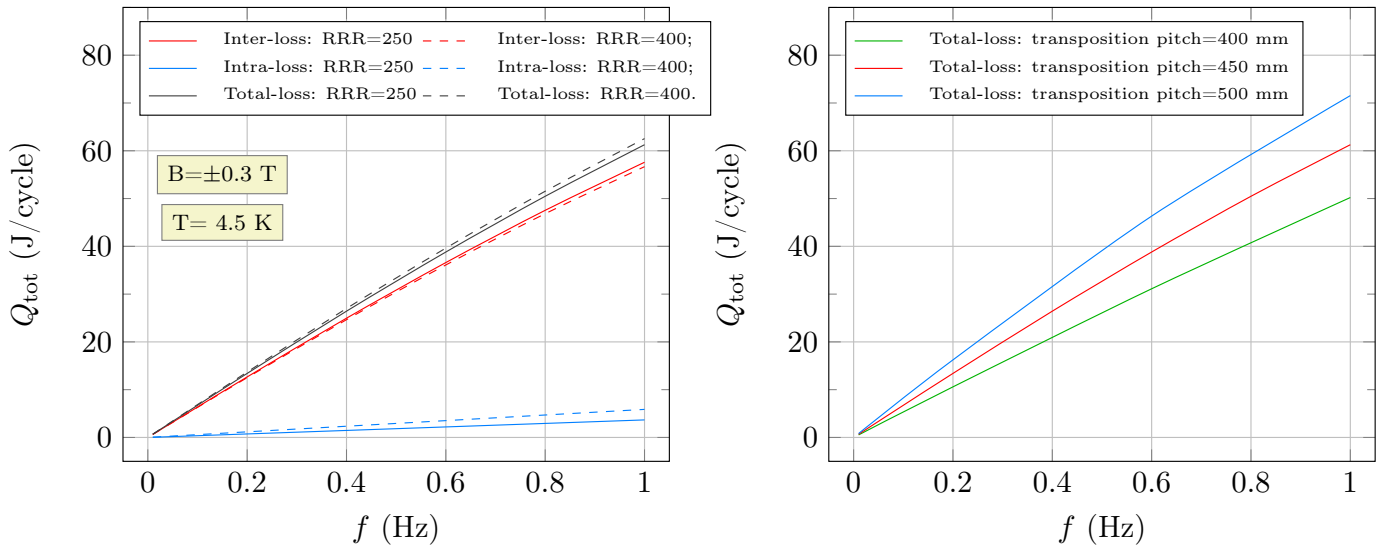

Figure 5.21: Left: Comparison between the AC losses in two Rutherford cables made by strands with different RRR; Right: Comparison between the AC losses in three Rutherford cables with different transposition pitches.

sistance conductor. For the Rutherford stabilizer, an assessment is given here by comparing the $R_\perp$ and $R_\parallel$ resistances of an ideal induced current loop like the one shown in Figure 5.22:

$$R_\perp \cong \frac{\varrho_c}{A_{contact}} = \frac{\varrho_c}{D^2} = \frac{7.02E-10}{1.089E-05} = 64.460\ \mu\Omega\,,$$

$$R_\parallel = \frac{\varrho_m}{A_{st}}\frac{l_{pitch}}{2} = \frac{6.761E-011}{8.553E-06} \times \frac{0.45}{2} = 1.778\ \mu\Omega\,,$$

$$\frac{R_\perp}{R_\parallel} = \frac{6.446E-05}{1.778E-06} = 36.241\,.$$

where D is the strand diameter and l_{pitch} is the conductor transposition pitch. The ratio between $R_\perp$ and $R_\parallel$ that results by considering a transposition pitch of 450 mm is large enough to confirm what was previously supposed and, moreover, if the limit case $R_\perp/R_\parallel \cong 1$ is considered by reducing the strand contact resistivity to $\varrho_c = 2E\text{-}11\,\Omega m^2$, the effect of the transposition pitch on the inter-strand loss vanishes as shown if Figure 5.23.

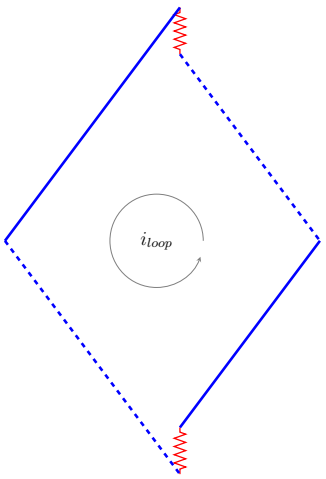

Figure 5.22: Induced current loop inside the Rutherford cable made by two contact points with resistance $R_\perp$ (red) and two branches with longitudinal resistance $R_\parallel$ (blue).
.

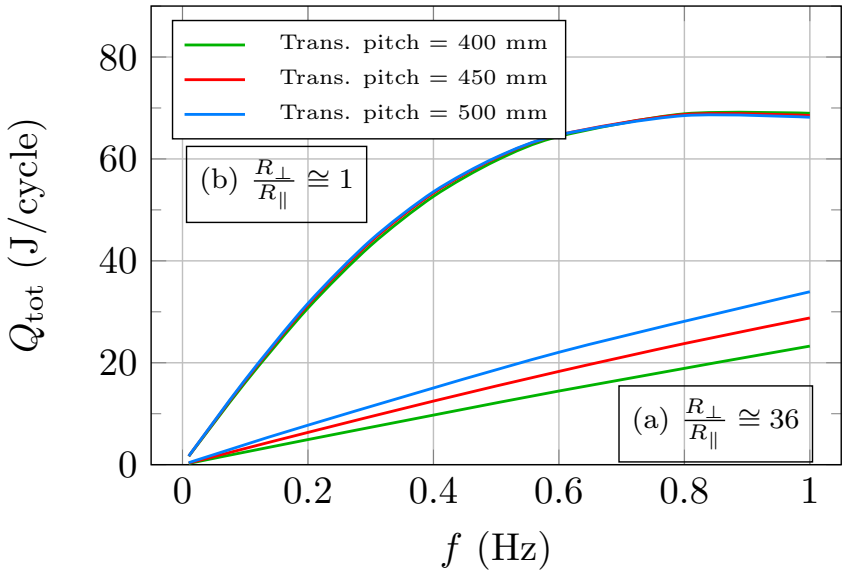

Figure 5.23: Comparison between the inter-strand loss computed by changing the transposition pitch of two Rutherford stabilizers composed by strands with different contact resistivity. Case (a): the value of ϱ_c is the tuned one of Section 5.3.4; case (b): a relatively low value of ϱ_c has been imposed.

Chapter 6

Conclusions

The aim of the present work was to develop new models for the numerical code THELMA. This code is able to study and analyze superconducting cables and magnets through suitable geometrical models and thermo-electromagnetic equivalent networks. The main objective of this thesis was to implement new geometrical models for multi-stage superconducting cables proposed for fusion reactors magnets.
A new model based on a pseudo-structural approach has been developed.

- The new model is able to reproduce in a verisimilar way the trajectories of the cable strands, whatever the final cross-section shape, thanks to the mimicking of the cabling process. The strands are first wound together to form bigger and bigger bundles by the progressively rotation of the sub-bundles axes, and then they are compacted down to the desired cross-section. An iterative procedure to remove the strands interferences on the cable cross-sections has been implemented. An elastic force is considered wherever an interference appears between the strands as a consequence of both the cabling and the compaction procedure. This model has also been adapted to describe the geometry of Rutherford-like cables composed of multi-stage bundles instead of single strands.

- Since the new geometrical model gives the possibility to remove the interferences between strands, a new contact model has been developed to evaluate the inter-strand resistances on the basis of the contact surface thanks to the computation of the local contact width. As a consequence, the value of the contact resistances is computed on the basis of the contact area.

The new geometrical and the contact models have been validated through the

calculation of contact resistances and the simulation of coupling currents loss in rectangular multi-stage conductors.

- The inter-strand resistances of the WR WP2 and RW WP1 prototype conductors proposed for the DEMO TF coils have been analyzed. For each cable, the strand 2D contact resistivity ϱ_c has been tuned in order to match the experimental measurements of contact resistances. The comparison shows that the measured data are sufficiently reproducible with the consideration of one free resistivity parameter to be tuned. On the other hand, these analyses were slightly limited by the computational time needed by the new geometrical model to generate a very large number of sample geometries with different phase set in order to carry out a statistical analysis of the contact resistances distribution.

- A preliminary study about the simulation of coupling currents loss has been done by considering a CIC conductors with rectangular cross-section composed of a few number of strands. The ϱ_c has been set in order to match the AC test results. The agreement between computed and measured loss is very good in the low frequencies range with the complete geometrical model. On the other hand, a deviation has been noticed at higher frequencies. Four more samples of the same conductor have been considered and modeled with different phase sets by considering a simplified cross-section made of 16 equivalent macrostrands. A parametric analysis demonstrated that denser longitudinal discretizations can lead to a reduction of the computed coupling loss at high frequencies. Nevertheless, the increase in computational time to be paid with an increased number of longitudinal elements is not justified if the low frequency range is considered.

- To further validate the geometrical model, the coupling loss in the WR WP2 conductors has been simulated. In this case, the value of ϱ_c tuned with respect to the contact measurements was used to calculate the inter-strand conductances. The numerical results obtained with a simplified cable model made by 43 equivalent macrostrands have shown a sufficient agreement with the experimental data at low frequencies whatever the phase set considered. Nevertheless, further data must be collected from the numerical analysis to understand the relation between the longitudinal strand discretization and the computed coupling loss.

In addition, the present thesis include the research activity carried out at the Paul Scherrer Institute (PSI) with the Superconductivity Group of the Swiss Plasma Center (EPFL). The eddy currents loss in the new stabilizer of

the RW2 prototype for the DEMO TF coils has been numerically modeled. The THELMA code has been used to reproduce the geometry of the stabilizer which consists in a Rutherford cable composed of 30 chromium-coated copper strands and to simulate the loss due to the presence of an external AC field. To calculate the contact conductances among the strands of the cable, the strand contact 2D resistivity parameter has been tuned starting from the contact resistance measurements carried out with two parallel strands at the PSI laboratory.

- The eddy currents loss in the Rutherford stabilizer computed with THELMA shown a lower time constant $n\tau$ and a higher loss peak frequency in comparison with the already tested full-profile RW2 sample assembled with the copper mixed matrix. Since most of the AC losses measured with the full-profile RW2 were due to the eddy currents induced in the copper stabilizer, the Rutherford cable seems to be a promising choice as new stabilizer.

Future work

Further studies are needed to improve the iterative method for the strands interferences removal process implemented in the new geometrical model. Future work will focus on the modeling of the coupling current loss inside a multi-stage Rutherford-like conductor to assess the results obtained with this kind of cables.
As regards the new stabilizer of the RW2 conductor, new contact resistances measurements carried out with CuNi-clad copper strands will be useful for the tuning of the strands contact parameter needed for the calculation of the contact conductances and the eddy currents loss in the final design of the Rutherford stabilizer. Moreover, a new implementation in the THELMA code is foreseen for the modeling of the whole RW2 cable, i.e. central core and surrounding stabilizers.

Bibliography

[1] Image licensed under a Creative Commons Attribution-ShareAlike 4.0 International License. Charlie Sanabria. https://nationalmaglab.org/magnet-development/applied-superconductivity-center/asc-image-gallery/nb3sn-image gallery.

[2] V. Corato, L. Affinito, A. Anemona, U. Besi Vetrella, A. Di Zenobio, C. Fiamozzi Zignani, R. Freda, G. Messina, L. Muzzi, M. Perrella, et al. Detailed design of the large-bore 8 T superconducting magnet for the NAFASSY test facility. *Superconductor Science and Technology*, 28(3):034005, 2015.

[3] Y. Tsui and D. P. Hampshire. Critical current scaling and the pivot-point in Nb_3Sn strands. *Supercond. Sci. Technol.*, 25(5):054008, April 2012.

[4] Dipak Patel, Su-Hun Kim, Wenbin Qiu, Minoru Maeda, Akiyoshi Matsumoto, Gen Nishijima, Hiroaki Kumakura, Seyong Choi, and Jung Ho Kim. Niobium-titanium (Nb-Ti) superconducting joints for persistent-mode operation. *Scientific reports*, 9(1):1–7, 2019.

[5] Giulio Manfreda. *Numerical Analysis Of Coupled Thermal-Electromagnetic Problems In Superconducting Cables.* PhD thesis, Udine University, Industrial and Information Engineering PhD, Via Delle Scienze, 208, April 2015.

[6] K. Yagotintsev and A. Nijhuis. AC loss, interstrand resistance and mechanical properties of prototype EU DEMO TF conductors up to 30 000 load cycles. *Supercond. Sci. Technol.*, 31(2):025010, Feb. 2018.

[7] T. Bagni, A. Devred, and A. Nijhuis. Strand level modeling of contact resistance and coupling loss for EU-DEMO-TF prototype conductors. *Superconductor Science and Technology*, 32(10):105012, 2019.

[8] Christophe Geuzaine and Jean-François Remacle. Gmsh: A 3-D finite element mesh generator with built-in pre-and post-processing facilities.

International journal for numerical methods in engineering, 79(11):1309–1331, 2009.

[9] A. Vostner, P. Bauer, R. Wesche, U. Besi Vetrella, B. Stepanov, A. della Corte, A. Portone, E. Salpietro, and P. Bruzzone. Development of the EFDA dipole high field conductor. *IEEE Trans. Appl. Supercond.*, 18(2):544, June 2008.

[10] G. Pucella and S.E. Segre. *Fisica dei plasmi*. 2009.

[11] *www.iter.org*.

[12] N. Mitchell, A. Devred, P. Libeyre, B. Lim, F. Savary, et al. The ITER magnets: Design and construction status. *IEEE Trans. Appl. Supercond.*, 22(3):4200809, June 2012.

[13] G. Federici, R. Kemp, D. Ward, C. Bachmann, T. Franke, S. Gonzalez, C. Lowry, M. Gadomska, J. Harman, B. Meszaros, C. Morlock, F. Romanelli, and R. Wenninger. Overview of EU DEMO design and r&d activities. *Fusion Engineering and Design*, 89(7):882 – 889, October 2014.

[14] S. Russenschuck. *Field computation for accelerator magnets: analytical and numerical methods for electromagnetic design and optimization*. Wiley, 2010.

[15] L. Cooley, P. Lee, and D. C. Larbalestier. Conductor processing of low Tc materials: The alloy NbTi. *Handbook of Superconducting Materials*, pages 603–638, 2003.

[16] B. T. Matthias, T. H. Geballe, S. Geller, and E. Corenzwit. Superconductivity of Nb_3Sn. *Phys. Rev.*, 95:1435, 1954.

[17] J. W. Ekin. Current transfer in multifilamentary superconductors. I. Theory. *Journal of Applied Physics*, 49(6):3406–3409, 1978.

[18] M. N. Wilson. *Superconducting magnets*. Mono. Cryog. Clarendon Press, 1983.

[19] David M. J. Taylor and Damian P. Hampshire. Relationship between the n-value and critical current in Nb_3Sn superconducting wires exhibiting intrinsic and extrinsic behaviour. *Supercond. Sci. Technol.*, 18(12):S297—S302, Dec. 2005.

[20] D. M. J. Taylor, S. A. Keys, and D. P. Hampshire. $E - J$ characteristics and n-values of a niobium-tin superconducting wire as a function of magnetic field, temperature and strain. *Physica C*, 372–376:1291–1294, August 2002.

[21] Luca Bottura. A practical fit for the critical surface of Nb-Ti. *IEEE T. Appl. Supercond.*, 10(1):1054–1057, March 2000.

[22] D. M. J. Taylor and D. P. Hampshire. The scaling law for the strain dependence of the critical current density in Nb_3Sn superconducting wires. *Supercond. Sci. Technol.*, 18(12):S241–S252, November 2005.

[23] L. Summers, M. Guinan, J. Miller, and P. Hahn. A model for the prediction of Nb_3Sn critical current as a function of field, temperature, strain, and radiation damage. *IEEE T. Magn.*, 27(2):2041–2044, March 1991.

[24] A. Godeke, B. Haken, H. H. J. ten Kate, and D. C. Larbalestier. A general scaling relation for the critical current density in Nb_3Sn. *Supercond. Sci. Technol.*, 19(10), 2006.

[25] C. P. Bean. Magnetization of high-field superconductors. *Rev. Mod. Phys.*, 36(1):31–39, 1964.

[26] M. N. Wilson, C. R. Walters, J. D. Lewin, and P. F. Smith. Experimental and theoretical studies of filamentary superconducting composites. *J. Appl. Phys.*, 3(11):1517–1585, November 1070.

[27] G. H. Morgan. Theoretical behavior of twisted multicore superconducting wire in a time-varying uniform magnetic field. *J. Appl. Phys.*, 41:3673, 1970.

[28] Sergey A. Lelekhov and Vladimir I. Tronza. AC loss before and after cyclic mechanical loading in the ITER RF CICCs. *IEEE Transactions on Applied Superconductivity*, 24(3):1–5, 2013.

[29] K. Kwasnitza. Scaling law for the AC losses of multifilament superconductors. *Cryogenics*, 17(11):616–620, 1977.

[30] H. Bajas. *Numerical simulation of the mechanical behavior of the ITER cable-in-conduit conductors*. PhD thesis, École Centrale Paris, 2012.

[31] H. Bajas, D. Durville, D. Ciazynski, and A. Devred. Numerical simulation of the mechanical behavior of iter cable-in-conduit conductors. *IEEE Trans. Appl. Supercond.*, 20(3):1467–1470, June 2010.

[32] R. Riccioli, A. Torre, M. Breschi, , and D. Durville. Mechanical modeling and first case study on iter tf cicc loading cases with upgraded finite element code simulations. *IEEE T. Appl. Supercond.*, 29(5):0603905, August 2019.

[33] F. Bellina, D. P. Boso, B. A. Schrefler, and G. Zavarise. Modelling a multistrand SC cable with an electrical DC lumped network. *IEEE T. Appl. Supercond.*, 12(1):1408–1412, March 2002.

[34] L. Muzzi, L. Affinito, S. Chiarelli, V. Corato, A. della Corte, A. Di Zenobio, R. Freda, S. Turtù, A. Anemona, R. Righetti, A. Bragagni, M. Seri, F. Gabiccini, G. Roveta, A. Aveta, S. Galignano, P. Bruzzone, K. Sedlak, B. Stepanov, and R. Wesche. Design, manufacture, and test of an 80 kA-class Nb_3Sn Cable-In-Conduit Conductor with rectangular geometry and distributed pressure relief channels. *IEEE Trans. Appl. Supercond.*, 27(4):4800206, June 2017.

[35] A. Di Zenobio, R. Albanese, A. Anemona, M.E. Biancolini, R. Bonifetto, C. Brutti, V. Corato, F. Crisanti, A. della Corte, G. De Marzi, C. Fiamozzi Zignani, F. Giorgetti, G. Messina, L. Muzzi, L. Savoldi, G. Tomassetti, S. Turtù, F. Villone, and A. Zappatore. DTT device: Conceptual design of the superconducting magnet system. *Fusion Engineering and Design*, 122:299–312, April 2017.

[36] A. Della Corte, V. Corato, A. Di Zenobio, C. Fiamozzi Zignani, L. Muzzi, G. M. Polli, L. Reccia, S. Turtù, P. Bruzzone, E. Salpietro, and A. Vostner. Successful performances of the EU-AltTF sample, a large size Nb_3Sn cable-in-conduit conductor with rectangular geometry. *Superconductor Science and Technology*, 23(4):045028, Mar 2010.

[37] Pierluigi Bruzzone, Boris Stepanov, Rainer Wesche, Antonio della Corte, Luigi Affinito, Matteo Napolitano, and Alexander Vostner. Test results of a Nb_3Sn cable-in-conduit conductor with variable pitch sequence. *IEEE Trans. Appl. Supercond.*, 19(3):1448–1451, June 2009.

[38] Giulio Manfreda, Fabrizio Bellina, Valentina Corato, Antonio della Corte, and Pierluigi Ribani. Coupled thermal and electromagnetic analysis of the NAFASSY magnet. *IEEE Trans. Appl. Supercond.*, 25(3):4801406, June 2015.

[39] L. Chiesa, M. Takayasu, and J. V. Minervini. Contact mechanics model for transverse load effects on superconducting strands in cable-in-conduit

conductors. In U. Balachandran, editor, *Advances in Cryogenic Engineering*, volume 56, pages 208–215, College Park, MD 20740, USA, April 8 2010. Proceeding of the Cryogenic Engineering Conference, 19–23 Jul 2010, Wroclaw, Poland, American Institute of Physics.

[40] T. Wang, L. Chiesa, and M. Takayasu. Fundamental evaluations of transverse load effects of Nb3Sn strands using finite element analysis. *paper 3MP2E*.

[41] P. Bruzzone, K. Sedlak, B. Stepanov, R. Wesche, L. Muzzi, M. Seri, L. Zani, and M. Coleman. Design, manufacture and test of a 82 kA React&Wind TF conductor for DEMO. *IEEE Trans. Appl. Supercond.*, 26(4):4801805, June 2016.

[42] Arjan Peter Verweij. *Electrodynamics of superconducting cables in accelerator magnets*. PhD thesis, University of Twente, The Netherlands, Sept. 1995.

[43] M.D. Sumption, E.W. Collings, R.M. Scanlan, A. Nijhuis, and H.H.J. ten Kate. Core-suppressed AC loss and strand-moderated contact resistance in a Nb_3Sn Rutherford cable. *Cryogenics*, 39(1):1–12, Jan. 1999.

[44] A. Nijhuis, N. H. W. Noordman, H. H. J. ten Kate, N. Mitchell, and P. Bruzzone. Electromagnetic and mechanical characterisation of ITER CS-MC conductors affected by transverse cyclic loading, part 2: Interstrand contact resistances. *IEEE Trans. Appl. Supercond.*, 9(2):1069–1072, June 1999.

[45] Paul G. Slade. *Electrical contacts: principles and applications*. CRC press, 2017.

[46] D. Richter, J. D. Adam, J-M. Depond, D. Leroy, and L. R. Oberli. DC measurement of electrical contacts between strands in superconducting cables for the LHC main magnets. *IEEE Trans. Appl. Supercond.*, 7(2):786–792, June 1997.

[47] Kazuya Nakamura, Motoharu Yamanouchi, Kentarou Hashimoto, and Tomoaki Takao. Effects of contact resistance between strands with Cr/non-Cr coating in Cable-in-Conduit Conductors. *IEEE Trans. Appl. Supercond.*, 14(2):1306–1309, June 2004.

[48] W. Abbas, A. Nijhuis, Yu. Ilyin, B. ten Haken, and H.H.J. ten Kate. A fully automatic press for mechanical and electrical testing of full-size ITER

conductors under transverse cyclic load. In U. Balachandran, editor, *Advances in Cryogenic Engineering*, volume 50, pages 51–58, College Park, MD 20740, USA, 2004. Proceedings of the International Cryogenic Materials Conference, 22-26 September, 2003 in Anchorage, Alaska, American Institute of Physics.

[49] Arend Nijhuis, Yuri Ilyin, W. Abbas, Bennie ten Haken, and Herman H. J. ten Kate. Change of interstrand contact resistance and coupling loss in various prototype ITER NbTi conductors with transverse loading in the Twente cryogenic cable press up to 40,000 cycles. *Cryogenics*, 44(5):319–339, May 2004.

[50] Y. Miyoshi, Y. Ilyin, W. Abbas, and A. Nijhuis. AC loss, inter-strand resistance, and mechanical properties of an Option-II ITER CICC up to 30,000 cycles in the press. *IEEE Trans. Appl. Supercond.*, 21(3):1944–1947, June 2011.

[51] Giulio Manfreda and Fabrizio Bellina. Analysis of the quench propagation along Nb_3Sn Rutherford cables with the THELMA code. Part I: geometric and thermal models. *Cryogenics*, 80:357–363, Dec. 2016.

[52] Fabrizio Bellina and Giulio Manfreda. Models of the resistive contact distribution in superconducting ITER CICC full size joints and terminations. *IEEE Trans. Appl. Supercond.*, 25(3):4200606, June 2015.

[53] Henk A. van der Vorst. Bi-CGSTAB: A fast and smoothly converging variant of Bi-CG for the solution of nonsymmetric linear systems. *SIAM J. Scientific Computing*, 13(2):631–644, 1992.

[54] L. Zani et al. Overview of progress on the EU DEMO reactor magnet system design. *IEEE Trans. Appl. Supercond.*, 26(4):4204505, June 2016.

[55] Y. Hashimoto, K. Yoshizaki, and M. Tanaka. Processing and properties of superconducting nb 3 sn filamentary wires. In *Proceedings of the fifth international cryogenic engineering conference, Kyoto, 1974*, 1974.

[56] Kamil Sedlak, Pierluigi Bruzzone, Boris Stepanov, Andries Den Ouden, Jos Perenboom, Antonio Della Corte, Luigi Muzzi, Aldo Di Zenobio, and Federico Quagliata. Test of the MF-CICC conductor designed for the 12-T outsert coil of the HFML 45-T Hybrid magnet. *IEEE Transactions on Applied Superconductivity*, 26(4):1–5, 2015.

[57] L. Muzzi, G. De Marzi, A. Di Zenobio, and A. Della Corte. Cable-in-conduit conductors: lessons from the recent past for future developments

with low and high temperature superconductors. *Superconductor Science and Technology*, 28(5):053001, 2015.

[58] A. Devred et al. Challenges and status of ITER conductor production. *Supercond. Sci. Technol.*, 27(4):044001, April 2014.

[59] D. Bessette. Design of aNb_3Sn cable-in-conduit conductor to withstand the 60000 electromagnetic cycles of the ITER Central Solenoid. *IEEE Transactions on Applied Superconductivity*, 24(3):1–5, 2013.

[60] A. Nijhuis, Herman H. J. ten Kate, P. Bruzzone., and L. Bottura. Parametric study on coupling loss in subsize iter Nb_3Sn cabled specimen. *Transactions on magnetics*, 32(4):2743, July 1996.

[61] A.M. Campbell. A general treatment of losses in multifilamentary superconductors. *Cryogenics*, 22(1):3–16, January 1982.

[62] A. Nijhuis, H.H.J. ten Kate, J.L. Duchateau, and P. Bruzzone. Coupling loss time const ants in full-size Nb_3Sn CIC model conductors for fusion magnets. *Advances in Cryogenic EngiMering*, 42, 1996.

[63] T. Schild and D. Ciazynski. A model for calculating AC losses in multistage superconducting cables. *Cryogenics*, 36(12):1039–1049, 1996.

[64] Maxime Chiletti, Jean-Luc Duchateau, Frederic Topin, Bernard Turck, and Louis Zani. Analytical modelling of CICCs coupling losses: Broad investigation of two-stage model. *IEEE Transactions on Applied Superconductivity*, 29(5):1–5, 2019.

[65] Luca Bottura, Marco Breschi, and C. Rosso. Analysis of electrical coupling parameters in superconducting cables. *Cryogenics*, 43(3-5):233–239, March-May 2003.

[66] E.P.A. van Lanen and A. Nijhuis. JackPot: A novel model to study the influence of current non-uniformity and cabling patterns in cable-in-conduit conductors. *Cryogenics*, 50(3):139–148, March 2010.

[67] S. A. Lelekhov. A physical model and numerical method for losses investigation in superconducting cable-in-conduit conductors (CICC). *Cryogenics*, 46(1):1–8, January 2006.

[68] B. Turck and L. Zani. A macroscopic model for coupling current losses in cables made of multistages of superconducting strands and its experimental validation. *Cryogenics*, 50(8):443–449, Aug. 2010.

[69] Marco Breschi and Pier Luigi Ribani. Electromagnetic modeling of the jacket in cable-in-conduit conductors. *IEEE Trans. Appl. Supercond.*, 18(1):18–28, March 2008.

[70] Pierluigi Bruzzone, Alexander Anghel, Albert M. Fuchs, Gabriel Pasztor, Boris Stepanov, Martin Vogel, and Georg Vecsey. Upgrade of operating range for SULTAN test facility. *IEEE Trans. Appl. Supercond.*, 12(1):520–523, March 2002.

[71] Xi Feng Lu, Stephen Pragnell, and Damian P. Hampshire. Small reversible axial-strain window for the critical current of a high performance Nb_3Sn superconducting strand. *Applied Physics Letters*, 91(13):132512, 2007.

[72] J. H. Murphy, M. S. Walker, W. J. Carr, and P. D. Vecchio. Field orientation dependence of losses in rectangular multifilamentary superconductors. *Adv. in Cry. Eng.*, 22:420, 1977.

[73] W. J. Carr Jr. *AC Loss and Macroscopic Theory of Superconductors.* Taylor & Francis, New York, 2nd edition.

[74] F. Cau and P. Bruzzone. AC loss measurements in cicc with different aspect ratio. *IEEE Trans. Magn.*, 19(3):2383, 2009.

[75] F. Cau and P. Bruzzone. Dependence of the AC loss on the aspect ratio in a cable in conduit conductor. *Supercond. Sci. Technol.*, 23(4):045011, Feb 2010.

[76] K. A. Yagotintsev, W. A. J. Wessel, A. Vostner, A. Devred, D. Bessette, N. Mitchell, Y. Nabara, T. Boutboul, V. Tronza, S. H. Park, et al. Overview of verification tests on AC loss, contact resistance and mechanical properties of ITER conductors with transverse loading up to 30 000 cycles. *Superconductor Science and Technology*, 32(10):105015, 2019.

[77] L.T. Summers, M.W. Guinan, J.R. Miller, and P.A. Hahn. A model for the prediction of Nb_3Sn critical current as a function of field, temperature, strain, and radiation damage. *IEEE Trans. Magn.*, 27(2):2041–2044, March 1991.

[78] Kamil Sedlak, Pierluigi Bruzzone, Boris Stepanov, Rainer Wesche, Xabier Sarasola, Davide Uglietti, Vincenzo D'Auria, Christian Vorpahl, Luigi Affinito, Luigi Muzzi, Antonio della Corte, and Corato Valentina. DC test results of the DEMO TF React&Wind conductor prototype no. 2. *IEEE Transactions on Applied Superconductivity*, 29(5):1–5, 4801005, 2019.

[79] Kamil Sedlak, Pierluigi Bruzzone, Xabier Sarasola, Boris Stepanov, and Rainer Wesche. Design and R&D for the DEMO toroidal field coils based on Nb_3Sn react and wind method. *IEEE Trans. Appl. Supercond.*, 27(3):4800105, June 2017.

[80] Pierluigi Bruzzone et al. LTS and HTS high current conductor development for DEMO. *Fusion Eng. Design*, 96-97:77–82, Oct. 2015.

[81] Pierluigi Bruzzone, Kamil Sedlak, and Boris Stepanov. High current superconductors for DEMO. *Fusion Engineering and Design*, 88(9-10):1564–1568, oct 2013.

[82] Pierluigi Bruzzone, Kamil Sedlak, Xabier Sarasola, Boris Stepanov, Davide Uglietti, Rainer Wesche, Luigi Muzzi, and Antonio della Corte. A prototype conductor by React&Wind method for the EUROfusion DEMO TF coils. *IEEE Trans. Appl. Supercond.*, 28(3):4202705, April 2018.

[83] DEMO reference configuration model, 2017 [Online]. Available: https://idm.euro-fusion.org/?uid=2N4EZW, June 2017.

[84] Pierluigi Bruzzone, Boris Stepanov, Kamil Sedlak, and Valentina Corato. A new test method of AC loss assessment for fusion conductors. *Fusion Engineering and Design*, 2019.

[85] W. J. Carr. AC loss in a twisted filamentary superconducting wire. I. *Journal of Applied Physics*, 45(2):929, Feb. 1974.